11-10-2014

Channel Analysis and Estimation and Compensation of Doppler Shift in Underwater Acoustic Communication and Mitigation of IFI, ISI in Ultra-wideband Radio

Sadia Ahmed
University of South Florida, ahmed3@mail.usf.edu

Channel Analysis and Estimation and Compensation of Doppler Shift in Underwater Acoustic

Communication and Mitigation of IFI, ISI in Ultra-wideband Radio

by

Sadia Ahmed

A dissertation submitted in partial fulfillment
of the requirements for the degree of
Doctor of Philosophy
Department of Electrical Engineering
College of Engineering
University of South Florida

Major Professor: Hüseyin Arslan, Ph.D.
Wilfrido Moreno, Ph.D.
Paris H. Wiley, Ph.D.
Miguel A. Labrador, Ph.D.
David F. Naar, Ph.D.

Date of Approval:
November 10, 2014

Keywords: Channel Classification, Channel Environment, Doppler Scale, OFDM

DEDICATION

To my parents, brother, grandmother, and my family

To everyone who enriched my life with knowledge

To the protection of our planet

To all the children of the world

To those women who did not have the opportunity to pursue higher education

ACKNOWLEDGMENTS

TABLE OF CONTENTS

LIST OF TABLES

LIST OF FIGURES

ABSTRACT

Water occupies three fourth of earth's surface. The remaining one fourth is land. Although human habitats reside on land, there is no denying of the vital connection between land and water. The future sustainability of human species on this planet depends on wise utilization of all available resources, including that provided by the vast water world. Therefore, it is imperative to explore, understand, and define this massive, varying, and in many areas, unexplored water domain.

The water domain exploration and data collection can be conducted using manned or unmanned vehicles, as allowed by the water environment. This dissertation addresses three of the key difficulties that occur during underwater acoustic communication among manned and/or unmanned vehicles and proposes feasible solutions to resolve those difficulties. The focus and the contributions of this research involve the following perspectives:

- Representation of Underwater Acoustic Communication (UAC) Channels: Providing a comprehensive classification and representation of the underwater acoustic communication channel based on the channel environment.

- Estimation and Compensation of Doppler Shift: Providing compensation algorithm to mitigate varying Doppler shift effect over subcarriers in UAC Orthogonal Frequency Division Multiplexing (OFDM) systems.

- Mitigation of Inter-symbol Interference (ISI): Providing feasible solution to long delay spread causing ISI in Ultra-wideband channels.

CHAPTER 1 :

INTRODUCTION

Underwater is an enormous, highly varying, and in many areas an unexplored domain. Communication through this domain presents many unique and complex challenges that vary in their degree of severity in comparison to communication in the terrestrial domain.

This dissertation will address three key challenges in underwater acoustic communication (UAC) and propose feasible solutions to those challenges. Prior to addressing these key issues in UAC, and proposing their solutions, it is important to understand the acoustic wave and its propagation through the water medium, and the uniqueness of underwater acoustic communication (UAC) channel compared to the terrestrial radio frequency (RF) channel.

This chapter presents, first, the basics of sound propagation through water medium, second, the differences between terrestrial radio frequency propagation and underwater acoustic propagation, and third, the major underwater applications .

1.1 Sound Propagation through Water

In this section, the physics of sound is presented first, followed by the propagation of sound through water.

1.1.1 Physics of Sound

Sound is a non-electromagnetic wave that creates compression and rarefaction of a medium and disturbs the mechanical energy within the medium as it propagates through it. Sound is described by its properties, such as frequency, wavelength, period, amplitude, and speed. Amplitude of sound wave is measured by its pressure. Generally, *sound* is what humans can hear. Scientifically, low frequency, human hearing frequency, and high frequency vibration, through all

forms of matter, gas, liquid, solid, and plasma is *sound*. *Acoustics* is the science of production, control, transmission, reception and effects of Sound. Acoustic Communication is the application of acoustics in communication.

1.1.2 Sound Propagation in Water Medium

Sound speed in water primarily depends on, a) depth or pressure, b) temperature, and c) salinity. Slow speed of sound creates latency in communication and loss of efficiency, where the transmitter depends on receiver acknowledgment or handshaking.

The speed of sound in water is determined by the water medium itself. The elasticity of the water medium is the most important factor in determining the speed of sound. The effect of medium density on sound is the second important factor. In addition to the normal density of water, there are several factors, which can cause the density of the water to change: they are salinity, pressure and temperature.

Salinity is defined as the salt content of the water. As salinity increases with the increase of water depth, the sound speed increases. Salinity can be a big factor near rivers. *Pressure* plays an important role below a depth of 1500 feet. As pressure increases, sound speed increases. Pressure increase can be constant and predictable. *Temperature* plays an important role above a depth of 1500 feet. Below that depth, temperature of the ocean is constant, and remains roughly at 1 degC. With each degree celsius increase in temperature, sound speed in water changes by 3 m/sec.

1.2 Major Differences between Terrestrial Radio Frequency and Underwater Acoustic Communication

In this section, the key differences between radio frequency communication through terrestrial medium and acoustic communication through water medium is presented. The terrestrial RF communication will be addressed first, followed by underwater acoustic communication.

1.2.1 Terrestrial Radio Frequency Communication

Radio frequency propagation through the terrestrial medium, and hence terrestrial communication is affected by several factors as follows.

Path Loss in air or space medium represents the loss of transmitted energy of the propagating information signal due to the distance it travels. Path loss is proportional to the distance between the transmitter and the receiver and also depends on the path coefficient. The longer path the signal travels, the more is the loss of energy and higher is the path loss. Empirical models have been derived to represent path loss in air medium.

Long Term Fading is caused by large objects in the signal path that may absorb or reflect signal and cause change in signal energy in addition to path loss. Big obstructions on the path such as mountains, tunnels, etc. can block the signal and reduce its strength. It is generally represented by log normal distribution.

Short Term Fading, Frequency Selectivity is caused in the following way. The phenomena of refraction, defraction, and scattering on objects within the terrestrial radio frequency channel, creates multiple paths that arrive at the receiver at different delays. These paths may vary in magnitude and phase. These multipaths result in delay spread in time domain, and frequency selectivity in frequency domain.

Short Term Fading, Time Selectivity is caused in the following way. The movements of transmitter, receiver, and/or one or more of the surrounding objects in the channel cause changes in the multipaths over time. This change with respect to time creates time selectivity in the time domain and Doppler shift/spread in the frequency domain.

Noise is present in addition to the above mentioned factors. Terrestrial channel can have both frequency dependent and indepent noise.

Fig. 1.1 illustrates the differences between reflection, diffraction and scattering in the terrestrial medium.

1.2.2 Underwater Acoustic Communication

Underwater acoustic communication channel is characterized by the same factors and difficulties that are present in the terrestrial domain. However, the degree of severity between the two domains vary extensively. The factors influencing underwater acoustic communication are presented below.
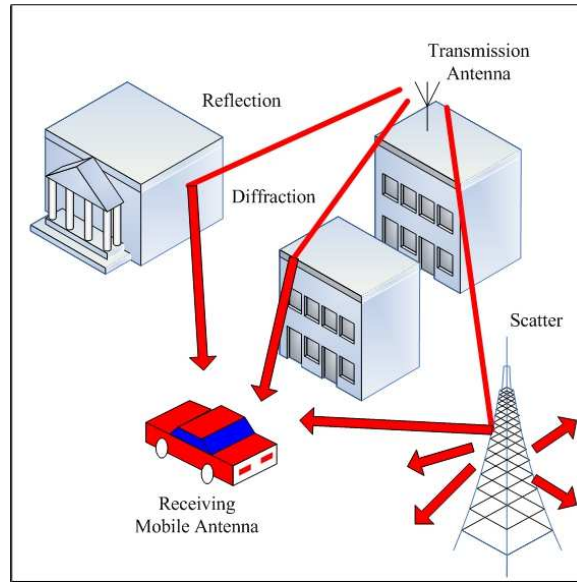
Figure 1.1 Reflection, Diffraction and Scattering in Terrestrial Medium

Path Loss in water medium is more severe compared to air or space medium due to the higher density of water and the water absorption coefficient, which is highly frequency dependent. The attenuation in water for high frequency radio, especially in electrically more conductive salt water, is extremely high. Assuming an average conductivity of seawater of 4 mhos/m, and 0.05 mhos/m in fresh water, the attenuation for 2.4GHz is around 1695 dB/metre in seawater, and 189 dB/m in freshwater. This is clearly not practical [1].

Long Term Fading exists in water due to the shore lines and rugged bottom surface in shallow water, and due to the reefs and rough terrains in the sea water. Large ships or offshore underwater oil drilling equipment, and internal waves over long period of time and internal ocean structure such as underwater reefs, mountains, and canyons can cause long term fading.

Short Term Fading, Frequency Selectivity in underwater is caused in the following way. Underwater multipath formation depends on (a) the reflection and scattering on the boundaries (bottom boundary, water surface boundary) and on any objects in between, (b) the direct path between transmitter and receiver and (c) the refraction or bending of rays depending on depth, pressure and temperature of water at different water levels. Fig. 1.2 illustrates the generic variation of sound speed, according to water depth, caused by the refraction of sound in water. In horizontal

4
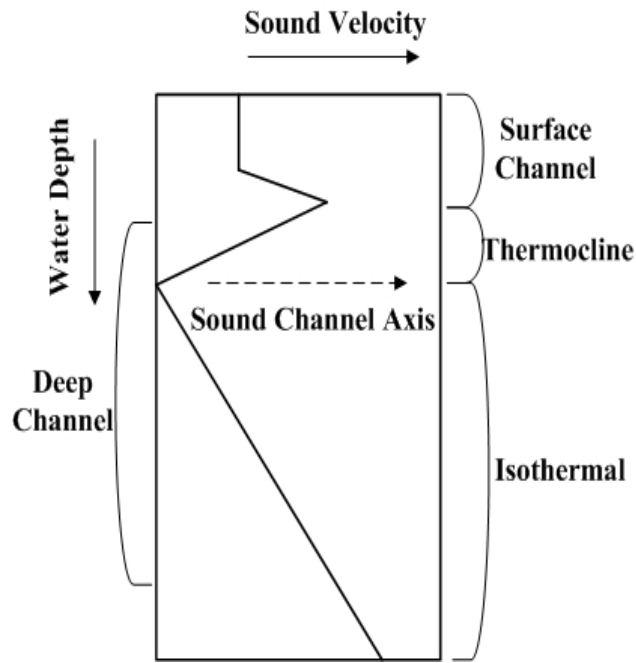
Figure 1.2 Sound Propagation in Water

underwater acoustic channels, multipaths increase to several tens, or hundreds of symbol intervals for moderate to high data rates. For example, a commonly encountered multipath spread of 10 ms in shallow water channel, causes the IS1 to extend over 100 symbols, if the system is operating at a rate of 10 kilosymbols per second (ks/s) [2]. Multipaths vary depending on location of transmitter and receiver. Multipaths also vary according to the transmission links. A vertical link has fewer number of multipaths while a horizontal link creates very long multipath delay profile. Fig. 1.3 and Fig. 1.4 illustrate the vertical and horizontal transmission links.

Short Term Fading, Time Selectivity in underwater is caused in the following way. Acoustic signal fluctuates over time. Scattering on the surface waves in shallow water situation and scattering on deep sea waves in deep water situation may cause time variability of the multipaths. Motion of the transceivers and/or surrounding objects also contributes to time varying multipaths. The time variation in the time domain leads to severe Doppler shift and/or Doppler spread in the frequency domain. Due to low operating frequency, low transmission bandwidth, and low acoustic velocity in the water, the Doppler effect can be severe on the acoustic signal.

5
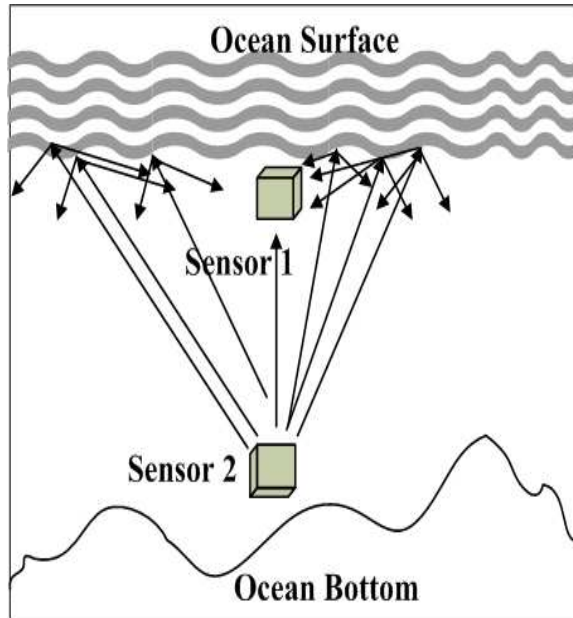
Figure 1.3 Vertical Link Transmission

Underwater Acoustic Signal is band limited. A long range system operating over several tens of kilometers is limited to few kHz of bandwidth; a medium-range system operating over several kilometers has a bandwidth on the order of ten kHz, while a short range system, operating over several tens of meters may have available bandwidth of more than a hundred kHz [2].

Background Noise is present in underwater acoustic channels. The movement of the sea surface, volcanic and seismic activity, shipping, marine life, bubbles, rain, acoustic system, its platform, acoustic vehicles, surface vessels, and submarine vehicles are the major contributors to the background noise. The self background noise may be caused by the transmitter/receiver. The ambient noise naturally exists due to the water, its surroundings, and the marine life. Some background noise, such as the bubble noise, noise from marine life, etc., is frequency dependent.

1.2.3   Achievable Frequency in Acoustic Communication

In the terrestrial RF communication, the commonly encountered frequency and bandwidth lie in the range of MHz and GHz. On the other hand, in UAC communication, the operating frequency and bandwidth are mostly limited in the Hz, kHz range. The achievable transmission

6
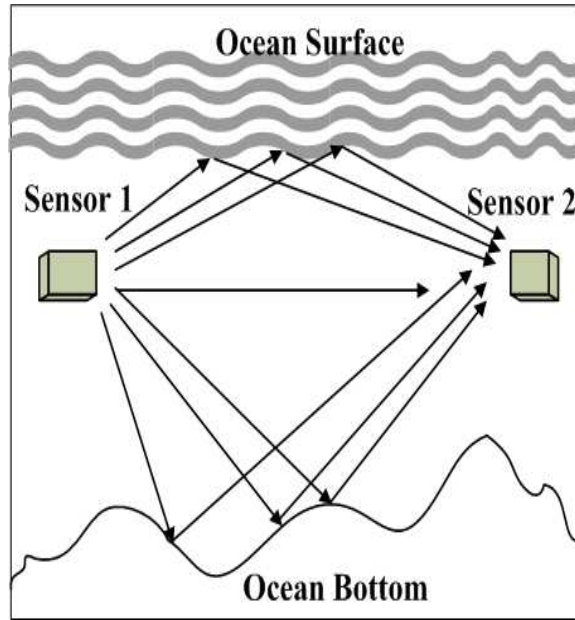
Figure 1.4 Horizontal Link Transmission

frequency, the transmission bandwidth, and consequently the achievable data rate in underwater acoustic communication, depends on many parameters as follows.

The range of transmission or distance affects the path loss encountered by the signal. The transmission frequency and bandwidth depend on how much path loss is allowed in the application due to distance. If the receiver is capable of the desired level of detection with highly erroneous received signal caused by path loss, then higher frequency can be achieved. Path loss due to distance and frequency acts as trade off on one another for the desired transmission signal.

Depending on deep or shallow water, the salinity and temperature and pressure variance, influence the attenuation of the transmitted signal. If the frequency is higher, there may be more attenuation depending on these parameters. Therefore, these environmental parameters also factor into the highest achievable frequency for the specific communication environment.

The geometry of the UAC channel, such as shallow channel, deep channel, the ocean floor, the shoreline, etc., heavily influence the number of multipaths, and consequently the delay spread in time. Transmission of higher bandwidth or shorter symbol duration is possible, if the receiver is

7

capable of handling the multipaths, whether the multipaths create inter-symbol interference (ISI) or not. Higher frequency transmission in turn, reduces the Doppler effect on the signal bandwidth.

1.3 Underwater Applications

In the past, underwater wireless communication was mainly utilized by military operations [3]. Over the past few years underwater wireless communication research has grown immensely to benefit commercial applications including but not limited to the following.

- Remote control in offshore oil industry

- Speech and multimedia transmission among divers

- Autonomous undersea vehicle applications

- Pollution monitoring in underwater environmental applications

- Offshore equipment monitoring

- Underwater robotics

- Underwater observation for weather prediction

- Rescue and search mission

- Ocean sampling of coastal ocean environment

- Distributed tactical surveillance, as in military

CHAPTER 2 :

ANALYSIS OF UNDERWATER ACOUSTIC COMMUNICATION CHANNELS

The underwater acoustic communication (UAC) channel [1]. presents many difficulties such as high frequency, space, and time selectivity, frequency dependent noise, and significant range and band limitation on transmission. Traditional UAC channel models that model such channels primarily include environmental models based on experimental data; models that are developed using mathematical equations such as wave equations, modal methods, and parabolic equations; and using statistical distributions. These methods/models are often limited in their coverage and accurate representations of every possible UAC channel environment. It is also physically impractical and cost ineffective to try to measure/estimate each channel to determine its model.

In chapter 2, cognitive intelligence is used in the selection of the appropriate channel representations according to each sensed UAC channel environment. In this chapter, the UAC channel representations according to the UAC channel environments are analysed and presented.

2.1 Problems in Underwater Acoustic Communication Channel Representation

The underwater acoustic communication (UAC) channel is vast and varying in nature. The existing UAC channel models may not be sufficient to represent every single UAC channel scenario. Moreover, the choice of models from the existing ones may not be accurate to represent the true channel environment. Thus the varying nature of the UAC channel requires representing of such channel according to its channel environment, which in turn is specified by sets of channel parameters. If the channel parameters and hence the channel environment is accurately determined, the environment can be mapped onto the appropriate UAC channel representation [4], [5]. The same channel representations can be reapplied in same or similar environments. The parameter values

---

[1]This chapter is published in The Marine Technology Society (MTS) Journal, vol. 47, no. 3, pp. 99117, May/Jun 2013 Permission is included in Appendix C.

can be adaptively measured/estimated or derived according to the UAC environment. Therefore, the relationship between UAC channel representations and the UAC environments allows wider representation and coverage of the varying UAC channels. A high level classification of the UAC channel environments according to literature is presented in Fig. 2.1. The contributions of this chapter are listed as below.

- This chapter presents an analysis of underwater acoustic communication channel impulse response according to each broadly categorized underwater acoustic communication channel environment in Fig. 2.1.

- Fading characteristics of the received signal and signal to noise ratio (SNR) of UAC channel in each channel environment and the relationship between environment parameters and different types of fading are analyzed and discussed in this chapter.

- The channel representations are generated using the AcTUP software module.

The rest of the chapter is organized as follows. Section 2.2 presents a brief literature review of UAC channel models. Section 2.3 presents the analysis of channel impulse response and fading characteristics of UAC channels according to channel environments. Section 2.4 provides the SNR analysis of the channel representations. Section 2.5 briefly presents the benefits of channel selection and the channel selection methods. Section 2.6 presents the simulation results. Section 2.7 presents the measurement set up and the measurement results, and Section 2.8 addresses the concluding remarks.

2.2   Related Works in UAC Channel Representation

The UAC channels are presented using stochastic models in some literature. In [6], the amplitude and phase fluctuation of received signal is presented first by linear and then nonlinear transformations of Gaussian variables. In [7], the estimation of slow phase fluctuations of channel impulse response is described as Markov's process and the accumulation of impulse channel responses is decided by the Viterbi algorithm. In [8], a channel model is proposed to present the time varying UAC channel, where the time variation is produced by transmitter and receiver motion. In
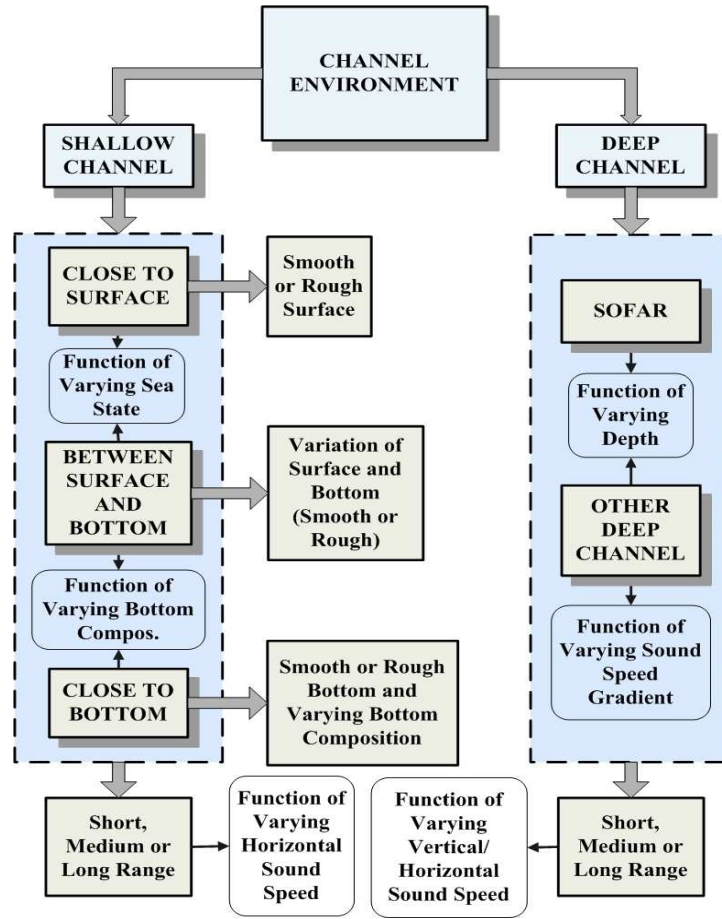
Figure 2.1 Identification and High Level Classification of Underwater Acoustic Communication Channel Environments

this model, the eigen rays corresponding to direct/reflected multipaths are determined using ray tracing while the random diffusive multipaths are modeled using Rayleigh fading.

In the current chapter, the random fluctuation due to diffusive paths are represented as Rayleigh or Rician variables according to the environment.

In [9], time and frequency dispersion of UAC channel is represented by a model, which encompasses two separate modeling stages. First, the environment model is developed using the environmental data such as wind speed, sound speed profile, bottom loss characteristics and incorporates features such as surface wave model, internal wave model, tidal currents model, two-layer bottom interactions, and ambient noise. Second, 3-D ray tracing is used to develop the propagation model that includes effects such as range dependent bathymetry, branching at the water/sediment

11

interface, propagation through the sediment layer, range dependent sound speed, caustics, reflection from the moving sea surface, and motion of transmitter/receiver platforms.

In the current chapter, the effect of environment parameters and the propagation characteristics are incorporated in the deterministic and stochastic components of the arrived paths.

In [10], the random fluctuation of dominant eigen paths between transmitter and receiver is represented by the presence of smaller sub-eigen paths. The combination of eigen and sub-eigen paths is represented by Rician fading. In [11], signal to multipath ratio and signal fading statistics is presented. Turbulence of water causes change in signal phase and amplitude. Ray tracing is used to determine the deterministic component and phase and amplitude variation is placed on top of the deterministic components.

In the current chapter, the deterministic eigen components are first derived using Ray tracing and then the random fluctuation causing sub-eigen components are placed on top of the deterministic components. The combined effect of eigen and sub-eigen is represented as Gaussian, Rayleigh, or Rician variables.

In [12], [13], data is measured and the measured data is interpolated to determine channel impulse response (CIR). Both uncorrelated and correlated taps are considered. Pseudorandom binary signal is used as probe signal in the measurements.

2.3 Proposed UAC Channel Representation According to Environment

All possible UAC channel environments may be determined from the sensed channel environment parameters as described in chapter 2. The channel representations, once mapped from the environments will be more accurate since they are derived from the actual channel environments. In the proposed channel analysis, the following assumptions are made.

- The channel equations are derived in the time domain. The transmission frequency and bandwidth are considered as parameters defining the UAC environment [4].

- Power in terms of path loss in dB is considered for each path in the power delay profile.

- Time variation of channel is applied on top of the power delay profile.
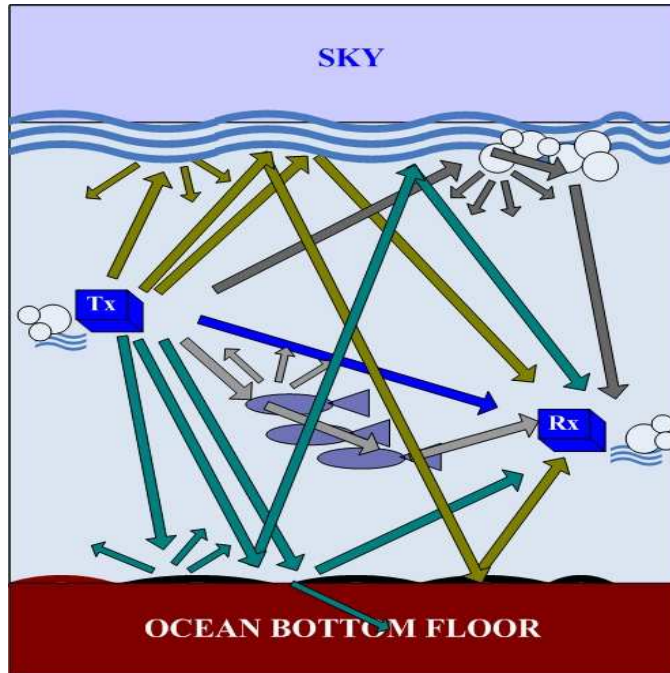
Figure 2.2 Underwater Acoustic Shallow Water Channel

- The individual scatters are assumed to be independent and identically distributed (i.i.d.) Gaussian random variables in the case of uncorrelated taps.

- Each dominant and its corresponding sub-eigenpaths arrive at the receiver at the same time.

- Line of Sight (LOS) path is considered to be present in each UAC environment.

The rest of this section is organized as follows. Subsection 2.3.1, presents the CIR and subsection 2.3.2, presents the fading characteristics of different UAC channels, according to each UAC environment. Subsection 2.3.3, briefly touches on the noise components and 2.3.4, on quasi-stationarity of UAC channels.

2.3.1 Channel Impulse Response of Underwater Acoustic Communication Channels

Let the transmitted signal be denoted by an impulse, $\delta(t)$, where δ represents a Dirac delta function. The UAC channel will produce multipaths that may vary in time. In a time invariant channel, the channel impulse response can be expressed as $h(\tau_{REF}) = \sum_{l=0}^{L-1} \alpha_l \delta(\tau_{REF} - \tau_l)$. The variables α_l and τ_l denote the attenuation coefficient and the time delay of the lth path respectively.

13
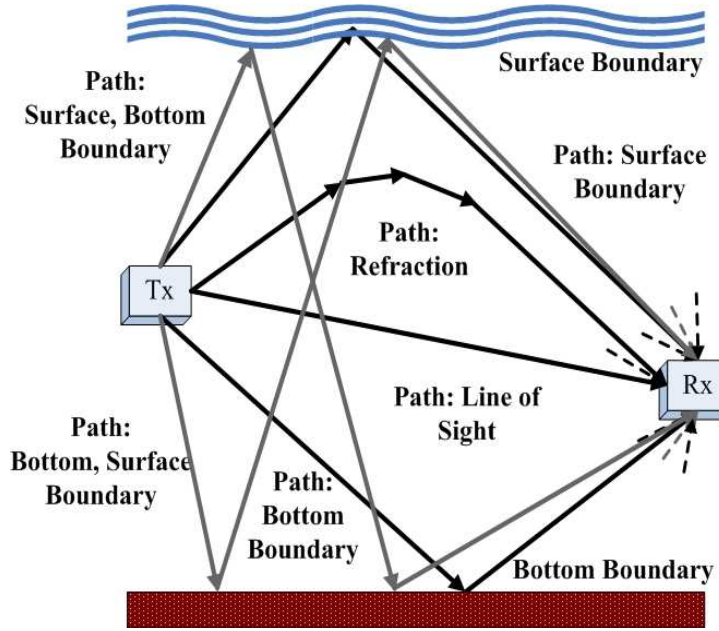
Figure 2.3 Single Path Originated from Each Group in UAC Shallow Channel

The variable L denotes the total number of multipaths, τ_{REF} is a time reference. In a time variant channel, this equation can be modified as below,

$$h(\tau_{REF}, t) = \sum_{l=0}^{L-1} \alpha_l(t)\delta(\tau_{REF} - \tau_l(t)). \qquad (2.1)$$

In an UAC channel, group of multipaths may consist of dominant paths, for examples, originating from reflections on the boundaries, also known as eigen paths [10, 14] accompanied by less dominant paths or sub-eigen paths, for example, originating from various scatters.

2.3.1.1 Shallow Channel Representation According to Environment

A generic shallow water channel is illustrated in Fig. 2.2. The shallow water UAC channel multipaths can be grouped according to their origination. In a shallow UAC channel environment, there may be five groups of eigen and sub-eigen paths. The first group of paths may result from surface only reflection and scatter, while the third group may result from bottom only reflection, bottom refraction, and scatter. The second group may include paths that reflect on both surface and bottom but the first reflection is on the surface. The fourth group may also include paths

reflecting on both surface and bottom but the first reflection is on the bottom. There may be scatters associated with these paths as well. Depending on the transmission range and depth, sound refraction through water layers may result in another group of eigen and sub-eigen paths. This fifth group may also include paths resulting from reflection, refraction, and scatter on marine life and other objects in the water medium. In addition, there may be a direct line of sight (LOS) that may depend on transmission range and depth. Equation (2.1) can be expanded to represent channel impulse response for all these five groups of paths as below.

$$
\begin{aligned}
h(t) \quad = \quad & \alpha_0(t)\delta(t) + \underbrace{\sum_{i=1}^{II}\left[\alpha_i(t)\delta(t-\tau_i(t))\right]}_{GROUP1} + \underbrace{\sum_{ii=II+1}^{I}\left[\alpha_{ii}(t)\delta(t-\tau_{ii}(t))\right]}_{GROUP2} \\
& + \underbrace{\sum_{j=I+1}^{JJ}\left[\alpha_j(t)\delta(t-\tau_j(t))\right]}_{GROUP3} + \underbrace{\sum_{jj=JJ+1}^{J}\left[\alpha_{jj}(t)\delta(t-\tau_{jj}(t))\right]}_{GROUP4} \\
& + \underbrace{\sum_{k=J+1}^{L-1}\left[\alpha_k(t)\delta(t-\tau_k(t))\right]}_{GROUP5}.
\end{aligned} \tag{2.2}
$$

Table 2.1 presents examples of dominant paths in these groups. Each group of (2.2) can be expanded into many eigen paths and their corresponding sub-eigen paths as in (2.3). Each eigen and its sub-eigen paths arrive at the same time at each delay.

$$
\begin{aligned}
GROUP_1 \quad = \quad & \left[\alpha_1(t)\delta(t-\tau_1) + \sum_{m_1=2}^{M_1-1}\alpha_{1m_1}(t)\delta(t-\tau_1)\right] \\
& + \left[\alpha_2(t)\delta(t-\tau_2) + \sum_{m_2=2}^{M_2-1}\alpha_{2m_2}(t)\delta(t-\tau_2)\right]... \\
& ...+ \left[\underbrace{\alpha_{II}(t)\delta(t-\tau_{II})}_{Eigenpath} + \underbrace{\sum_{m_{II}=2}^{M_{II}-1}\alpha_{IIm_{II}}(t)\delta(t-\tau_{II})}_{Sub-eigenpaths}\right].
\end{aligned} \tag{2.3}
$$

Fig. 2.3 illustrates one single dominant path originating in each group along with less dominant paths due to scatters. Solid line represents eigen paths and dashed line represents sub-

Table 2.1 The Five Groups and Their Respective Paths in Shallow Channel

Group	Paths in the Group
GROUP1	
GROUP2	
GROUP3	
GROUP4	
GROUP5	

eigen paths. In an ideal scenario, with a smooth surface and a smooth bottom boundary, the channel generated multipaths can be described as arriving from image sources [15]. Under this scenario, the range traversed by each path from source to destination denoted by $Range_{wv}$ can be expressed in terms of the distance between source and destination denoted by D, source and destination depth from surface denoted by z_s and z_r respectively, and water column height between surface and bottom denoted by H. There are four such image sources and are given by [15],

$$
\begin{aligned}
z_{1v} &= 2(v-1)H + z_s - z_r \\
z_{2v} &= 2(v-1)H + z_s + z_r \\
z_{3v} &= 2vH - z_s - z_r \\
z_{4v} &= 2vH - z_s + z_r.
\end{aligned}
\tag{2.4}
$$

Then the time delay of each multipath at the destination can be expressed as

$$
\tau_{wv} = \frac{Range_{wv}}{c},
\tag{2.5}
$$

16

where $w = 1, 2, 3, 4$ denotes the image source types and c denotes the sound velocity. The values of v can be $v = 1, 2, 3....$ If only path loss is considered and the sound velocity is considered constant (the value is provided in simulation), each multipath from individual image source will go through path loss given by [15],

$$TL_{wv} = 20 \log Range_{wv} + \beta Range_{wv}, \tag{2.6}$$

where β is the water absorption coefficient with units of dB/Km. In this ideal scenario, in the absence of scatters, each path arriving from each image source will only consist of a dominant path. The amplitude of each path derived from (2.6) can be expressed as,

$$A_{wv} = 10^{\frac{TL_{wv}}{10}}. \tag{2.7}$$

In case of a smooth surface and a smooth bottom and in the absence of sub-eigen paths, there will only be dominant paths; the CIR will consist of one LOS, one surface reflected path (GROUP1), one bottom reflected path (GROUP3), multiple paths in GROUP2 and multiple reflected paths in GROUP4. Therefore, in the absence of sub-eigen paths, (2.2) becomes,

$$
\begin{aligned}
h(t) \;=\;& \alpha_0(t)\delta(t) + \underbrace{\left[\alpha_1(t)\delta(t-\tau_1)\right]}_{GROUP1} + \underbrace{\sum_{ii=II+1}^{I}\left[\alpha_{ii}(t)\delta(t-\tau_{ii}(t))\right]}_{GROUP2} \\
&+ \underbrace{\left[\alpha_{JJ}(t)\delta(t-\tau_{JJ}(t))\right]}_{GROUP3} + \underbrace{\sum_{jj=JJ+1}^{J}\left[\alpha_{jj}(t)\delta(t-\tau_{jj}(t))\right]}_{GROUP4} \\
&+ \underbrace{\sum_{k=J+1}^{L-1}\left[\alpha_k(t)\delta(t-\tau_k(t))\right]}_{GROUP5}.
\end{aligned} \tag{2.8}
$$

The above ideal scenarios generate *deterministic path components.*

Now, let the smooth surface and smooth bottom be replaced by surface waves and a rough bottom respectively. Let the following conditions be assumed. (a) the transmitter and the receiver are stationary. (b) the water column height (vertical distance between surface and bottom) remain

the same for both transmitter and receiver. (c) the acoustic wave length is much larger than the wave surface and bottom reflector elements (d) the dominant paths arrive at the receiver, and (e) the delays of dominant paths are calculated using image sources, although, the surface movement due to surface waves and the presence of rough bottom may vary these dominant path delays .

The scatters induced by surface waves and rough bottom may produce sub-eigen paths that can be represented as *stochastic path components* along with each dominant path. Then (2.8) becomes,

$$
\begin{aligned}
h(t) \;=\; & \alpha_0(t)\delta(t) + \underbrace{\left[\alpha_1(t)\delta(t-\tau_1) + \sum_{m_1=2}^{M_1-1}\alpha_{1m_1}(t)\delta(t-\tau_1)\right]}_{GROUP1} \\
& + \underbrace{\sum_{ii=II+1}^{I}\left[\alpha_{ii}(t)\delta(t-\tau_{ii}(t)) + \sum_{mm_{ii}=2}^{MM_{ii}-1}\alpha_{iimm_{ii}}(t)\delta(t-\tau_{ii}(t))\right]}_{GROUP2} \\
& + \underbrace{\left[\alpha_{JJ}(t)\delta(t-\tau_{JJ}) + \sum_{p_{JJ}=2}^{P_{JJ}-1}\alpha_{JJp_{JJ}}(t)\delta(t-\tau_3)\right]}_{GROUP3} \\
& + \underbrace{\sum_{jj=JJ+1}^{J}\left[\alpha_{jj}(t)\delta(t-\tau_{jj}(t)) + \sum_{pp_{jj}=2}^{PP_{jj}-1}\alpha_{jjpp_{jj}}(t)\delta(t-\tau_{jj}(t))\right]}_{GROUP4} \\
& + \underbrace{\sum_{k=J+1}^{L-1}\left[\alpha_k(t)\delta(t-\tau_k(t)) + \sum_{q_k=2}^{Q_k-1}\alpha_{kq_k}(t)\delta(t-\tau_k)\right]}_{GROUP5}.
\end{aligned}
\tag{2.9}
$$

Let the combination of each dominant and its corresponding sub-eigenpaths be denoted as $R_{index}(t)$. Using (2.9), $h(t)$ can be expressed as the sum of variables as below,

$$
\begin{aligned}
h(t) = h_{S_{BET}}(t) \;=\; & \alpha_0(t)\delta(t) + \underbrace{R_1(t)}_{GROUP1} + \underbrace{R_{II+1}(t) + R_{II+2}(t) + ... + R_I(t)}_{GROUP2} \\
& + \underbrace{R_{JJ}(t)}_{GROUP3} + \underbrace{R_{JJ+1}(t) + R_{JJ+2}(t) + ... + R_J(t)}_{GROUP4} \\
& + \underbrace{R_{J+1}(t) + R_{J+2}(t) + ...R_{L-1}(t)}_{GROUP5},
\end{aligned}
\tag{2.10}
$$

18

where $GROUP_1$ denotes the surface only reflected/scattered paths, $GROUP_3$ denotes bottom only reflected/scattered paths, and $GROUP_5$ denotes paths corresponding to refraction in the medium and refraction/reflection/scatter on other objects. The $GROUP_2$ represents the surface/bottom reflected/scattered paths while $GROUP_4$ represents the bottom/surface reflected/scattered paths. It is to be noted that arrival time of groups of paths and paths within the groups may vary.

According to Fig. 2.1, the shallow channel can be classified into three broad categories. They are close to surface, close to bottom, and in between channels. The surface and bottom roughness dictates further classification of shallow channel environment. The channel representations for these environments are given below.

A channel that represents a shallow channel communication environment in between surface and bottom, can be expressed by (2.10), where $h_{S_{BET}}(t)$ denotes the channel impulse response. Depending on how close to the surface and/or to the bottom the source and destination are, both CIR, h_{S_S} and h_{S_B}, for close to surface and close to bottom environment respectively, may have paths in GROUP1 through GROUP4.

- *Shallow Channel Close to Rough Surface:* Similar to a channel somewhere in between surface and bottom, a close to rough surface shallow channel can be expressed as, (2.10). If however, the bottom *is far away from* the surface in a close to rough surface communication environment, strictly *ideally*, the bottom reflected dominant paths may disappear due to higher loss and/or longer delay in arriving. Under such scenario, GROUP3 will be empty, and in GROUP2 and GROUP4 only surface scattered sub-eigen paths will dominate. Let the combination of scattered sub-eigen paths generated only from the surface corresponding to each negligible surface/bottom reflected dominant paths be denoted by the variables R'_{index}. In that case, (2.10) will reduce to $h_{S_S}(t)$ as below,

$$
\begin{aligned}
h_{S_S}(t) \;=\; & \alpha_0(t)\delta(t) + \underbrace{R_1(t)}_{GROUP1} + \underbrace{R'_{II+1}(t) + R'_{II+2}(t) + ... + R'_I(t)}_{GROUP2} \\
& + \underbrace{R'_{JJ+1}(t) + R'_{JJ+2}(t) + ... + R'_J(t)}_{GROUP4} \\
& + \underbrace{R_{J+1}(t) + R_{J+2}(t) + ...R_{L-1}(t)}_{GROUP5}.
\end{aligned}
\tag{2.11}
$$

The CIR in a close to a rough surface for long, short, and medium range transmission can be expressed as $h_{S_{RS/L}}(t)$, $h_{S_{RS/S}}(t)$, and $h_{S_{RS/M}}(t)$ respectively. The expressions for these are derived from (2.11). In a *long range close to rough surface transmission*, the sub-eigen paths due to scatter are negligible and hence may result in GROUP2 and GROUP4 of (2.11) to be empty. Surface reflected dominant paths may dominate over the surface scattered sub-eigen paths. Let $R_1''(t)$ denote the combination of surface reflected dominant path and negligible sub-eigen scatters. There may be horizontal variation of sound speed resulting in scatter and/or dominant paths due to refraction. Even though some reflection and scatters may occur due to objects in the medium, in a long range these may/may not be negligible. Hence GROUP5 may not be empty. Using (2.11), the CIR for transmission can be written as,

$$h_{S_{RS/L}}(t) \quad = \quad \alpha_0(t)\delta(t) + \underbrace{R_1''(t)}_{GROUP1} + \underbrace{R_{J+1}(t) + R_{J+2}(t) + ...R_{L-1}(t)}_{GROUP5}. \qquad (2.12)$$

In a *short range close to rough surface transmission*, surface scattered sub-eigen paths will be dominating. Therefore, GROUP2 and GROUP4 will not be empty. Due to short range there may not be horizontal sound velocity variation but the presence of other objects in the water may result in reflection and scatters. If the range is short, the reflection/scatter on objects in the medium may be significant. Therefore, GROUP5 may not be empty. The resulting CIR, $h_{S_{RS/S}}(t)$ will be as same as (2.11) with $R_1(t)$ having more dominant sub-eigen paths. In a *medium range transmission*, there may be dominant paths due to reflection and sub-eigen paths due to scatter. If the range is medium, the reflection/scatter on objects in the medium may be significant. The CIR of such a channel, $h_{S_{RS/M}}(t)$ will be as same as (2.11).

- *Shallow Channel Close to Smooth Surface:* In case of smooth surface, there will be no sub-eigen paths due to scatters on surface or bottom. Hence when the bottom is far away from the surface, ideally, GROUP2 and GROUP4 will be empty. For *medium range transmis-*

sion, (2.11) can be expressed as,

$$h_{S_{SS/M}}(t) = \alpha_0(t)\delta(t) + \underbrace{R_1'''(t)}_{GROUP1} + \underbrace{R_{J+1}(t) + R_{J+2}(t) + ...R_{L-1}(t)}_{GROUP5}, \qquad (2.13)$$

where R_1''' denotes surface only reflected dominant path without any sub-eigen paths. Equation (2.13) also represents *short range* and *long range* close to smooth surface channels.

- *Shallow Channel Close to Rough Bottom:* Similar to channels close to the surface, a close to rough bottom channel can be expressed as (2.10). If the surface is far away from the bottom, *ideally*, the surface reflected dominant paths will disappear due to higher loss and/or due to delay in arriving and (2.10) will reduce to $h_{S_B}(t)$ as shown in (2.14). Variable $R'_{Bindex}(t)$ denotes the combination of sub-eigen scatters generated only from the bottom corresponding to each negligible surface/bottom reflected dominant path.

$$\begin{aligned} h_{S_B}(t) \;=\; & \alpha_0(t)\delta(t) + \underbrace{R'_{BII+1}(t) + R'_{BII+2}(t) + ... + R'_{BI}(t)}_{GROUP2} \\ & \underbrace{R_{JJ}(t)}_{GROUP3} + \underbrace{R'_{BJJ+1}(t) + R'_{BJJ+2}(t) + ... + R'_{BJ}(t)}_{GROUP4} \\ & + \underbrace{R_{J+1}(t) + R_{J+2}(t) + ...R_{L-1}(t)}_{GROUP5}. \end{aligned} \qquad (2.14)$$

The CIR in a close to a rough bottom for long, short, and medium range transmission can be expressed as $h_{S_{RB/L}}$, $h_{S_{RB/S}}$, and $h_{S_{RB/M}}$ respectively. In a close to rough bottom shallow channel, in addition to bottom reflection, different bottom composition may produce refracted scatters in GROUP2, GROUP3 and GROUP4.In *long range transmissions*, these scatters may not have significant contribution and so, GROUP2 and GROUP4 may be empty. Then (2.14) becomes,

$$h_{S_{RB/L}}(t) \;=\; \alpha_0(t)\delta(t) + \underbrace{R''_{JJ}(t)}_{GROUP3} + \underbrace{R_{J+1}(t) + R_{J+2}(t) + ...R_{L-1}(t)}_{GROUP5}, \qquad (2.15)$$

where $R''_{JJ}(t)$ denotes combination of bottom reflected dominant path and negligible sub-eigen scatters. Different marine life and other objects on the ocean floor may produce scatters due to reflection and refraction. In long range transmission these scatters may not be significant but in short and medium range transmission, these scatters may be dominant. In short and medium range transmissions, strong bottom reflected/refracted scatters may also be dominant. Therefore, *short range close to rough bottom transmission*, can be expressed as (2.14), denoted by $h_{S_{RB/S}}(t)$, where $R_{JJ}(t)$ will contain more dominant sub-eigen paths. A *medium range close to rough bottom transmission* can also be expressed as (2.14), and denoted by $h_{S_{RB/M}}(t)$.

- *Shallow Channel Close to Smooth Bottom:* In case of smooth bottom, there will be no sub-eigen paths due to scatters on the bottom. Hence for *medium range transmission*, (2.14) can be expressed as,

$$h_{S_{SB/M}}(t) \quad = \quad \alpha_0(t)\delta(t) + \underbrace{R'''_{JJ}(t)}_{GROUP3} + \underbrace{R_{J+1}(t) + R_{J+2}(t) + ...R_{L-1}(t)}_{GROUP5}, \qquad (2.16)$$

where $R'''_{JJ}(t)$ denotes bottom only reflected dominant path without any sub-eigen paths. Equation (2.16) also represents *short range* and *long range* close to smooth bottom channels denoted by $h_{S_{SB/S}}(t)$ and $h_{S_{SB/L}}(t)$ respectively.

2.3.1.2 Deep Channel Representation According to Environment

If only path loss is considered, in a deep channel, each multipath will go through path loss given by [15] and will arrive at various delays. In a deep channel, when the sound velocity is *not* constant, the first group of multipaths represents the steepest paths, the second group represents grazing paths for isothermal channel or axis paths for SOFAR channel, and the third

group represents bottom reflected multipaths [15]. These paths are presented below as,

$$
\begin{aligned}
h_D(t) \;=\; & \underbrace{\sum_{i_D=1}^{I_D}\left[\alpha_{i_D}(t)\delta(t-\tau_{i_D}) + \sum_{m_{D_{i_D}}=2}^{M_{D_{i_D}}-1}\alpha_{i_D m_{D_{i_D}}}(t)\delta(t-\tau_{i_D})\right]}_{GROUP1} + \\[2mm]
& \underbrace{\sum_{j_D=I_D+1}^{J_D}\left[\alpha_{j_D}(t)\delta(t-\tau_{j_D}) + \sum_{p_{D_{j_D}}=2}^{P_{D_{j_D}}-1}\alpha_{j_D p_{D_{j_D}}}(t)\delta(t-\tau_{j_D})\right]}_{GROUP2} \\[2mm]
& + \underbrace{\sum_{k_D=J_D+1}^{L_D-1}\left[\alpha_{k_D}(t)\delta(t-\tau_{k_D}) + \sum_{q_{D_{k_D}}=2}^{Q_{D_{k_D}}-1}\alpha_{k_D q_{D_{k_D}}}(t)\delta(t-\tau_{k_D})\right]}_{GROUP3}.
\end{aligned}
\tag{2.17}
$$

Although (2.17) considers both eigen and sub-eigen components, the existence of a fewer number of scatters in a deep channel may only cause dominant eigen components to exist. The deep channel can be broadly categorized into SOFAR and other types of deep channels.

- *SOFAR Channel:* The CIR in a SOFAR channel for long, medium, and short range transmission can be derived from (2.17). For long, medium, and short range transmission, not close to surface or bottom, the scatters may be insignificant resulting in only dominant components as below,

$$
\begin{aligned}
h_{D_{SOF/L,M,S}}(t) \;=\; & \underbrace{\sum_{i_D=1}^{I_D}\left[\alpha_{i_D}(t)\delta(t-\tau_{i_D})\right]}_{GROUP1} + \\[2mm]
& \underbrace{\sum_{j_D=I_D+1}^{J_D}\left[\alpha_{j_D}(t)\delta(t-\tau_{j_D})\right]}_{GROUP2} \\[2mm]
& + \underbrace{\sum_{k_D=J_D+1}^{L_D-1}\left[\alpha_{k_D}(t)\delta(t-\tau_{k_D})\right]}_{GROUP3}.
\end{aligned}
\tag{2.18}
$$

23

However, for SOFAR channels close to surface or bottom, there may be some significant scatters that would result in (2.17). In both cases, GROUP1 denotes the steepest paths, GROUP2 denotes the axis paths, and GROUP3 denotes the bottom reflected paths.

- *Other Deep Channels, Isothermal Deep Channel:* The CIR in isothermal channels for long, medium, and short range transmission can be expressed as $h_{D_{ISO/L,M,S}}(t)$. For long, medium, and short range transmission, not close to surface or bottom, the scatters may be insignificant resulting in mostly dominant eigen paths similar to (2.18). For channels close to surface or bottom, the presence of significant scatters may result in an equation similar to (2.17). The first group of paths denote the steepest paths, the second one grazing paths, and the third one denotes the bottom reflected paths.

2.3.2 Fading Characteristics, Probability Distribution, Relationship between Fading and Channel Parameters for Wide Sense Stationary (WSS) Uncorrelated Tap Channel

In determining the fading characteristics and probability distribution of various UAC channels, the following assumptions are made.

- Channel paths are considered at each sample time.

- In the absence of a natural path at any sample, a path is generated by interpolating neighboring paths.

- The symbol period is considered large enough to encapsulate all the significant arrived multipaths.

After convolving with the channel the received signal, using (2.1), can be expressed as,

$$r(t) = \alpha_0(t)s(t) + \sum_{l=1}^{L-1} \alpha_l(t)s(t - \tau_l), +n_1(t) + n_2(t), \tag{2.19}$$

where the variables $s(t)$, $n_1(t)$ and $n_2(t)$ denote the transmitted signal, frequency independent and frequency dependent noise respectively. When each arrived path is i.i.d. Gaussian, the following

24

conditions may occur. Case a) When the dominant path to less dominant multipath ratio, which is denoted by signal to multipath ratio, SMR is less than 1, i.e. $SMR \ll 1$ the amplitude of the envelop of paths follows Rayleigh distribution [10]. Case b) When the eigen path component dominates, as in the case of direct LOS, $SMR \gg 1$, and the amplitude of the envelop of the paths follows Gaussian distribution. Case c) When the dominant path is comparable to the less dominant paths, such that the dominant path exists as one single large path compared to the less dominant paths, i.e. $SMR \approx 1$ the amplitude of the envelop of the paths follows Rician distribution.

The symbol is sampled at each arrived multipath. Each path at each sample location is a combination of eigen and sub-eigen paths. At each sample location, these simultaneous paths can add constructively or destructively. The amplitude of the resultant path at each sample location can be subjected to one of the three conditions mentioned above resulting in Gaussian, Rayleigh or Rician fading distribution. Let each sample represent a variable, G, RL, or RC identifying an amplitude with either Gaussian, Rayleigh, or Rician distribution respectively.

These variables are an indication of the channel environment and are directly related to the environment parameters. For example, the value of the range parameter (short/medium/long) and/or depth parameter (close to surface/close to bottom etc.) may determine the variable at each sample location to be G, RL, or RC.

If the channel delay spread is long and some paths arrive outside of the symbol duration, those outside paths will also contain combination of dominant and sub-eigen paths resulting in an amplitude variation, the distribution of which can be presented by a Gaussian, Rayleigh, or Rician variable according to the channel environment. Fig. 2.4 illustrates the relationship between the paths, the symbol duration, and the sample time. The bold lines represent dominant eigen and dashed lines represent sub-eigen paths. Each arrived path within symbol duration and outside of symbol duration may consist of one dominant and/or one/multiple sub-eigen paths. The received signal representation in terms of Gaussian, Rayleigh, or Rician fading, for the UAC channels described in the last sub-section are given below. The SMR for *each path* can be expressed as,

$$SMR_{Path} = \frac{|Eigen_{path}|}{|\sum SubEigen_{Path}|}.$$ (2.20)
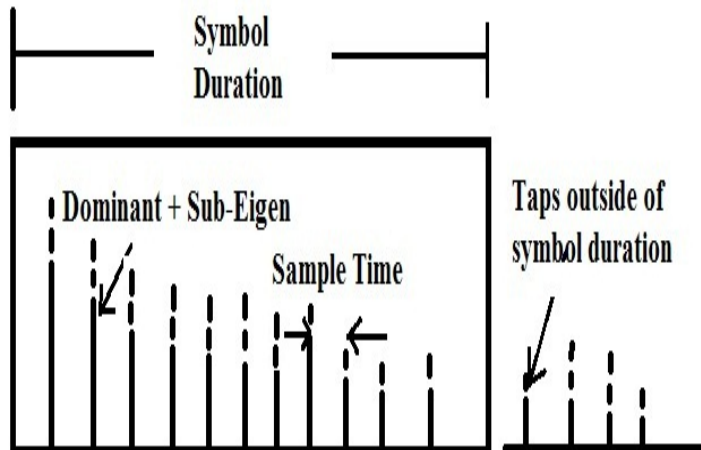
Figure 2.4 Channel Paths, Symbol Duration, and Sample Time

Depending on the value of SMR_{Path} of each path, the combination of eigen and sub-eigen components will follow Rayleigh, Gaussian, or Rician distribution. If the symbol duration encapsulate all paths, then,

$$SMR_{Symbol} = \frac{|LOS|}{|\sum Other_{Path}|}. \tag{2.21}$$

Depending on the value of SMR_{Symbol}, the combination of all paths (each path a combination of eigen and sub-eigen components) within the symbol duration will follow Rayleigh, Gaussian, or Rician distribution.

Fading characteristics of the shallow channel will be addressed first below, followed by the fading characteristics of the deep channel.

2.3.2.1   Fading Characteristics of Shallow Channel

- *Shallow Channel Close to Rough Surface:*   The received signal in a close to a rough surface for long, short, and medium range transmission can be expressed as $r_{S_{RS/L}}(t)$, $r_{S_{RS/S}}(t)$, and

26

$r_{S_{RS/M}}(t)$ respectively. Using (2.12), in *long range* transmission,

$$
\begin{aligned}
r_{S_{RS/L}}(t) \;=\; & G_0 + \Big[\ \underbrace{RC_1''(t)}_{Rician(GROUP1)}\ \Big] \\
& + \Big[\ \underbrace{RC_{J+1}(t) + RC_{J+2}(t) + ...RC_{L-1}(t)}_{Rician(GROUP5)}\ \Big] \\
& n_1(t) + n_2(t),
\end{aligned}
\tag{2.22}
$$

where $RC_1''(t)$ represents the Rician envelop corresponding to surface reflected dominant path and sub-eigen paths. Each of RC_Js represent a Rician envelop corresponding to scatter/dominant paths due to refraction from sound speed variation and/or reflection/refraction or scatter on objects in the medium. The surface reflected path will produce Rician fading if the scatters are not negligible otherwise it will produce Gaussian fading. In a *short range* transmission, using (2.11), the received signal can be expressed as,

$$
\begin{aligned}
r_{S_{RS/S}}(t) \;=\; & G_0 + \Big[\ \underbrace{RL_1(t)}_{Rayleigh(GROUP1)}\ \Big] \\
& + \Big[\ \underbrace{RL'_{II+1}(t) + RL'_{II+2}(t) + ... + ... + RL'_I(t)}_{Rayleigh(GROUP2)}\ \Big] \\
& + \Big[\ \underbrace{RL'_{JJ+1}(t) + RL'_{JJ+2}(t) + ... + RL'_J(t)}_{Rayleigh(GROUP4)}\ \Big] \\
& + \Big[\ \underbrace{RL_{J+1}(t) + RL_{J+2}(t) + ...RL_{L-1}(t)}_{Rayleigh(GROUP5)}\ \Big] \\
& + n_1(t) + n_2(t),
\end{aligned}
\tag{2.23}
$$

where $RL_1(t)$ represents the Rayleigh envelop corresponding to surface reflected path and dominant scattered sub-eigen paths. The RL'_{II}s and RL'_{JJ}s represent Rayleigh envelop of combination of surface scattered sub-eigen paths corresponding to each negligible surface/bottom reflected (first reflection on surface for GROUP2 and first reflection on bottom for GROUP4) dominant path. Each of RL_Js represent a Rayleigh envelop corresponding to scatter/dominant paths due to refraction from sound speed variation and/or reflec-

tion/refraction/scatter on objects in the medium. In a *medium range*, paths in GROUP5 will result in some Rician variables and some Rayleigh variables. Therefore, using (2.11),

$$
\begin{aligned}
r_{S_{RS/M}}(t) \quad = \quad & G_0 + \Big[\underbrace{RC_1(t)}_{Rician(GROUP1)} \Big] \\
& + \Big[\underbrace{RL'_{II+1}(t) + RL'_{II+2}(t) + ... + RL'_I(t)}_{Rayleigh(GROUP2)} \Big] \\
& + \Big[\underbrace{RL'_{JJ+1}(t) + RL'_{JJ+2}(t) + ... + RL'_J(t)}_{Rayleigh(GROUP4)} \Big] \\
& + \Big[\underbrace{RC_{J+1}(t) + RC_{J+2}(t) + ...RC_{J+J'}(t)}_{Rician(GROUP5)} \Big] \\
& + \Big[\underbrace{RL_{J'+1}(t) + RL_{J'+2}(t) + ...RL_{L-1}(t)}_{Rayleigh(GROUP5)} \Big] \\
& + n_1(t) + n_2(t),
\end{aligned}
\tag{2.24}
$$

where $RC_1(t)$ represents the Rician envelop of dominant surface reflected path and sub-eigen scatters.

- *Shallow Channel Close to Smooth Surface:* In case of smooth surface, the received signal in long, short, and in medium range can be denoted as, $r_{S_{SS/L}}(t)$, $r_{S_{SS/S}}(t)$, and $r_{S_{SS/M}}(t)$ respectively. The equations for long, short, and medium range will be same and using (2.13) can be expressed as,

$$
\begin{aligned}
r_{S_{SS/L,M,S}}(t) \quad = \quad & G_0 + \Big[\underbrace{G_1''''(t)}_{Gaussian(GROUP1)} \Big] \\
& + \Big[\underbrace{G_{J+1}(t) + G_{J+2}(t) + ...G_{L-1}(t)}_{Gaussian(GROUP5)} \Big] + n_1(t) + n_2(t),
\end{aligned}
\tag{2.25}
$$

where G'''' denotes the Gaussian variable corresponding to surface only reflected dominant path without any sub-eigen paths. The variable, G_Js denote Gaussian variables representing dominant paths due to refraction from sound speed variation and/or reflection/refraction on objects in the medium.

- *Shallow Channel Close to Rough Bottom:* The received signal in a close to a rough bottom for long, short, and medium range transmission can be expressed as $r_{S_{RB/L}}$, $r_{S_{RB/S}}$, and $r_{S_{RB/M}}$ respectively. In a long range transmission, the bottom reflected/refracted paths will produce Rician fading, if the scatters are not negligible otherwise it will produce Gaussian fading. Therefore, using (2.15),

$$
r_{S_{RB/L}}(t) = G_0 + \left[\underbrace{RC''_{JJ}(t)}_{Rician(GROUP3)} \right] + \left[\underbrace{RC_{J+1}(t) + RC_{J+2}(t) + ...RC_{L-1}(t)}_{Rician(GROUP5)} \right]
$$
$$
+ n_1(t) + n_2(t), \tag{2.26}
$$

where RC''_{JJ} represents the Rician envelop corresponding to bottom reflected dominant path and negligible sub-eigen scatters. Using (2.14),

$$
r_{S_{RB/S}}(t) = G_0 + \left[\underbrace{RL'_{BII+1}(t) + RL'_{BII+2}(t) + ... + RL'_{BI}(t)}_{Rayleigh(GROUP2)} \right] + \left[\underbrace{RL_{JJ}(t)}_{Rayleigh(GROUP3)} \right]
$$
$$
+ \left[\underbrace{RL'_{BJJ+1}(t) + RL'_{BJJ+2}(t) + ... + RL'_{BJ}(t)}_{Rayleigh(GROUP4)} \right]
$$
$$
+ \left[\underbrace{RL_{J+1}(t) + RL_{J+2}(t) + ...RL_{L-1}(t)}_{Rayleigh(GROUP5)} \right]
$$
$$
+ n_1(t) + n_2(t), \tag{2.27}
$$

where RL'_{BII}s and RL'_{BJJ}s represent Rayleigh envelops of combination of bottom scattered sub-eigen paths corresponding to each negligible surface/bottom reflected path (first reflection on surface for GROUP2 and first reflection on bottom for GROUP4). In a medium range, paths in GROUP5 will result in some Rician variables and some Rayleigh variables. Therefore,

using (2.14)

$$
\begin{aligned}
r_{S_{RB/M}}(t) \;=\;& G_0 + \Big[\, \underbrace{RL'_{BII+1}(t) + RL'_{BII+2}(t) + ... + RL'_{BI}(t)}_{Rayleigh(GROUP2}\, \Big] \\
&+ \underbrace{RC_{JJ}(t)}_{Rician(GROUP3)} \; + \Big[\, \underbrace{RL'_{BJJ+1}(t) + ... + RL'_{BJ}(t)}_{Rayleigh(GROUP4)}\, \Big] \\
&+ \Big[\, \underbrace{RC_{J+1}(t) + RC_{J+2}(t) + ...RC_{J+J'}(t)}_{Rician(GROUP5)} \\
&+ \underbrace{RL_{J'+1}(t) + RL_{J'+2}(t) + ...RL_{L-1}(t)}_{Rayleigh(GROUP5)}\, \Big] \\
&+ n_1(t) + n_2(t),
\end{aligned}
\tag{2.28}
$$

where $RC_{JJ}(t)$ represents the Rician variable corresponding to the bottom reflected dominant path and sub-eigen scatters.

- *Shallow Channel Close to Smooth Bottom:* In case of smooth bottom, the equations can be expressed as $r_{S_{SB/L}}$, $r_{S_{SB/S}}$, and $r_{S_{SB/M}}$. Expressions for short, medium, and long range will be same and using (2.16) can be expressed as,

$$
\begin{aligned}
r_{S_{SB/S}}(t) \;=\;& G_0 + \Big[\, \underbrace{G'''_{JJ}(t)}_{Gaussian(GROUP3)}\, \Big] \\
&+ \Big[\, \underbrace{G_{J+1}(t) + G_{J+2}(t) + ...G_{L-1}(t)}_{Gaussian(GROUP5)}\, \Big] + n_1(t) + n_2(t),
\end{aligned}
\tag{2.29}
$$

where G'''_{JJ} represents the Gaussian variable corresponding to bottom reflected dominant path.

- *Shallow Channel in between Surface and Bottom:* The received signal in an environment between surface and bottom will be affected by both surface and the bottom. The type of channel for long, short, and medium range transmission can be expressed as $r_{S_{BET/L}}$, $r_{S_{BET/S}}$, and $r_{S_{BET/M}}$ respectively. The equation for $r_{S_{BET/L}}$ can be expressed as a combination of $r_{S_{SS/L}}$ and $r_{S_{SB/L}}$, when both surface and the bottom are smooth. If either or both are rough, the equations can be modified to include more scatters. Similarly, $r_{S_{BET/S}}$ will be a
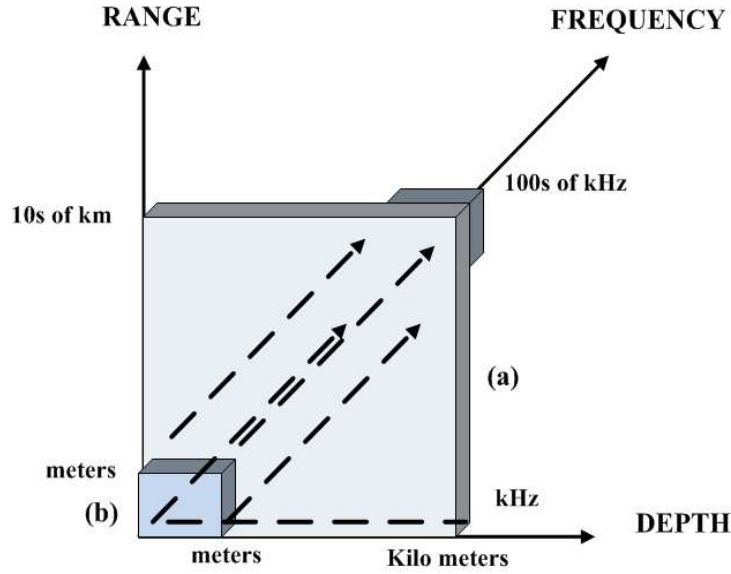
Figure 2.5 Shallow Channel, (a) Long Range, High Depth, Low Frequency Rician Zone, (b) Short Range, Low Depth, High Frequency Rayleigh Zone

combination of $r_{S_{SS/S}}$ and $r_{S_{SB/S}}$ and $r_{S_{BET/M}}$ will be a combination of $r_{S_{SS/M}}$ and $r_{S_{SB/M}}$. Rough surface/bottom will add scatters and equations will change accordingly. In a clear, unobstructed channel, the increase of transmission range and water column depth will produce dominant components. If the transmission is close to surface/bottom or there are smaller objects in the water, the resulting scatters combined with the dominant component may produce Rician fading. With farther increase of range and depth, scattering effect may be minimal and the Rician may become Gaussian only fading. In a clear, unobstructed short range and low water column depth channels, there will be dominant components. But due to the closeness of the two boundaries, and the shorter range to travel, the scattering components will be significant and the scatters will be comparable to the dominant components, resulting in Rayleigh fading. Fig. 2.5 illustrates this characteristics.

2.3.2.2   Fading Characteristics in Deep Channel

Deep channel transmission will result in Gaussian fading due to the presence of noise, if the transmission happens far from surface/bottom boundaries, and the objects in the transmission

31

Table 2.2 Self and Ambient Noise in UAC

Self Noise	Machinery Noise	Flow Noise	Cavitation	
	Pumps, reduction gears, power plant, etc.	Relative motion between object and the water	Bubble collapse	
Ambient Noise	Hydrodynamic	Seismic	Biological	Ocean Traffic
	Movement of water	Movement of earth	Marine life	Other boats

path are scarce. If however, the deep channel is close to surface/bottom, the fading characteristics of close to surface, close to bottom or in between channels may apply.

2.3.3 Frequency Dependent and Independent Noise

Table 2.2 presents the possible noise in UAC channel. Some of these noise is frequency independent and can be considered under, $n_1(t)$ as Additive White Gaussian Noise (AWGN) with zero mean and normal distribution. However, some of the noise in Table 2.2 can be frequency dependent, and if the operating transmission frequency is as same as the frequencies of any of these noise sources, the transmitted signal will be affected. Frequency dependent noise is included under $n_2(t)$.

2.3.4 Fading Characteristics, Distribution, Relationship between Fading and Channel Parameters for Quasi-stationary Channels

In UAC channel, wide sense stationary (WSS) assumption is not always true [11], [13], [12]. When the transmitter and the receiver or their platforms are moving, the various taps can be correlated at different delays. There are different approaches to address non-WSS channels. One method is to consider the channel as quasi-WSS, i.e. the channel is WSS within a certain time and band of frequency. Another way of dealing with non-WSS is to define time and frequency dependent scattering functions [12]. In this chapter, the channels considered are WSS.

2.4 SNR Analysis

From the equations (2.22) through (2.29), it can be concluded that the received signal in any underwater environment of Fig. 2.1 is a summation/combination of Gaussian random variables (RV), Rician RVs, and Rayleigh RVs. Let the summation of Gaussian RVs, Rician RVs, and Rayleigh RVs be denoted as G_{SUM}, R_{SUM}, and RL_{SUM} respectively. Therefore, the pdf of the received signal will be equal to the pdf of an RV that is a summation of G_{SUM}, R_{SUM}, and RL_{SUM} or any combination of them. If the RV representing the received signal is denoted by RV_{REC}, then

$$RV_{REC} = G_{SUM} + R_{SUM} + RL_{SUM} \tag{2.30}$$

Although RV_{REC} is expressed in (2.30) as summation of Gaussian, Rayleigh, or Rician variables, RV_{REC} represents the resultant after the vectorial addition of all paths within symbol duration. Since every path is an i.i.d. Gaussian, the resultant amplitude, i.e. $|RV_{REC}|$ will follow any one of Gaussian, Rayleigh or Rician distributions. Rician fading is governed by two parameters, K, and Ω, which can be expressed as,

$$K = \frac{P_d}{\sum_{pi=1}^{LL-1} P_{pi}}, \tag{2.31}$$

$$\Omega = P_d + \sum_{pi=1}^{LL-1} P_{pi}, \tag{2.32}$$

where P_d represents the power of the dominant path, and P_{pi}, the power of each less dominant path. Clearly, when the power of any path is determined by the transmission loss in (2.6) and by the equation for α, the path powers will depend on R, H, and f. According to the UAC environment, R, H, f will vary resulting in different values of K and Ω. When $K \approx 0$ or $K \ll 1$, the denominator or the sum of powers of less dominant paths will be greater than the power of the dominant path, the received signal will follow Rayleigh fading. For $K \geq 1$, the received signal will follow Rician statistics. For $K \gg 1$, the signal will follow Gaussian statistics. The signal to noise ratio (SNR)

can be expressed as,

$$SNR \quad = \quad \frac{SignalPower}{NoisePower} \tag{2.33}$$
$$= \frac{|\sum Path|^2}{NoisePower}.$$

Let the AWGN noise variance and the frequency dependent noise variance be denoted as, σ^2 and N_{otr} respectively. Therefore, (2.33) can be expressed as,

$$SNR = \frac{(|RV_{REC}|)^2}{\sigma^2 + N_{otr}} \tag{2.34}$$

or using (2.19)

$$SNR = \frac{(|\sum_{l=0}^{L-1} \alpha_l(t)s(t-\tau_l)|)^2}{\sigma^2 + N_{otr}}. \tag{2.35}$$

The eigen and sub-eigen paths will vary in different environments. Hence the SNR will vary according to each environment. The numerator of (2.35) will be the square of Rayleigh or Rice or Gaussian variable and the denominator will be the summation of Gaussian variance and variance of noise component, N_{otr}. The square of Rayleigh variable gives exponential distribution and the square of Rician variable gives non-chi square distribution and hence can be expressed as, RV_{EXP} and RV_{CHI} respectively. Therefore, when RV_{REC} is a Rayleigh or Rician variable, SNR can be expressed as SNR_{EXP} and SNR_{CHI} respectively as shown below.

$$SNR_{EXP} = \frac{RV_{EXP}}{(\sigma^2 + N_{otr})}, \tag{2.36}$$

$$SNR_{CHI} = \frac{RV_{CHI}}{(\sigma^2 + N_{otr})}, \tag{2.37}$$

where the mean and the variance of the above SNR will be as follows,

$$\mu_{EXP} = \frac{\overline{RV_{EXP}}}{(\sigma^2 + N_{otr})}, \sigma_{EXP}^2 = \frac{VAR(RV_{EXP})}{(\sigma^2 + N_{otr})^2} \tag{2.38}$$

$$\mu_{CHI} = \frac{\overline{RV_{CHI}}}{(\sigma^2 + N_{otr})}, \sigma_{CHI}^2 = \frac{VAR(RV_{CHI})}{(\sigma^2 + N_{otr})^2} \tag{2.39}$$

Table 2.3 Depth, Transmission Distance, Transmitter and Receiver Depth for Shallow Long, Medium, and Short Range Channels

Depth (m)	Distance (m)	Transmitter Depth (m)	Receiver Depth (m)	Channel Type	Frequency (kHz)
1000	10000	995	995	Long, Close to bottom	1
		5	5	Long, Close to surface	1
		5	995	Long, In between	1
100	1000	95	95	Medium, Close to bottom	10
		5	4	Medium, Close to surface	10
		5	95	Medium, In between	10
9	90	8.5	8.5	Short, Close to bottom	100
		1	1	Short, Close to surface	100
		1	8.5	Short, In between	100

Using the values of exponential mean and variance and non-central chi-square mean and variance, equations (2.38) and (2.39) become,

$$\mu_{EXP} = \frac{\lambda^{-1}}{(\sigma^2 + N_{otr})}, \sigma^2_{EXP} = \frac{\lambda^{-2}}{(\sigma^2 + N_{otr})^2} \tag{2.40}$$

$$\mu_{CHI} = \frac{(K' + \lambda)}{(\sigma^2 + N_{otr})}, \sigma^2_{CHI} = \frac{2(K' + 2\lambda)}{(\sigma^2 + N_{otr})^2}, \tag{2.41}$$

where $K' > 0$ represents the degrees of freedom, and $\lambda > 0$ represents the rate in the first equation and non-centrality parameter in the second equation.

2.5   Benefits of Channel Classification and Selection of Channels

In this section, first, the benefits of channel classification will be provided briefly and second, selection of channels will be discussed. It is beneficial to classify the UAC channels according to their environments. Once the UAC environments are determined, the appropriate channel representation can be used. In shallow channel environments, *close to surface channel* may have line of sight path (if both the transmitter and receiver are in sight of each other) arriving first, followed by one time surface reflected path, then one time bottom reflected path, followed by bottom-surface one time reflected path, surface-bottom one time reflected paths, followed by other multiple reflected paths. In *close to bottom channel*, the paths will be in the order of LOS, bottom reflected, surface reflected, bottom-surface one time reflected path, surface-bottom reflected path followed by other multiple reflected paths. In *in-between* channels, if the difference $|z_s - z_r|$ is small the order of the paths will be LOS, surface, bottom, surface-bottom one time reflected, bottom-surface one time reflected path followed by multiple reflected paths. If the difference $|z_s - z_r|$ is large, the paths will be LOS, surface, bottom, bottom-surface, surface-bottom followed by rest of the multiple reflected paths. Once the channel environment and hence the path origins are identified, it may be easier to retrieve the signal information. For example, a surface only reflected path will be affected by surface wave and other surface agitations. Knowledge of path origin will allow applying noise cancellation and small scale fading compensation techniques suited for surface boundary agitation.

The UAC channels can be affected by geographical location of communication (longitude/latitude), transmitter and receiver distances from the surface and the bottom boundaries; water column height; transmission range; frequency; sound velocity, the water environment etc. Channel parameters unique to each UAC environment is used to differentiate each environment and its corresponding channel equations. For example, the longitude/latitude of location, time of year or season, wind velocity will determine the roughness of the sea surface. Knowing these parameters in addition to the transceiver depth from surface will determine if the channel is close to rough or smooth surface. Once rough surface is identified, scatters due to rough surface may be taken into account, and the channel equations corresponding to close to rough surface environment may be utilized.

The Cognitive Intelligence (CI) can sense channel environment parameters and map them to accurate UAC channel environment according to parameter values [4]. Once the UAC channel environment is determined, the UAC channel environment can be mapped [5] onto any one of the appropriate channel representations that were presented in the previous sections.

In an event, when the channel database does not contain an exact match of a UAC environment, CI can choose a channel representation that fits closest to the UAC environment. This may happen when a significant number of channel parameters and/or parameter values defining the specific UAC environment differ from a known UAC environment in the database. For example, the depth value in a new UAC environment may be larger than the depth threshold for close to surface environment in the database, the temperature and the location in the world may indicate the new environment to be in between the surface and the bottom. But the type of ocean traffic and the type of marine life concentration may indicate the new UAC environment to be a close to surface channel environment. In such a case, depending on the deviation of parameter values of the new UAC environment from the thresholds of parameter values of a known UAC environment in the channel database, the in between surface and bottom environment may be selected. Correspondingly, the channel representation for in between surface and bottom can be chosen for communication.

2.6 Simulation Results of UAC Channels

The simulation is carried out using the parameters in Table 2.3, MATLAB, and the Bellhop model [16] used and provided by the AcTUP software module [17]. The range to depth ratio can define an underwater channel to be shallow or deep. A range to depth ratio of 10:1 may define a channel as shallow [18] and the transmission can be considered horizontal. The range of transmission can define a channel to be short, medium, or long. A long range channel over several tens of kilometers is limited to a few kHz; a medium-range channel over several kilometers has a bandwidth in the order of tens of kHz, while a short range channel over several tens of meters may have hundreds of kHz [2] available.

First, the simulation results of the channel impulse response are presented. Second, the results of the fading characteristics of various channels are presented.

2.6.1 Channel Impulse Response in Different UAC Environments

- Shallow Channel (Constant Sound Velocity), Smooth Surface and Bottom: In a shallow *in between surface and bottom* channel environment, when the boundaries are smooth, the CIR will contain paths from surface only reflection, multiple surface bottom reflections, bottom only reflection, multiple bottom surface reflections, and paths due to other reflections/refractions/scatters from in between objects as in (2.10). The CIR of in between channels in Fig. 2.8, 2.11, and 2.14 contain all these groups of paths. Fig. 2.6, 2.9, and 2.12 illustrate *close to smooth surface* channels. If the paths reflected from the bottom are weak, they can be neglected. Fig. 2.7, 2.10, and 2.13 illustrate *close to smooth bottom channels*. If the paths reflected on the surface are weak, they can be neglected. In close to surface smooth channels, the values of source depth, z_s and receiver depth, z_r will be smaller compared to water column height, H or transmission range, D. When both H and D are small, in case of short range, the paths LOS, surface only, bottom only, bottom-surface, surface-bottom, paths will be more distinctly apart from each other. If D is high as in long range channels, the above paths will arrive close to each other and will be less distinct. For short and medium range, if H is higher, multiple boundary reflected paths will be grouped together and will almost overlap. For example, paths resulting from $2H$ will be grouped together, $3H$ will be grouped together (using (2.4)). Equations, (2.4) and (2.6) are used to generate delay and transmission loss amplitudes of Fig. 2.15, where a) Depth 9m, distance 90m, transmitter depth 1m, receiver depth 1m, frequency 100kHz (b) Depth 100m, distance 1000m, transmitter depth 5m, receiver depth 4m, frequency 10kHz, and (c) Depth 1000m, distance 10000m, transmitter depth 5m, receiver depth 5m, frequency 1kHz. In this figure, only the LOS, surface only, bottom only, bottom-surface, and surface-bottom paths are displayed. For short range channel (a), D is small and H is small, hence the LOS and surface only paths are distinct. For medium (b) and long (c) range channels, both D and H are high and these two paths almost overlap each

other. Paths interacting with the bottom boundary arrive later but these paths are close to the LOS and surface only reflected paths in terms of loss and delay and hence cannot be neglected. If z_s and z_r are small enough and H and D are large enough, the paths interacting with the bottom will have larger delay and loss and hence can be neglected as seen in equations (2.13). In a *short range, shallow, close to smooth surface channels*, as in Fig. 2.6, the paths are more spread out at each delay i.e. at each delay, neighboring paths arrive without overlapping. In Fig. 2.8, *short range, in between surface and bottom channel*, the paths are less spread out compared to close to surface case. In a *close to bottom channel*, as in Fig. 2.7, the paths are least spread out among the three short range channels. Compared to the *short range* channels, *the medium range* channel paths are much less spread out and are almost overlapping, and are arriving as an overlapped bundle at each delay. This can be observed in Fig. 2.9 through Fig. 2.11. In long range channels, the neighboring paths completely overlap each other. As a result, at each delay, there is only one path instead of spreading of paths. Fig. 2.12 through Fig. 2.14 illustrate this. In the shallow channel environments presented above, the paths in different groups arrive very close to each other. Because of this reason, the paths in different groups are not separately shown in the figures.

- Shallow Channel (Constant Sound Velocity), Rough Surface and Bottom: If the bottom or the surface varies in shallow channels, the power delay profile varies drastically, where only a few paths arrive at the receiver at different delays and at different power levels. For a varying surface, the number of paths, their amplitudes, and delays in Fig. 2.6, 2.9, and 2.12 will vary. This variation will be more prominent in short and medium range channels. For a varying bottom, the number of paths, their amplitudes, and delays in Fig. 2.7, 2.10, and 2.13 will vary. This variation will be more prominent in short and medium range channels.

- Deep Channel Simulation (Varying Sound Velocity Profile): Sound velocity will vary in a deep channel. Considering a variable sound velocity profile simulation can be carried out in SOFAR and other deep channels. Simulation results will be similar to that of the shallow channel figures as presented above. Because of high depth and long range that characterize

the deep channels, there will be high loss associated with each path arriving at very long delays.

2.6.2 Fading Characteristics of WSS Uncorrelated Tap Channel

In Fig. 2.16, the power (power calculated in terms of path loss) ratios of direct path to other paths, in various ranges, in shallow water close to bottom channels are illustrated. The power values are taken from Fig. 2.7, 2.10, and 2.13. All the arrived paths are considered. In medium and long range channels, the ratio is greater than 1 at all three distances, indicating Rician or Gaussian fading. At 6000 meter in long range and at 600 m in medium range, it is Gaussian fading. At 3000m in long range and at 200m in medium range, it is also Gaussian fading. At longer distances, the direct path loses power significantly and becomes comparable to the less dominant paths. Hence at 1000m in medium and at 10000m in long range channels, it becomes Rician fading. In short range channels, the indirect paths have significant power and hence results in mostly Rayleigh fading at all three distances.

2.7 Measurement Results

This section presents the setup and results of underwater acoustic communication channel measurement carried out at University of South Florida, St. Petersburg, FL campus.

2.7.1 Measurement Setup

The measurement is conducted in an indoor tank in Marine Science laboratory, University of South Florida, St. Petersburg, FL. The tank inner dimension is of length 2.38m, width 1.16m, and water surface to bottom depth of 0.88m. The tank is made up of nylon material. The tank water temperature and salinity measured is 68.9°F and 30.80 respectively. Two RESON transducers are used to transmit and receive the signal while a signal generator generates the transmitted signal and an oscilloscope is used to record the transmitted and received signals. The transducers are 18 degrees conical directional transducers with operating resonant frequency of 200 KHz, operating bandwidth of 40 KHz, and with maximum power level of 50 Watt or 47 dB. The voltage and frequency range of the signal generator is 32V peak to peak and 50MHz respectively. The range of

the oscilloscope is 100V per division with probe on the Y axis and $100\mu sec$ per division on the X axis. Figures 2.17, 2.18, 2.19, 2.20, and 2.21 illustrate the tank, the transducers, salinity instrument, signal generator, and oscilloscope. The transducer transmits signal at 200kHz with peak to peak voltage of 20V. Fig. 2.22 (a) presents the measurement configuration by varying the depth of the transducers between the water surface and bottom. In this figure one transducer position is shown, the other transducer will have identical position variation on the opposite side. Both transducers are placed at the mid length position of the longer side of the tank wall. The transducers are 1.16m from each other. Position A denotes the placement of the transducers 1 inch from water surface, facing each other, and adjacent to the tank walls along the length of the tank. Position B denotes the placement of the transducers mid point between surface and bottom of the tank, facing each other, and adjacent to the tank wall along the length of the tank. Position C denotes the placement of the transducers 1 inch from the bottom of the tank, facing each other, and adjacent to the tank wall along the length of the tank.

Fig. 2.22 (b) presents the measurement configuration by varying the range of the transducers along the longer side of the tank walls. In this figure one transducer position is shown, the other transducer will have identical position variation on the opposite side. Position F denotes the placement of the transducers at the mid point between surface and bottom, facing each other, and adjacent to the tank walls along the shorter length of the tank, 2.38m from each other. Position G denotes the placement of the transducers at the mid point between surface and bottom, facing each other, and 1.19m from each other and 0.595m away from the shorter wall of the tank. Position H denotes the placement of the transducers at the mid point between surface and bottom, facing each other, and 0.595m from each other and 0.8925m away from the shorter wall of the tank.

2.7.2   Measured Results

Figures 2.23, 2.24, 2.25, 2.26, 2.27, and 2.28 illustrate the transmitted and received signal snapshots from the oscilloscope at corresponding positions of the transducers in Fig. 2.22 under smooth surface and bottom conditions. The input or transmitted channel on the oscilloscope is calibrated with 10V per division on the Y axis and the output or received channel is calibrated

with 20mV per division on the Y axis. The channel analysis in section 2.3 is based on the fact that the UAC channel is bounded by 2 boundaries, namely the surface and the bottom. However, the UAC channel in the tank measurement is bounded by 6 boundaries, 4 tank walls in addition to surface and bottom boundaries. This difference in the channels may contribute to differences in the CIR between analysis and measured results.

Fig. 2.29 presents the CIR of the transmitted signal, which is a single pulse with a peak to peak voltage of 20V. The noise in the system contributes to an amplitude of less than .01V. Fig. 2.30, 2.31, and 2.32 present the CIR of the received signal at position A, B, and C respectively. When the communication channel is close to either of the two boundaries (positions A and C), the received signal strength is higher compared to the signal from in between surface and bottom channel (position B). For close to surface and close to bottom channels, the reflected and/or scattered paths from the surface and bottom respectively propagate shorter paths that contribute to stronger arrived paths. In addition for these two types of channels, reflected and/or scattered paths from the *opposite boundaries* travel longer paths losing strength when arrived at the receiver. Therefore, there is a significant difference in earlier and latter paths in the CIR of these two types of channels. Between positions A and C, when the channel is close to the bottom boundary, the received signal is subjected to diffraction and absorption by the bottom surface of the tank resulting in lower received signal strength compared to close to surface scenario. For the in between surface and bottom channel, paths reflected/scattered on both boundaries travel longer paths compared to channels in positions A or C resulting in lower similar amplitude signal strength in most of the arrived paths. It may be noted that because of the transducer positions adjacent to the walls, some paths are absorbed, diffracted by the tank walls.

Fig. 2.33, 2.34, and 2.35 present the CIR of the received signal at position F, G, and H respectively. In the longest range, position F, the signal is indistinguishable from the surrounding noise. In position G, medium range, the received signal strength is still at the noise level. However, in position H, short range, the signal strength is high and the CIR is clearly distinguishable. Since compared to all other positions, at H, the transducers are closest to each other in range, the paths arrive earlier compared to other scenarios. Additionally even though it is a short range in between
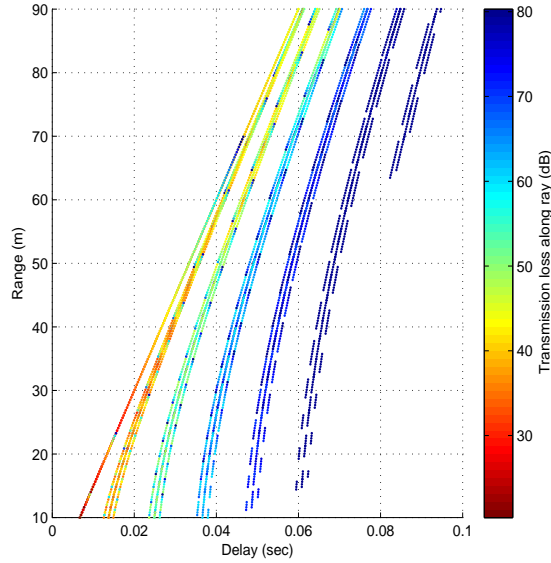
42

Figure 2.6 Transmission Loss/amplitude at Various Delays and Ranges, Short, Close to Surface, Shallow Smooth Surface and Bottom, Depth 9m, Distance 90m, Frequency 100kHz

surface and bottom channel, the paths are stronger compared to position B. This is due to the fact that the short range makes the surface and/or bottom reflected/scattered paths to travel shorter distance.

2.8   Conclusion and Future Research of UAC Channel Representation

Once the UAC environments are determined from the channel parameters, the channel representations can be derived according to the environments. In this chapter, a high level classification of the UAC channel environments are presented and channel representations are proposed, which are derived according to the classified UAC environments. The channel analysis is shown in terms of channel impulse response equations and fading characteristics of the received signals. As part of future research, classification and channel representation of non-WSS channels and correlated taps can be considered.
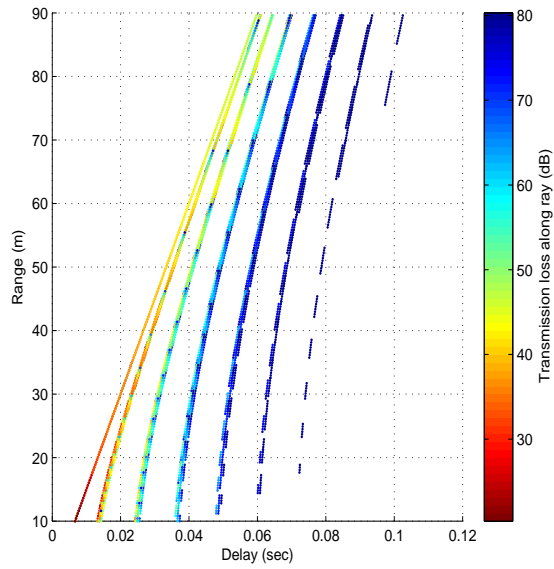
Figure 2.7 Transmission Loss/amplitude at Various Delays and Ranges, Short, Close to Bottom, Shallow Smooth Surface and Bottom, Depth 9m, Distance 90m, Frequency 100kHz
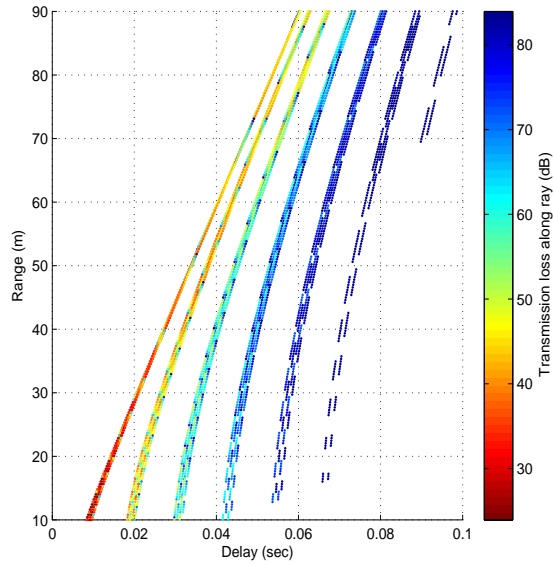

Figure 2.8 Transmission Loss/amplitude at Various Delays and Ranges, Short, Between Surface and Bottom, Shallow Smooth Surface and Bottom, Depth 9m, Distance 90m, Frequency 100kHz
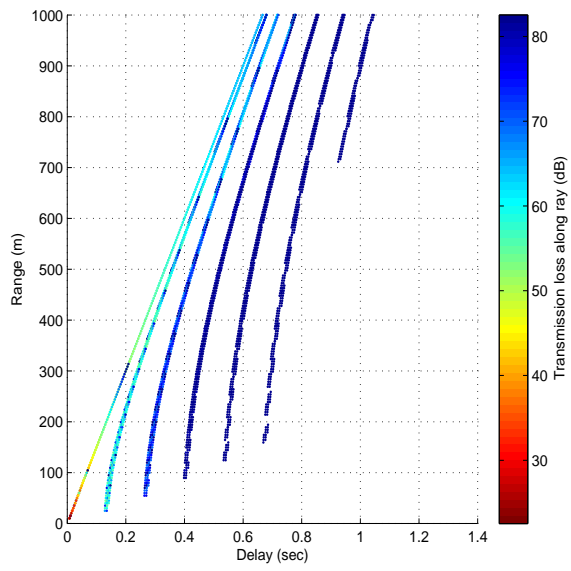
Figure 2.9 Transmission Loss/amplitude at Various Delays and Ranges, Medium, Close to Surface, Shallow Smooth Surface and Bottom, Depth 100m, Distance 1000m, Frequency 10kHz
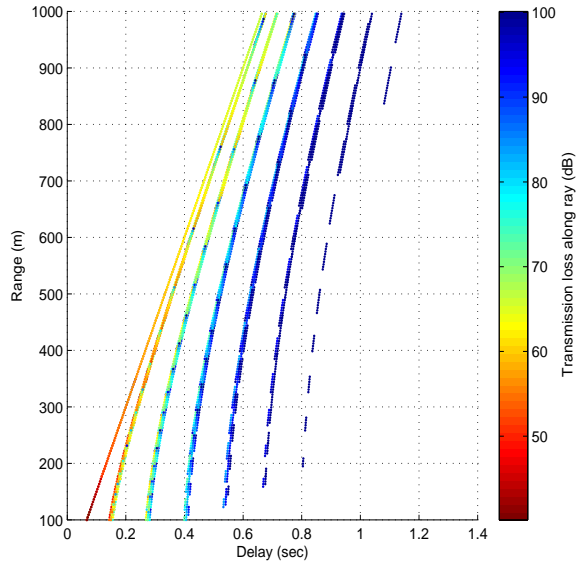

Figure 2.10 Transmission Loss/amplitude at Various Delays and Ranges, Medium, Close to Bottom, Shallow Smooth Surface and Bottom, Depth 100m, Distance 1000m, Frequency 10kHz
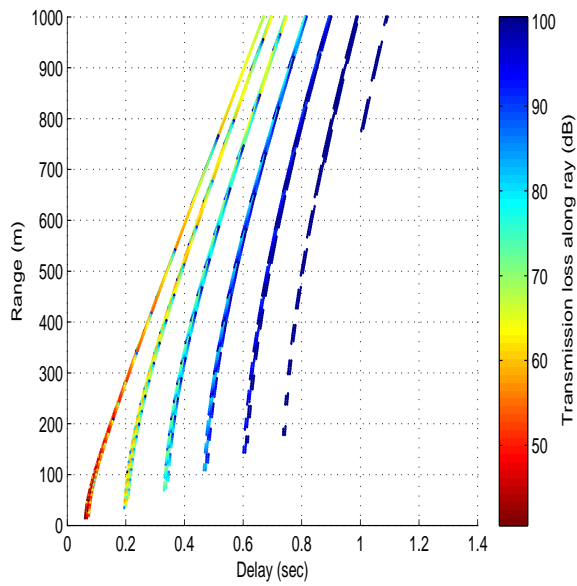
Figure 2.11 Transmission Loss/amplitude at Various Delays and Ranges, Medium, Between Surface and Bottom, Shallow Smooth Surface and Bottom, Depth 100m, Distance 1000m, Frequency 10kHz
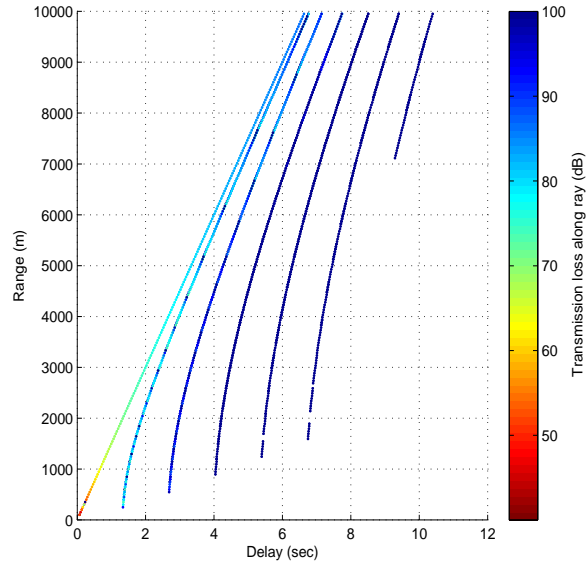

Figure 2.12 Transmission Loss/amplitude at Various Delays and Ranges, Long, Close to Surface, Shallow Smooth Surface and Bottom, Depth 1000m, Distance 10000m, Frequency 1kHz
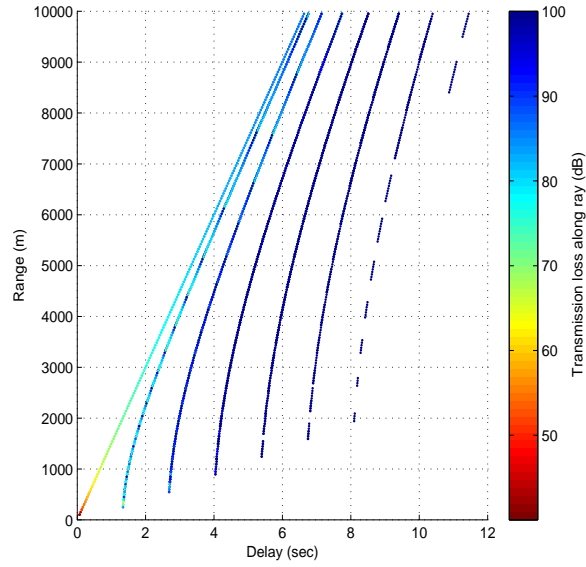
Figure 2.13 Transmission Loss/amplitude at Various Delays and Ranges, Long, Close to Bottom, Shallow Smooth Surface and Bottom, Depth 1000m, Distance 10000m, Frequency 1kHz
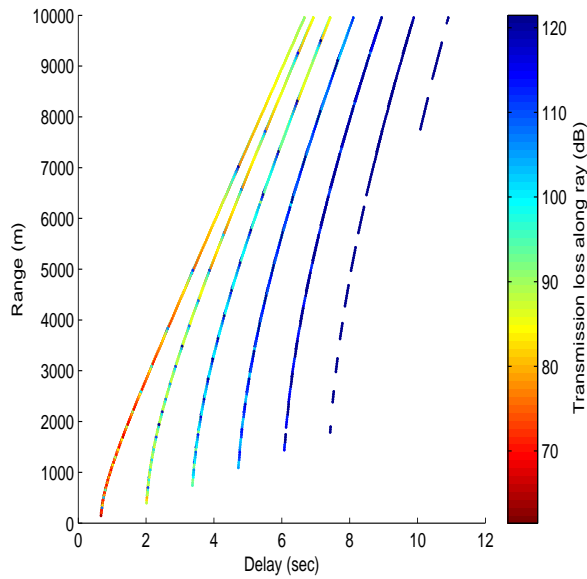

Figure 2.14 Transmission Loss/amplitude at Various Delays and Ranges, Long, Between Surface and Bottom, Shallow Smooth Surface and Bottom, Depth 1000m, Distance 10000m, Frequency 1kHz

47
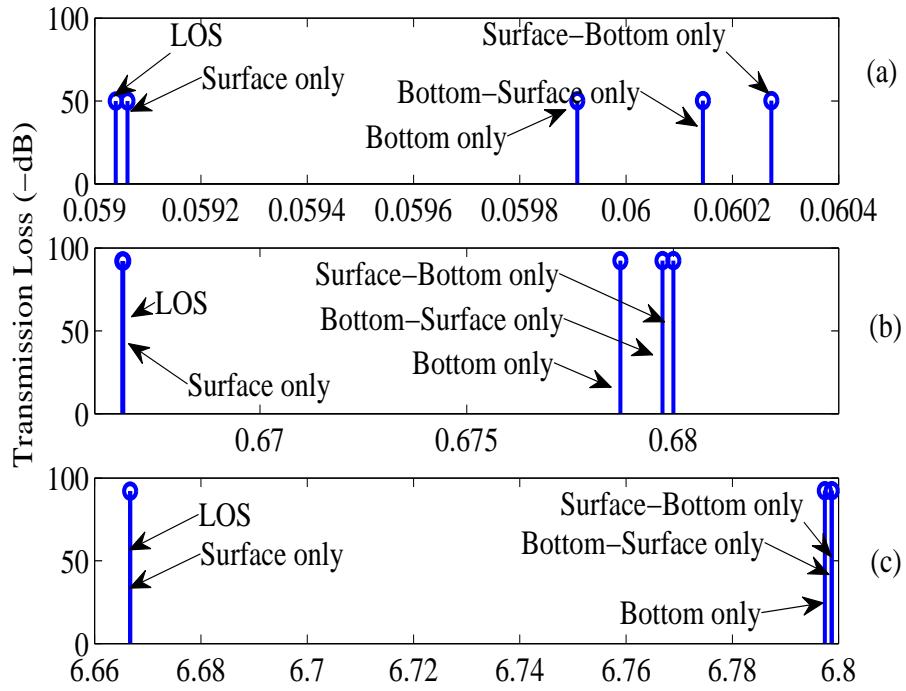
Figure 2.15 Transmission Loss at Various Delay, Smooth Surface and Bottom Shallow Channel, Close to Smooth Surface
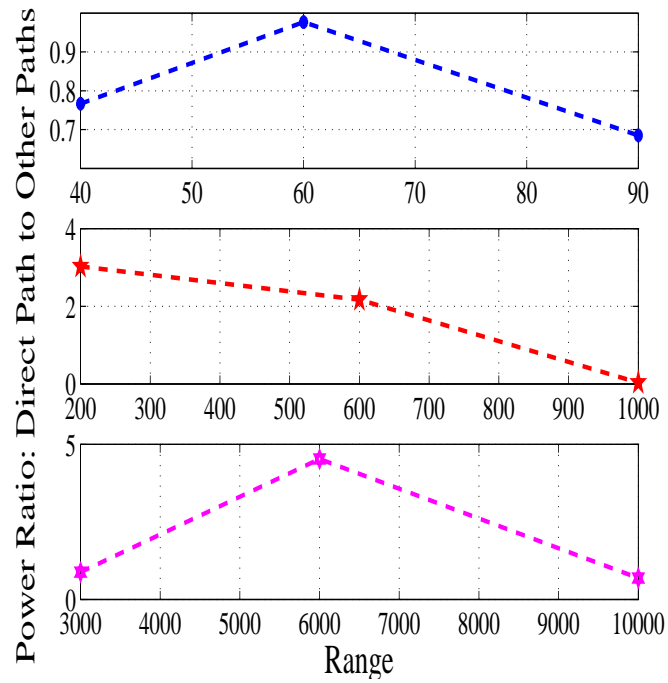
Figure 2.16   Top, Short, Close to Bottom Shallow, Middle, Medium, Close to Bottom Shallow, Bottom Long Close to Bottom Shallow

Figure 2.17   Measurement Tank

Figure 2.18 Transducers
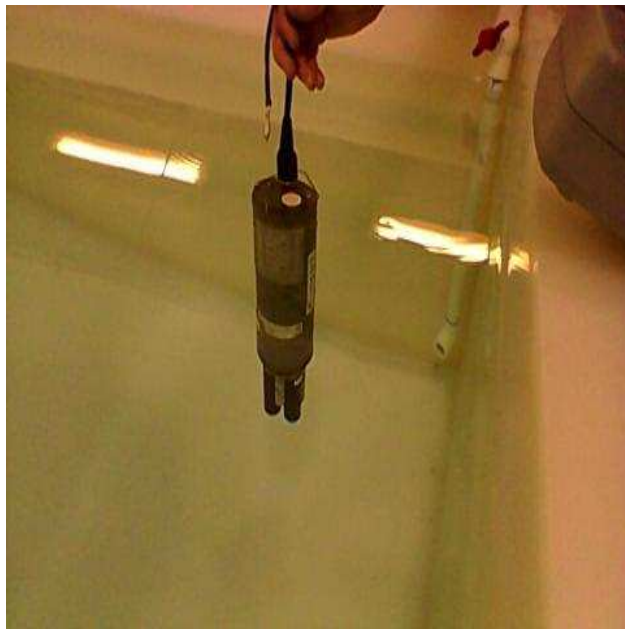
Figure 2.19 Salinity Measuring Instrument

Figure 2.20 Signal Generator

Figure 2.21 Oscilloscope
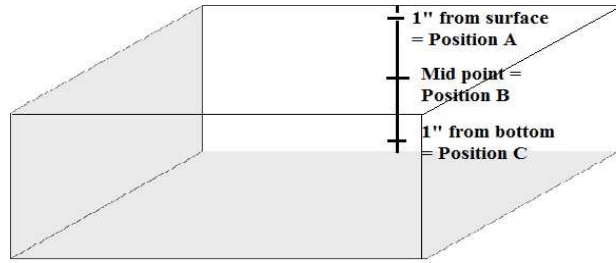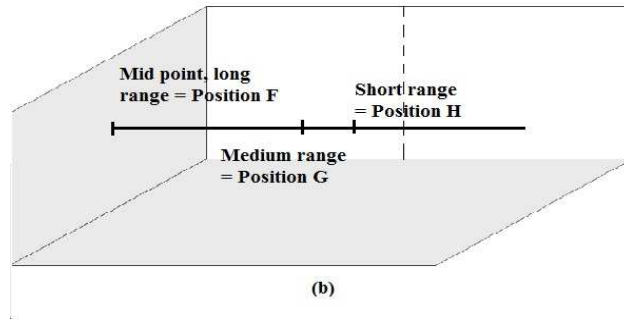
Figure 2.22 Tank Measurement Configuration

Figure 2.23 In Tank, Position A, Close to Surface

Figure 2.24 In Tank, Position B, In between Surface and Bottom

Figure 2.25 In Tank, Position C, Close to Bottom

Figure 2.26 In Tank, Position F, Long Distance, In between Surface and Bottom
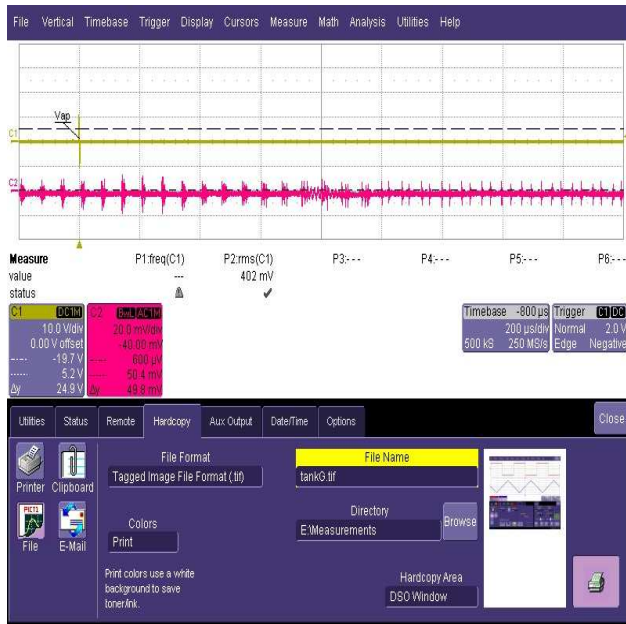
Figure 2.27 In Tank, Position G, Medium Distance, In between Surface and Bottom

Figure 2.28 In Tank, Position H, Short Distance, In between Surface and Bottom
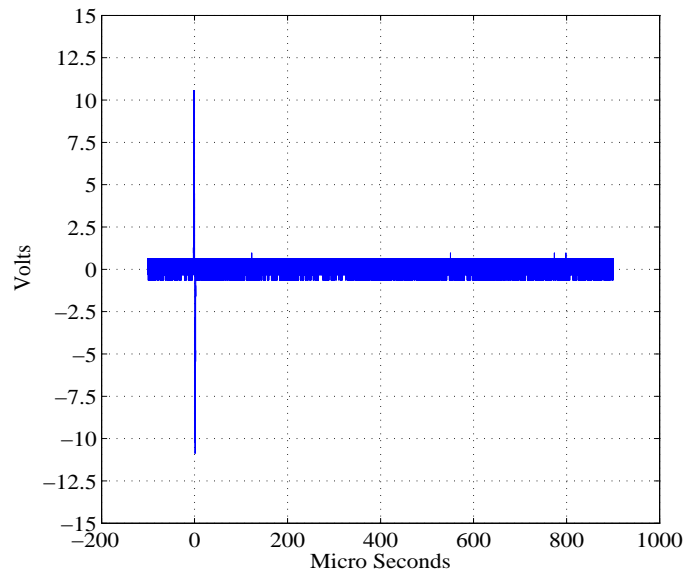
Figure 2.29 In Tank, CIR of Source Signal
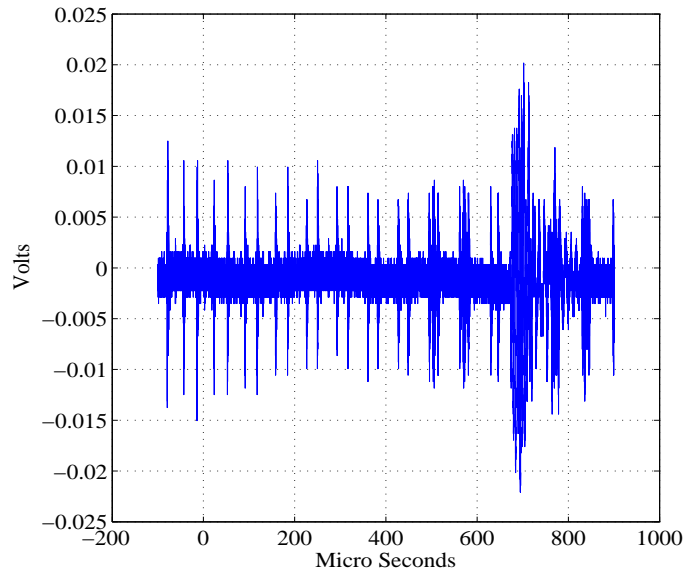
Figure 2.30 In Tank, Position A, Received Signal CIR
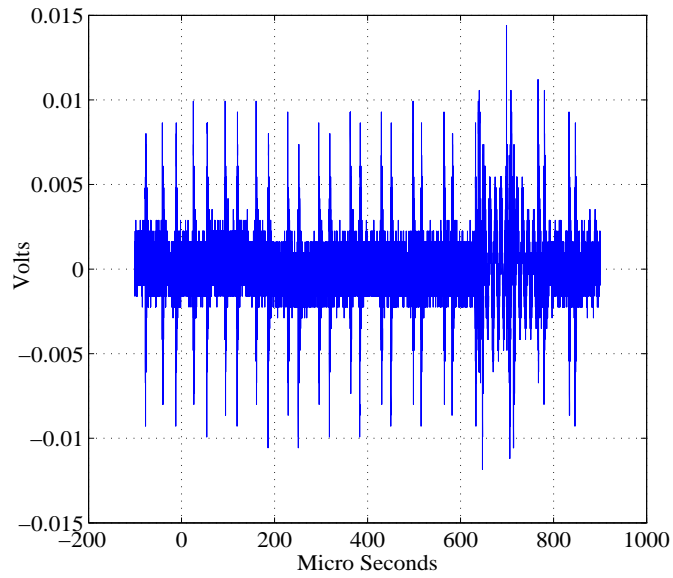
Figure 2.31 In Tank, Position B, Received Signal CIR

56
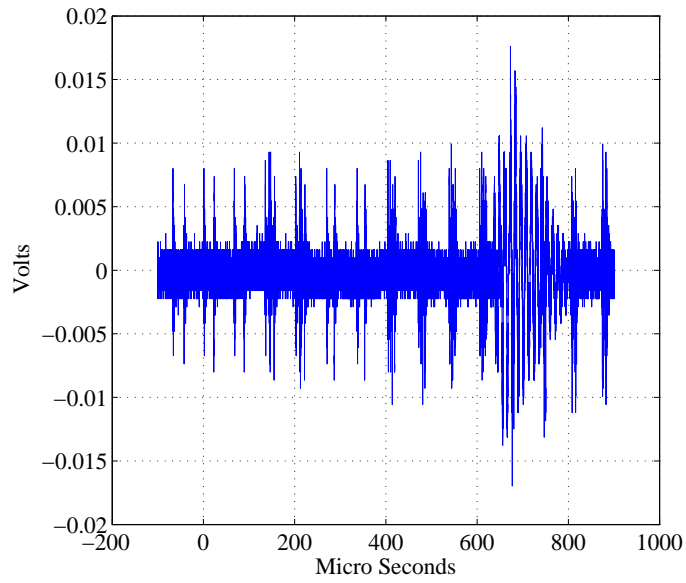
Figure 2.32 In Tank, Position C, Received Signal CIR
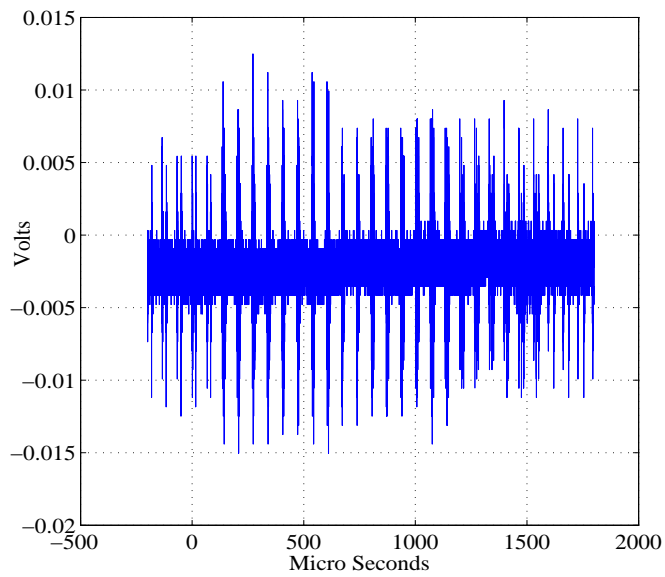
Figure 2.33 In Tank, Position F, Received Signal CIR
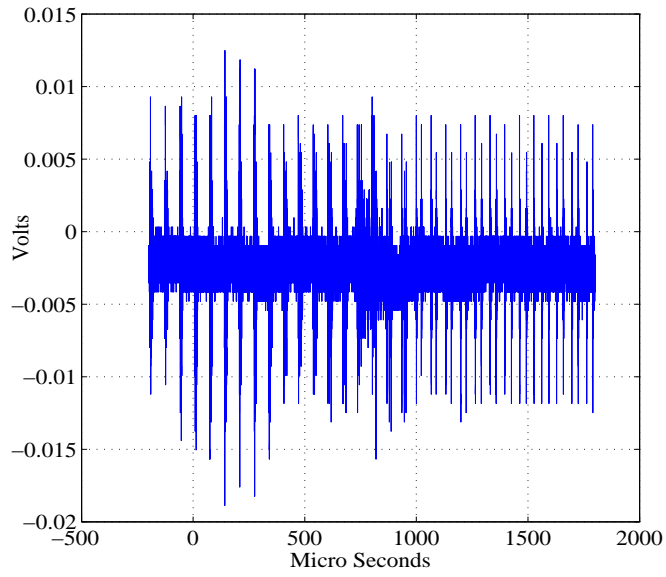
Figure 2.34 In Tank, Position G, Received Signal CIR
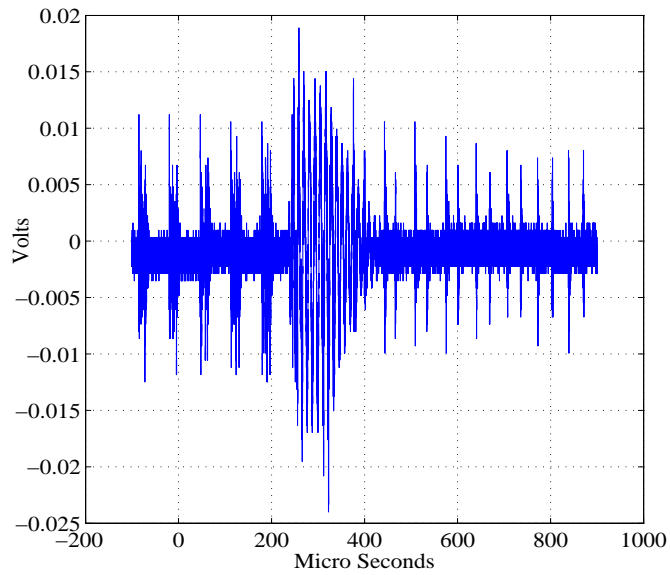
Figure 2.35 In Tank, Position H, Received Signal CIR

58

CHAPTER 3 :

ESTIMATION AND COMPENSATION OF DOPPLER SHIFT IN UAC OFDM SYSTEMS

Doppler effect [1] causes loss of orthogonality in Orthogonal Frequency Division Multiplexing (OFDM), which in turn may severely degrade receiver performance. In high data rate underwater acoustic communication (UAC), the effect of Doppler shift varies considerably over OFDM frequency band. In the past and current UAC OFDM literature [19]- [24], the frequency domain Doppler shift is presented in terms of path dependent Doppler scale in time domain. This chapter proposes and presents two algorithms to estimate Doppler scale induced by time variability of the channel. The performance of these estimation methods is evaluated under varying sampling period, varying number of channel taps, and varying channels.

3.1 Problem with Varying Doppler Shift in UAC OFDM Systems

In underwater acoustic communication (UAC) channel, Doppler causes significant degradation in transmission. According to the literature [2], [25], the two Doppler effects, shift and spread, are caused by two different sources. The *Doppler shift* is a function of the relative velocity of the transducers/hydrophones and other objects, variable acoustic velocity, and signal frequencies. The *Doppler spread* on the other hand, is primarily caused by the wind speed on the surface waves and by the internal currents. The total Doppler effect is a combination of Doppler shift and Doppler spread, where the average Doppler shift is much larger compared to overall Doppler spread [25].

In OFDM systems Doppler causes loss of orthogonality. This in turn may severely degrade receiver performance. In underwater OFDM, the bandpass frequency is comparable (for example, in Hz or kHz) to the baseband subcarrier frequencies (for example, in Hz or kHz). In such cases, the

---

[1]Part of the this chapter has been published in Proc. IEEE The Military Communicatins Conference,(MILCOM), San Diego, CA, USA, Nov 2008. Permission is included in Appendix C.
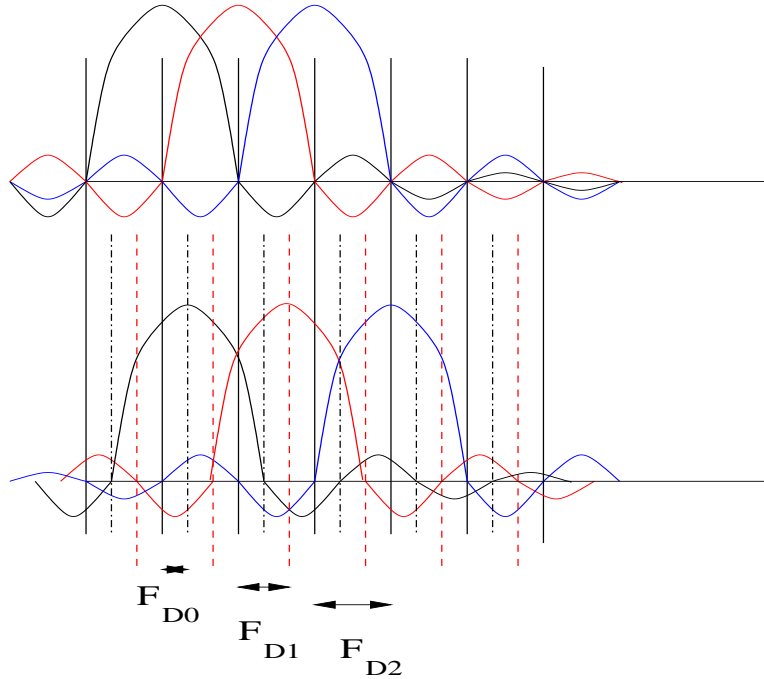
Figure 3.1 Varying Effect of Doppler Shift over OFDM Subcarriers

individual subcarrier frequency variation from the bandpass frequency is significant. Therefore, the effect of Doppler shift on OFDM signal will vary over subcarriers. The shift on the kth subcarrier due to the mth scatterer in baseband OFDM can be expressed as,

$$F_{Dkm} = \frac{v_w}{c_w} f_k cos\theta_m \ ,$$ (3.1)

where f_k is the kth subcarrier frequency, θ_m is the scattering angle of the mth scatterer, c_w is the sound speed in water, and v_w is the mobile velocity in water. Compared to the narrowband terrestrial RF, Doppler shift effect in UAC is more severe over OFDM subcarriers. This is primarily due to, A) Very low acoustic velocity compared to RF velocity, c_a i.e. $c_w << c_a$) giving rise to high Doppler shift effect, B) The comparable Doppler amount to the low values of subcarrier frequencies effect each subcarrier, and C) The variable Doppler shift effect over subcarriers due to low bandpass frequencies. Fig. 3.1 illustrates the varying effect of Doppler shift over OFDM subcarriers. In this chapter, two methods of time domain estimation of Doppler scale are proposed. The performance

of these estimation methods is evaluated under varying sampling period, varying number of channel taps, and varying channels. The contribution of this chapter are listed below.

- Two Doppler scale estimation methods are proposed to estimate the Doppler scale in time domain that causes Doppler shift over OFDM subcarriers in frequency domain. In both methods, at the transmitter, a known reference OFDM symbol is transmitted prior to transmiting data OFDM symbols. At the receiver, the received reference symbol, which is convolved with the channel, is cross-correlated at different delays, with the local known symbol, provided by the receiver that has not been convolved with the channel. The correlation operation determines the channel tap positions. In the first method, channel tap positions in the absence of Doppler are assumed *known*. The tap positions in the presence and in the absence of Doppler are compared to estimate the Doppler scale. In the second method, the channel tap positions in the absence of Doppler are *unknown* and a data OFDM symbol is auto-correlated at the receiver. The tap positions within the cross correlated reference and auto correlated data OFDM symbols are compared to determine the Doppler scale. Fig. 3.2 (a) illustrates the first method and Fig. 3.2 (b) illustrates the second method.

- Analysis of the two methods are derived. Simulation results are provided.

The rest of the chapter is organized as follows. In Section 3.2, a brief literature study is presented on Doppler effect in underwater acoustic OFDM. In Section 3.3, the proposed algorithms to estimate Doppler scale are presented. In Section 3.4, the analysis of Doppler effect is presented. In Section 3.5, the simulation results are provided for both the algorithms. In Section 3.6, the concluding remarks are presented.

3.2 Related Work on Doppler Shift in UAC OFDM

In [26], an iterative receiver is proposed to estimate Doppler and channel parameters and decode in an iterative manner where previous iteration values are used to compute future estimations. In [27], Doppler is treated as carrier frequency offset (CFO) and the CFO is estimated in an iterative manner. In this chapter, the proposed Doppler scale estimation methods do not treat
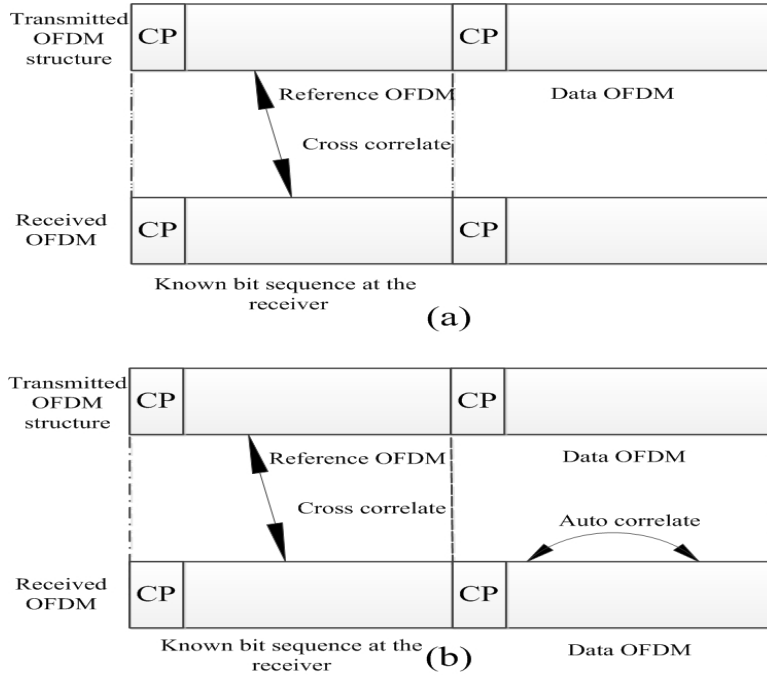
Figure 3.2 Signal Structure, Doppler Scale Estimation Methods

Doppler as CFO. Doppler scale results from time variability of the UAC channel and therefore, is not fixed over time. In the proposed methods, no previous estimated values are used in future estimations.

In [28], an adaptive frequency domain equalizer is utilized in coded OFDM. In [29], over-sampling is done in frequency domain to mitigate Doppler effect. In this chapter, the proposed estimation methods conduct the estimation, resampling, and compensation in time domain.

In [30], two ICI mitigation techniques are proposed. In the first method, ICI is explicitly estimated and in the second, instead of determining ICI values detection is done by adaptive decision feedback equalization. In [31], a factor graph based equalization method is utilized to mitigate both ICI and inter block interference (IBI). In this chapter, the proposed Doppler scale estimation and compensation are conducted in time domain. No ICI values or its components are determined.

In [32], adaptive detection method is proposed in MIMO OFDM signals to compensate non-uniform Doppler. In [33], a multiband OFDM is utilized to tackle Doppler. In this chapter, the Doppler scale estimation methods are proposed for single band OFDM systems.

In [20]- [23] a Doppler rate factor is determined to estimate Doppler and is compensated in the time domain. Similar to these publications, the two proposed Doppler estimation methods in this chapter estimate Doppler scale in time domain. However, in the prior publications, two extra identical OFDM symbols are transmitted prior to transmitting the data OFDM symbols. At the receiver, these two transmitted symbols are correlated to determine the Doppler scale. In other cases, a preamble and a postamble are transmitted with the OFDM block. By comparing the length of the received OFDM block with the expected length, the Doppler scale is determined. In this chapter, in the proposed Doppler scale estimation methods, one reference OFDM symbol is transmitted prior to data OFDM block. This reference OFDM is used with a local known symbol at the receiver to estimate Doppler scale in the first method. In the second proposed method, one data OFDM symbol is used in addition to estimate Doppler scale.

In [34], [35], the bounds of optimal resampling factor is determined when the Doppler scale varies over taps. In this chapter two Doppler scale estimation methods are proposed to estimate Doppler scale, when the scale is non-varying over taps and when it is varying. No optimal resampling factor is derived.

3.3   Proposed Estimation Techniques

The proposed Doppler scale estimation algorithms operate in time domain. Fig. 3.2 illustrates the signal structure for both algorithms. In both methods a known OFDM reference symbol is transmitted prior to transmitting the data symbols. This reference is cross correlated with the local known symbol at the receiver.

In the second proposed method, in addition to the reference cross-correlation, a data OFDM symbol is autocorrelated. In Fig. 3.3, the reference OFDM symbol is shown preceding the data OFDM block at the end of the IFFT operation.   Fig. 3.4 (a) illustrates the receiver architecture for the first algorithms and Fig. 3.4 (b) for the second. The rest of this section presents the two methods.
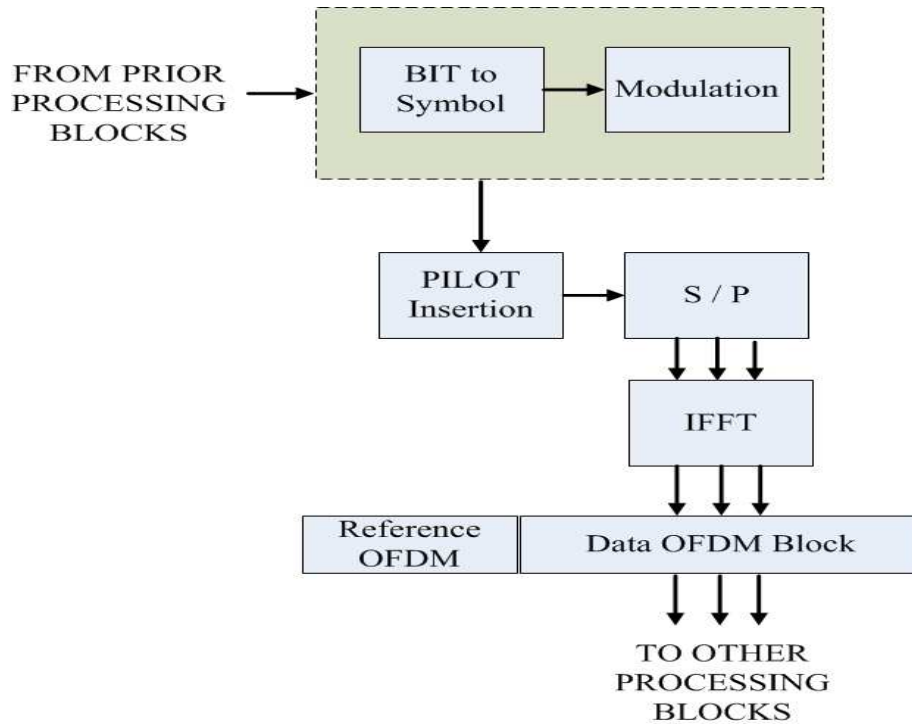
Figure 3.3 Transmitter Block Diagram

3.3.1 First Estimation Algorithm

The estimation algorithm is presented below.

- Cross correlate received reference symbol with the local known OFDM symbol.

- Determine the peak location/s.

- Compare each peak location with the corresponding known peak location. The difference determines the Doppler scale.

In the scenario, where the Doppler scale is assumed to be same on all taps, the scale is averaged over multiple peak differences. When the scale varies over taps, each peak will correspond to each path dependent Doppler scale.
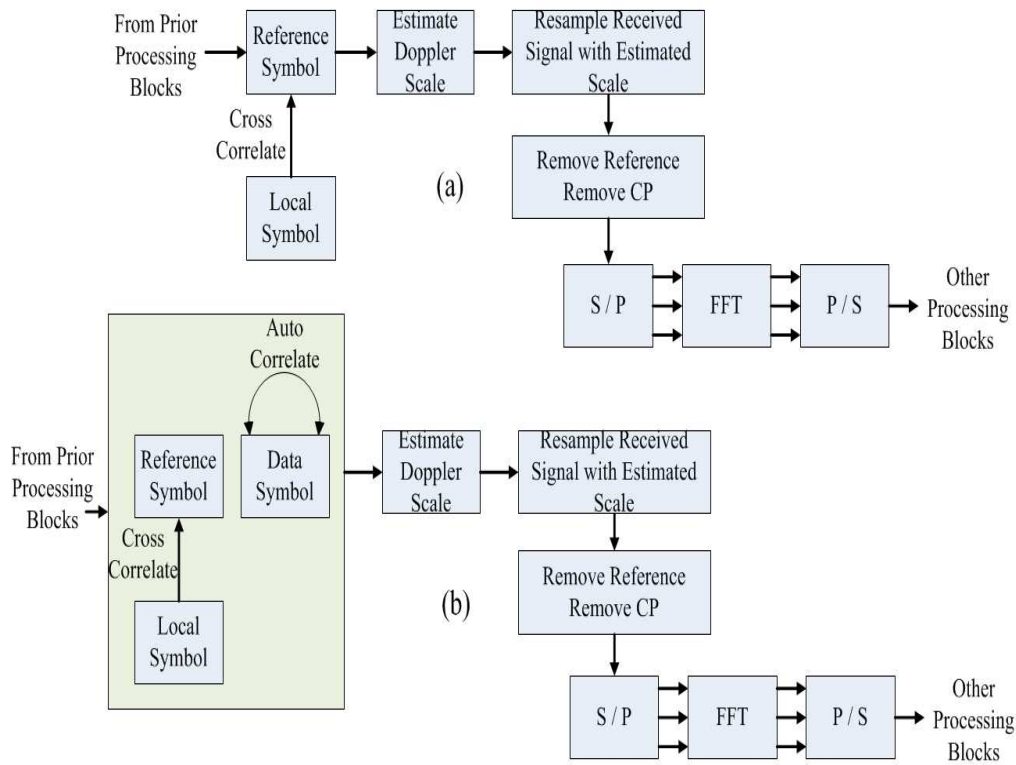
Figure 3.4 Receiver Block Diagram

3.3.2 Second Estimation Algorithm

In the second estimation method, in addition to the reference symbol, an OFDM data symbol is auto correlated. The algorithm is described below:

- Cross correlate received reference symbol with the local known OFDM symbol.

- Determine the peak location/s.

- Auto correlate the successive data OFDM symbol. Determing the peak location/s.

- Compare the peak location within the reference with the corresponding peak location within the data OFDM. The difference in peak location pairs determines the Doppler scale.

3.4 Analysis of Time Varying Channel in UAC OFDM Systems

A frequency selective and time varying channel can be expressed as [36],

$$h(t, \tau_{REF}) = \sum_{l=0}^{L-1} \alpha_l(t, \tau_{REF}) \delta(\tau_{REF} - \tau_l(t)), \tag{3.2}$$

where $\alpha_l(t, \tau)$ and $\tau_l(t)$ represent time varying attenuation coefficient and time varying tap delay of the lth delay bin respectively. Both parameters are function of time and depend on the scatterers arriving within the lth bin. The variable L represents the total number of multipaths or delay bins and δ represents the Dirac Delta function. In discrete domain (3.2) can be expressed as,

$$\begin{aligned}
h(n, nT_s) &= \sum_{l=0}^{L-1} \alpha_l(n, nTs) \delta(nT_s - \tau_l(n)) \\
&= \sum_{l=0}^{L-1} h_l(n), \\
&= h_0(n) + h_1(n) + h_2(n) + ..., \tag{3.3}
\end{aligned}$$

where variable T_s denotes the sampling period, nT_s represents the time corresponding to the nth sample. The channel impulse $h(n)$ is a complex quantity. It can be assumed that the real and imaginary components of $h(n)$ are independent and identically distributed (i.i.d.) and follow Gaussian distribution. Under such condition, the modulus of $h(n)$ or $|h(n)|$ will follow Rayleigh distribution [36]. Each scatterer causes a Doppler shift while M scatterers arriving at the same instance within the delay bin will cause Doppler spread.

The Doppler shift in frequency domain is caused by both time varying attenuation and time varying delay of each tap as seen in (3.3). In accordance to the literature in UAC, the time varying delay in time domain is considered to be the primary cause of Doppler shift in frequency domain. The time variability of each delay bin can be quantified with a scale factor known as Doppler scale.

In the rest of this section, first the general analysis is presented. Then individual analysis for each estimation method is presented. The following assumptions are made for simplicity of analysis,

- Each individual channel scatter within a channel tap, ideally, is associated with an attenuation, a delay, and a Doppler scale. It is reasonably assumed that all scatters within a channel tap have same delay, and Doppler scale, but different attenuation.

- It is reasonably assumed that channel tap attenuation, time invariant part of the delay, and Doppler scale parameter remain same over a block of OFDM symbols.

- The Doppler scale is first assumed to be same over all channel taps. This assumption is later removed.

- The tap attenuation is invariant over time, i.e. $\alpha_l(n) \approx \alpha_l$.

The time varying delay, $\tau_l(n)$ can be expressed as

$$
\begin{aligned}
\tau_l(n) &= \tau_l - an \\
\tau_l(n) &= lT_s - alT_s,
\end{aligned}
\tag{3.4}
$$

where a denotes the Doppler scale. In a frequency selective and fast fading channel, the kth channel frequency sample using (3.3) and (3.4) , can be expressed as,

$$
\begin{aligned}
H_k(n) &= \sum_{l=0}^{L-1} h_l(n) e^{-j2\pi f_k n} \\
&= \sum_{l=0}^{L-1} h_l e^{-j2\pi f_k \tau_l} e^{j2\pi f_k an}
\end{aligned}
\tag{3.5}
$$

The *OFDM signal structure* is represented as follows. After performing inverse fast Fourier transform (IFFT) on the frequency domain OFDM symbol, the nth discrete time sample of the transmitted OFDM symbol can be expressed as,

$$
X_n = \sum_{k=0}^{N-1} X_k e^{j2\pi \frac{nk}{N}} \quad 0 \le n \le N-1,
\tag{3.6}
$$

where N is the total number of FFT points. Replacing nk/N in (3.6),

$$
\begin{aligned}
X_n &= \sum_{k=0}^{N-1} X_k e^{j2\pi f_k(nT_s)} \quad 0 \le n \le N - 1, \\
&= \sum_{k=0}^{N-1} X_k e^{j2\pi f_k(n)} \quad 0 \le n \le N - 1,
\end{aligned}
\tag{3.7}
$$

where the real and imaginary components of the complex sample X_n are assumed to be i.i.d. Gaussian distributed [37]. If the channel is frequency selective, an additional cyclic prefix (CP) of length G will be added to each OFDM symbol such that, $G \ge M$. The sample of the transmitted OFDM symbol with CP can be expressed as (similar to [38]),

$$
X'_n = \begin{cases} X_n & 0 \le n \le N - 1 \\ X_{N+n} & -G \le n \le -1 \end{cases}
$$

After the removal of the cyclic prefix, the above equation deduces to (3.7).

The *received OFDM signal* is expressed as follows. In a frequency selective and a fast fading channel, the received OFDM symbol can be expressed as a discrete convolution between the transmitted symbol and the channel (similar to [38], [39]). Then the nth time sample Y_n of the recieved symbol is,

$$
\begin{aligned}
Y_n &= \sum_{l=0}^{L-1} h_l(n) X_{n-l} \quad 0 \le n \le N - 1, \\
&= h_0(n) X_n + h_1(n) X_{n-1} + h_2(n) X_{n-2}...
\end{aligned}
\tag{3.8}
$$

where the n in $h_l(n)$ denotes the time variation of the lth tap or bin. After performing fast Fourier transform (FFT) on the time domain received symbol, the frequency domain kth sample can be expressed as, $Y_k = \frac{1}{N} \sum_{n=0}^{N-1} Y_n e^{-j2\pi \frac{nk}{N}} = \frac{1}{N} \sum_{n=0}^{N-1} Y_n e^{-j2\pi f_k n}$. Using (3.8),

$$
Y_k = \frac{1}{N} \sum_{n=0}^{N-1} \Big[\sum_{l=0}^{L-1} h_l(n) X_{n-l} \Big] e^{-j2\pi f_k n}.
\tag{3.9}
$$

$$h_l(n) \;=\; \alpha_l \delta(nT_s - (\tau_l - an)), \tag{3.10}$$

When the Doppler scale varies over channel taps, i.e. each channel tap is associated with a different Doppler scale, eqn. (3.10) becomes

$$h_l(n) \;=\; \alpha_l \delta(nT_s - (\tau_l - a_l n)), \tag{3.11}$$

where a_l denotes the Doppler scale specific to lth tap delay. The received reference symbol, after convolving with the time varying channel, using (3.8) and (3.10) can be expressed as,

$$Y[n] = h_0 X_{n-an} + h_1 X_{n-1-an} + h_2 X_{n-2-an} + ..., \tag{3.12}$$

where X_{n-an} are known values at the receiver and the time variation of tap delays correspond to the convolution of channel taps with samples at time variant sample locations. When Doppler scale varies per channel taps, eqn. (3.12) becomes,

$$Y[n] = h_0 X_{n-a_0 n} + h_1 X_{n-1-a_1 n} + h_2 X_{n-2-a_2 n} + ..., \tag{3.13}$$

In the *First Estimation Method*, as presented in section 3.3, applying the Doppler scale estimation algorithm, the correlation operation at different lags between the received reference and the local known clean OFDM symbol, can be expressed as (using eqn. (3.12)),

$$
\begin{aligned}
RR_D[an] \;&=\; E[Y[n] * X[n - an]] \\
&= h_0 |X_{n(1-a)}|^2 + 0..., \\
&= PR_{D0} + 0... \\
RR_D[an - 1] \;&=\; E[Y[n] * X[n - an - 1]] \\
&= h_1 |X_{n(1-a)-1}|^2 + 0 \\
&= PR_{D1} + 0...,
\end{aligned}
\tag{3.14}
$$

Using eqn. (3.14), each tap value can be determined by,

$$|h_l| = \frac{PR_{Dl}}{|X_{n(1-a)-l}|^2},$$ (3.15)

Using eqn. (3.14), each tap location within the reference OFDM symbol in the presence of Doppler can be determined by,

$$[n_{R_{D1}}] = \arg\max RR_D[n]$$

$$[n_{R_{D2}}] = \arg\max RR_D[n], n \neq PRL_{D1},$$

$$[n_{R_{D3}}] = \arg\max RR_D[n], n \neq PRL_{D1}, n \neq PRL_{D2}, ...,$$ (3.16)

where each peak location, in terms of sample index, $PRL_{D1} = [n_{R_{D1}}]$, $PRL_{D2} = [n_{R_{D2}}]$, $PRL_{D3} = [n_{R_{D3}}]$ gives the time variant sample location after Doppler displacement of each tap. This location is compared with the known tap location in the absence of Doppler to estimate Doppler scale. Let the peak locations in the absense of Doppler be denoted as, PL_{ND1}, PL_{ND2}, PL_{ND3} etc. Then the Doppler scale a_r can be determined using eqn. (3.16) as follows,

$$\begin{aligned} \hat{a}_r &= \frac{PL_{ND1} - PRL_{D1}}{n_{ND1}}, \\ \hat{a}_r &= \frac{n_{ND1} - n_{ND1} + a_r n_{ND1}}{n_{ND1}}, \end{aligned}$$ (3.17)

where n_{NDi} denotes the sample location of the peak in the absence of Doppler. Averaging over all taps, using eqn. (3.17), the estimated Doppler scale becomes,

$$\hat{a}_r = \frac{1}{L} \sum_{i=0}^{L-1} \frac{a_{r_i} n_{NDi}}{n_{NDi}}$$ (3.18)

When Doppler scale is variable over taps, by considering multiple peaks for multiple taps and their corresponding sample locations, the tap/path dependent Doppler scales, a_{rl} can be estimated.

If the actual Doppler scale is denoted by a, then the difference between actual and estimated

scale can be determined by,

$$a - \hat{a}_r = a - \frac{1}{L}a_r \sum_{i=0}^{L-1} \frac{n_{NDi}}{n_{NDi}}$$
$$= a - \hat{a}_r \beta \tag{3.19}$$

Therefore, the estimated scale will be equal to the actual a if β in the second term in (3.19) is equal to 1. From (3.19), the following can be stated,

- the estimation accuracy is a function of number of taps. More number of taps can also imply the accuracy will be more prone to noise from each tap.

- Since the location of correlated peaks is used in estimation, the higher the values of taps, the more accurate will be the estimation.

- the estimation accuracy depends on the known code sequence used. In other words the reference symbol must possess strong autocorrelation property such that (3.14) yields a 0 at cross correlated positions. To express this (3.14) can be modified to have,

$$RR_D[an] = E[Y[n] * X[n - an]]$$
$$= P_{D0} + \epsilon...$$
$$RR_D[an - 1] = E[Y[n] * X[n - an - 1]]$$
$$= P_{D1} + \epsilon..., \tag{3.20}$$

then $\epsilon = 0$. The noise present in the received reference symbol will contribute to noise in the cross correlated peaks.

In the *Second Proposed Estimation Method*, a data OFDM is auto correlated in addition to the operations on the reference OFDM in the first method. The auto correlated peaks within the data

OFDM, PD_{Di}s can be expressed as,

$$RD_D[0] = E[Y[n] * Y[n]]$$

$$= h_0^2|X_{n(1-a)}|^2 + h_1^2|X_{n(1-a)-1}|^2 + h_2^2|X_{n(1-a)-2}|^2...,$$

$$RD_D[0] = PD_{D0} + PD_{D1} + PD_{D2} + ... \tag{3.21}$$

Using eqn. (3.21), each tap location within the data OFDM symbol in the presence of Doppler can be determined by,

$$[n_{D_{D1}}] = \arg\max RD_D[n]$$

$$[n_{D_{D2}}] = \arg\max RD_D[n], n \neq PDL_{D1},$$

$$[n_{D_{D3}}] = \arg\max RD_D[n], n \neq PDL_{D1}, n \neq PDL_{D2}, ..., \tag{3.22}$$

where each peak location, $PDL_{D1} = [n_{D_{D1}}]$, $PDL_{D2} = [n_{D_{D2}}]$, $PDL_{D3} = [n_{D_{D3}}]$ gives the time variant sample location after Doppler displacement of each tap within the data OFDM. This location is compared with the tap locations in the cross correlated reference OFDM found in equations, (3.16). Then the Doppler scale a_{RD} can be determined using eqn. (3.16) and (3.22) as follows,

$$PRL_{D0} - PDL_{D0} = n_{R_{D0}} - n_{D_{D0}}$$

$$= T_{OFDM} + \hat{a_{rD}}n_{ND0}$$

$$\hat{a_{rd}} = \frac{n_{R_{D0}} - n_{D_{D0}} - T_{OFDM}}{n_{ND0}}$$

$$\hat{a_{rd}} = \frac{(n_{R_{D0}} - n_{D_{D0}}) - N}{n_{ND0}} \tag{3.23}$$

Averaging over all taps, using eqn. (3.23), the estimated Doppler scale becomes,

$$\hat{a_{rd}} = \frac{1}{L} \sum_{i=0}^{L-1} \frac{(n_{R_{Di}} - n_{D_{Di}}) - N}{n_{NDi}} \tag{3.24}$$

The noise present in the received reference and data symbols will contribute to noise in the cross correlated peaks and auto correlated peaks respectively. When Doppler scale is variable over taps, by considering multiple peaks for multiple taps and their corresponding sample locations, the tap/path dependent Doppler scales, a_{rd_l} can be estimated.

If the actual Doppler scale is denoted by a, then the difference between actual and estimated scale can be determined by,

$$a - \hat{a_{rd}} = a - \frac{1}{L} \sum_{i=0}^{L-1} \frac{(n_{R_{Di}} - n_{D_{Di}}) - N}{n_{NDi}} \tag{3.25}$$

Therefore, the estimated scale will be equal to the actual a if the second term in (3.25) is equal to 0. The same three statements derived from (3.19) can be stated for (3.25) with the addition that the data sequence in the data OFDM may need to have good autocorrelation property as well.

In both of the proposed methods, in order to accurately estimate Doppler scale, the sampling period needs to be carefully chosen such that, either a_r or a_{rd} is a multiple of the sampling period,

$$\begin{aligned} a_r &= mT_s, \\ a_{rd} &= mT_s, \end{aligned} \tag{3.26}$$

where m denotes a fraction multiple.

The *ICI and SIR* can be expressed as follows. Using (3.6) in (3.9),

$$Y_k = \frac{1}{N} \sum_{n=0}^{N-1} \underbrace{\left[\sum_{l=0}^{L-1} h_l(n) \left(\sum_{k=0}^{N-1} X_k e^{j2\pi f_k(n-l)} \right) \right]}_{A_k} \cdot e^{-j2\pi f_k n}. \tag{3.27}$$

The A_k of (3.27) can be expanded using (3.5) and is expressed as below,

$$
\begin{aligned}
A_k &= \left[\sum_{l=0}^{L-1} h_l(n) \left(X_k e^{j2\pi f_k(n-l)} + \sum_{p=0,p\neq k}^{N-1} X_p e^{j2\pi(n-l)f_p} \right) \right] \\
&= \left[X_k \sum_{l=0}^{L-1} h_l(n) e^{j2\pi(n-l)f_k} + \sum_{p=0,p\neq k}^{N-1} X_p \sum_{l=0}^{L-1} h_l(n) e^{j2\pi(n-l)f_p} \right] \\
&= \left[\left(X_k \sum_{l=0}^{L-1} h_l(n).e^{-j2\pi f_k l} \cdot e^{j2\pi f_k n} \right) + \left(\sum_{p=0,p\neq k}^{N-1} X_p \sum_{l=0}^{L-1} h_l(n) e^{-j2\pi f_p l} \cdot e^{j2\pi f_p n} \right) \right] \\
&= \left[\left(e^{j2\pi f_k n} X_k \sum_{l=0}^{L-1} h_l(n) e^{-j2\pi f_k l} \right) + \left(\sum_{p=0,p\neq k}^{N-1} X_p \sum_{l=0}^{L-1} h_l(n) e^{-j2\pi f_p l} e^{j2\pi f_p n} \right) \right] \\
&= \left[e^{j2\pi f_k n} X_k H_k(n) + e^{j2\pi f_p n} \sum_{p=0,p\neq k}^{N-1} X_p H_p(n) \right] \quad (3.28)
\end{aligned}
$$

Using the value of A from (3.28) in(3.27) and after some simple computation, the received signal can be expressed as,

$$
\begin{aligned}
Y_k &= \underbrace{\frac{1}{N} \sum_{n=0}^{N-1} X_k H_k(n)}_{Desired} + \underbrace{\frac{1}{N} \sum_{n=0}^{N-1} \sum_{p=0,p\neq k}^{N-1} X_p H_p(n) e^{j2\pi n(f_k-f_p)}}_{ICI}, \\
&= \underbrace{\frac{1}{N} \sum_{n=0}^{N-1} X_k H_k(n)}_{Desired} + \underbrace{\frac{1}{N} \sum_{n=0}^{N-1} \sum_{p=0,p\neq k}^{N-1} X_p H_p(n) e^{j2\pi n\Delta f(p-k)}}_{ICI} \quad (3.29)
\end{aligned}
$$

where both the desired and the ICI are complex values incorporating time varying channel, where n denotes the time variability. The time variation of each tap is expressed as time variation of the delays in terms of Doppler scale. Using (3.5) in (3.29) the desired signal can be expressed as,

$$
D_{NC} = \frac{1}{N} \sum_{n=0}^{N-1} X_k \sum_{l=0}^{L-1} h_l e^{-j2\pi f_k l T_s(1+a)}, \quad (3.30)
$$

$$
D_C = \frac{1}{N} \sum_{n=0}^{N-1} X_k \sum_{l=0}^{L-1} h_l e^{-j2\pi f_k l T_s \frac{(1+a)}{(1+\hat{a})}}, \quad (3.31)
$$

Table 3.1 Doppler Shift Simulation Parameters

Parameters	Values
FFT Size	256
Carrier Frequency(kHz)	60
Bandwidth(kHz)	40
Number of taps	1,3
Channel(m)	100,50
Sampling rate (times)	10,50,1000
TxRx Speed(m/sec)	$[.01 : .1 : 3]$
Signal Velocity(m/sec)	1350
Realizations	10000
Channel	Actual

where D_{NC} and D_C denote the desired signal part without and with Doppler compensation respectively. The symbol, $\hat{a}$ is the general Doppler scale and can be estimated using either of the two proposed methods. Using (3.5) in (3.29) the ICI part can be expressed as,

$$ICI_{NC} \quad = \quad \frac{1}{N} \sum_{n=0}^{N-1} \sum_{p=0,p\neq k}^{N-1} X_p e^{j2\pi n \Delta f(p-k)} \sum_{l=0}^{L-1} h_l e^{-j2\pi f_k l T_s(1+a)}, \tag{3.32}$$

$$ICI_C = \sum_{n=0}^{N-1} \sum_{p=0,p\neq k}^{N-1} X_p e^{j2\pi n \Delta f(p-k)} \sum_{l=0}^{L-1} h_l e^{-j2\pi f_k l T_s \frac{(1+a)}{1+\hat{a}}}, \tag{3.33}$$

where ICI_{NC} and ICI_C denote the ICI components in the absense and in the presence of Doppler effect respectively.

When Doppler scale is estimated accurately, i.e. $\frac{(1+a)}{(1+\hat{a})} \approx 1$ in (3.31) and in (3.33), there will be no contribution of time varying effect into the desired signal part and into the ICI part respectively. Taking into account an additive white Gaussian noise (AWGN) term with zero mean and variance of σ_n, the signal to interference plus noise ratio (SINR) can be expressed as,

$$\begin{aligned} SINR_{ICI} \quad &= \quad \frac{Signal power}{ICI power + noise power} \\ &= \frac{E|Desired|^2}{E|ICI|^2 + \sigma_n}, \end{aligned} \tag{3.34}$$

3.5 Simulation Results

The simulation is carried out using the parameters in Table 3.1. The results are provided for realistic underwater acoustic channel responses provided in [40]. The simulation is carried out for various SNR values. The following two sub sections discuss the simulation results for the two estimation methods.

3.5.1 Simulation Using First Algorithm

Fig. 3.5 and 3.6 illustrates the coarse estimated Doppler scale in a 100m channel using the first 3 channel taps for 10 times and 50 times the original sampling rate respectively. The estimated Doppler scale values are more scattered with sampling rate of 10 compared to 50. The corresponding BER plots are given in Fig. 3.7 and in Fig. 3.8.

Fig. 3.9 and 3.10 illustrates the coarse estimated Doppler scale in a 100m channel using only the first channel tap for 10 times and 50 times the original sampling rate respectively. The estimated Doppler scale values are more scattered with sampling rate of 10 compared to 50. The corresponding BER plots are given in Fig. 3.11 and in Fig. 3.12.

Ideally, estimation with 3 taps should provide better accuracy. At the same time higher number of taps inject more noise in the estimation calculation. In the above figures it can be seen that compared to estimation with 3 taps, estimation with 1 tap gives less scattered values in both sampling rate situations.

During estimation and data sampling, when the rate is 10 or 50, the Doppler shifted samples are not hit because of low sampling rate and because of rounding the indexes during simulation. So, even though there is Doppler shift, the effect is not seen in the above BER plots, that is Doppler absence and presence act the same way.

Fig. 3.13 and 3.14 illustrates the coarse estimated Doppler scale in a 50m channel using the first 3 channel taps for 10 times and 50 times the original sampling rate respectively. The estimated Doppler scale values are more scattered with sampling rate of 10 compared to 50. The corresponding BER plots are given in Fig. 3.15 and in Fig. 3.16. Fig. 3.17 and 3.18 illustrates the coarse estimated Doppler scale in a 50m channel using only the first channel tap for 10 times

and 50 times the original sampling rate respectively. The estimated Doppler scale values are more scattered with sampling rate of 10 compared to 50. The corresponding BER plots are given in Fig. 3.19 and in Fig. 3.20.

Ideally, estimation with 3 taps should provide better accuracy. At the same time higher number of taps inject more noise in the estimation calculation. In the above figures it can be seen that compared to estimation with 3 taps, estimation with 1 tap gives less scattered values in both sampling rate situations.

During estimation and data sampling, when the rate is 10 or 50, the Doppler shifted samples are not hit because of low sampling rate and because of rounding the indexes during simulation. So, even though there is Doppler shift, the effect is not seen in the above BER plots, that is Doppler absence and presence act the same way.

The estimated values in 100m channel using 3 taps and 10 times sampling rate is more scattered compared to the corresponding values in 50m channel. The estimated values in 100m channel using 1 tap and 50 times sampling rate is more scattered compared to the corresponding values in 50m channel.

Fig. 3.25 and Fig. 3.26 illustrate the BER in a 100m channel, where the Doppler scale is estimated using the first 3 channel taps with sampling rate of 10 and the data signal is sampled 1000 times the sampling rate. Fig. 3.27 and 3.28 illustrate the BER in a 100m channel, where the Doppler scale is estimated using the first 3 channel taps with sampling rate of 50 and the data signal is sampled 1000 times the sampling rate. In the above BER figures, the estimation is done with a sampling rate of 10 and 50. But to show how Doppler compensation works, data is sampled at 1000, so even after the rounding of sample index, some Doppler scale values cause Doppler shift and hence Doppler distortion. For these effective Doppler scale shifts, when the data samples are shifted back with the exact Doppler scale values, they show BER performance similar to the case without Doppler. However when, the estimated Doppler scale values are used to resample, some of the BER plots return to no Doppler state but others are not fully compensated and hence the BER performance is not good for those Doppler scales.

3.5.2   Simulation Using Second Algorithm

Fig. 3.21 and 3.22 illustrates the coarse estimated Doppler scale in a 100m channel using the first 3 channel taps for 10 times and 50 times the original sampling rate respectively.   The corresponding BER plots are given in Fig. 3.23 and in Fig. 3.24.

During estimation and data sampling, when the rate is 10 or 50, the Doppler shifted samples are not hit because of low sampling rate and because of rounding the indexes during simulation. So, even though there is Doppler shift, the effect is not seen in the above BER plots, that is Doppler absence and presence act the same way.

Fig. 3.29 and Fig. 3.30 illustrate the BER in a 100m channel, where the Doppler scale is estimated using the first 3 channel taps with sampling rate of 10 and the data signal is sampled 1000 times the sampling rate. Fig. 3.31 and 3.32 illustrate the BER in a 100m channel, where the Doppler scale is estimated using the first 3 channel taps with sampling rate of 50 and the data signal is sampled 1000 times the sampling rate. In the above BER figures, the estimation is done with a sampling rate of 10 and 50. But to show how Doppler compensation works, data is sampled at 1000, so even after the rounding of sample index, some Doppler scale values cause Doppler shift and hence Doppler distortion. For these effective Doppler scale shifts, when the data samples are shifted back with the exact Doppler scale values, they show BER performance similar to the case without Doppler. However when, the estimated Doppler scale values are used to resample, some of the BER plots return to no Doppler state but others are not fully compensated and hence the BER performance is not good for those Doppler scales.

In comparison to the first method, the second estimation method performs worse. The estimated Doppler scale values deviate far from the actual values compared to the first estimation method. This is due to the fact that in the second estimation method, noisy data symbol is autocorrelated in addition to the cross correlation of reference OFDM symbol leading to more noise in the calculation.

3.6 Conclusion and Future Research on Varying Doppler Shift over OFDM Subcarriers

Doppler shift in frequency domain is caused by time selectivity of UAC channels in time domain. This Doppler shift varies considerably over OFDM subcarriers in UAC OFDM causing ICI and subsequently loss of orthogonality that may degrade receiver performance.

The variation of Doppler shift over OFDM subcarriers can be represented with Doppler scale in time domain. In this chapter, two Doppler scale estimation methods are proposed. In both methods, one known reference OFDM symbol is transmitted prior to the data symbols. The known reference is cross correlated with the known local symbol at the receiver. In the first method, with respect to the known tap locations the cross correlated peak locations give a coarse estimation of the Doppler scale. In the second method, the cross correlated peaks of the reference are compared to the auto correlated peaks of a data symbol to provide estimation of the Doppler scale. Between these two methods, first one provides more estimation accuracy since clean reference is used without usage of noisy data symbol. In the first method, the knowledge of the channel taps in the absence of Doppler is needed. In the second method, although this prior knowledge is not necessary, the noise from the auto correlated noisy data contribute to more noise in estimation.

As a continuation of this research in the future, strong code selection in the reference OFDM, which is robust against UAC channels to reduce estimation error can be investigated.
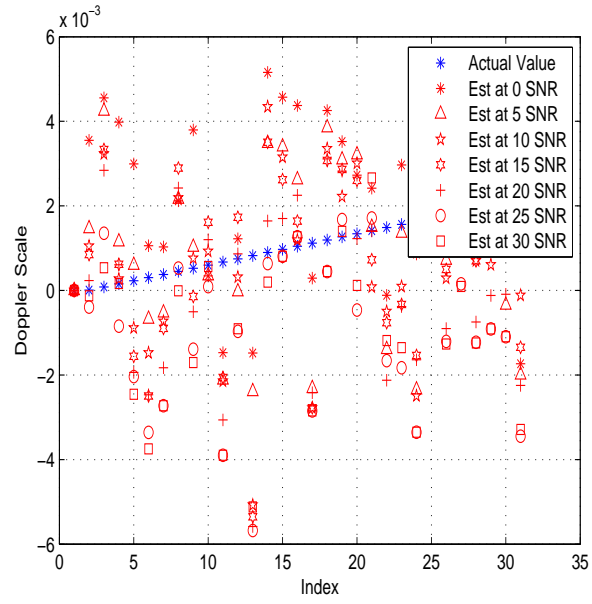
Figure 3.5 First Estimation Method, Channel 100m, Taps 3, Rate 10
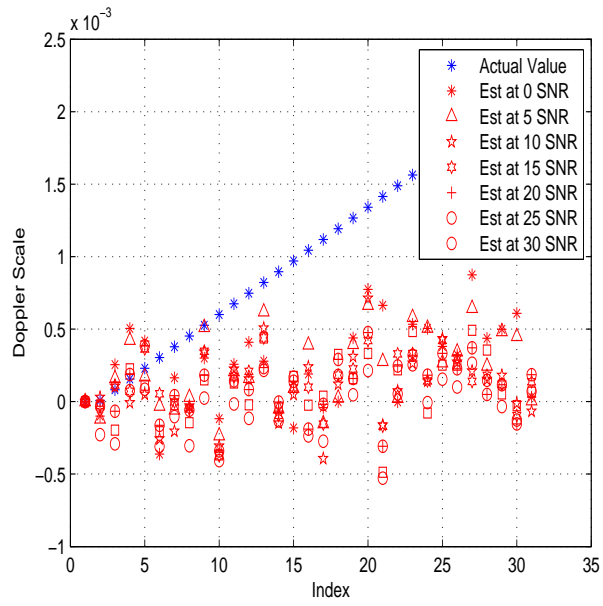
Figure 3.6 First Estimation Method, Channel 100m, Taps 3, Rate 50
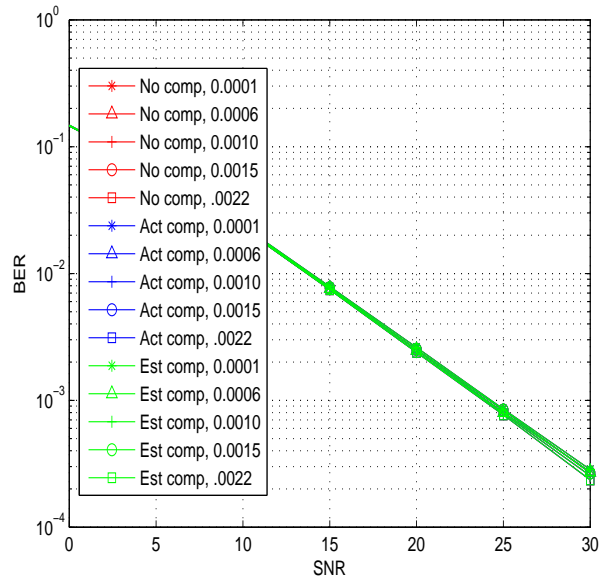
Figure 3.7 BER, Rirst Estimation Method, Channel 100m, Taps 3, Rate 10
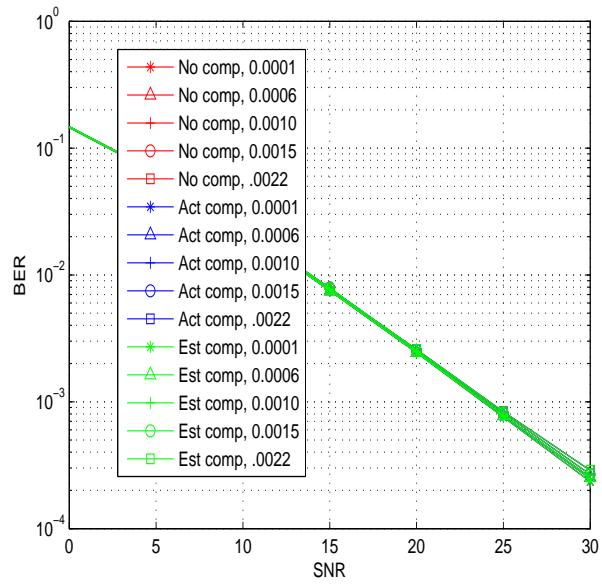
Figure 3.8 BER, First Estimation Method, Channel 100m, Taps 3, Rate 50
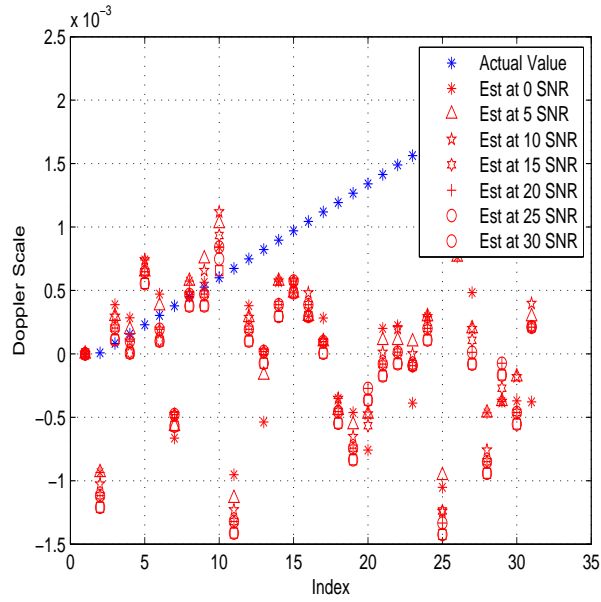
Figure 3.9 Doppler Scale, First Estimation Method, Channel 100m, Taps 1, Rate 10
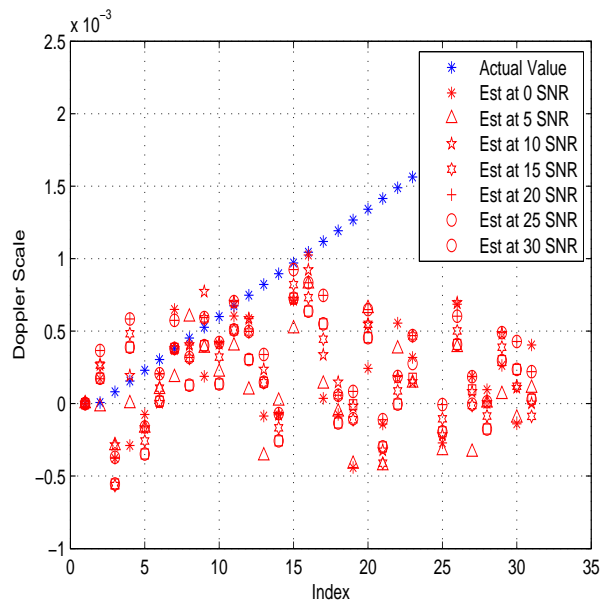
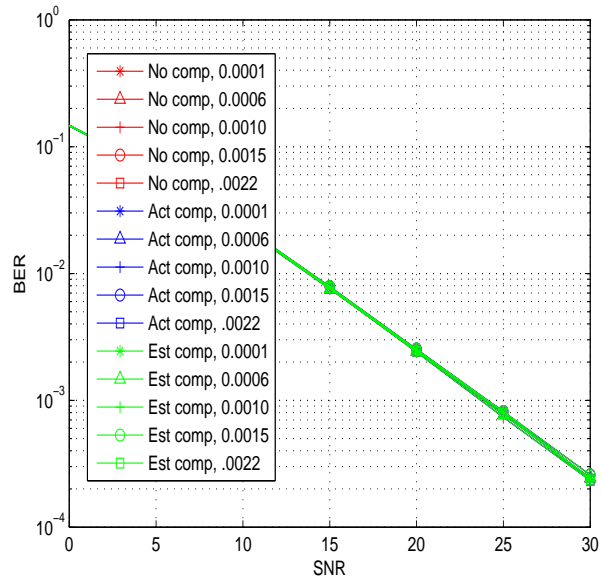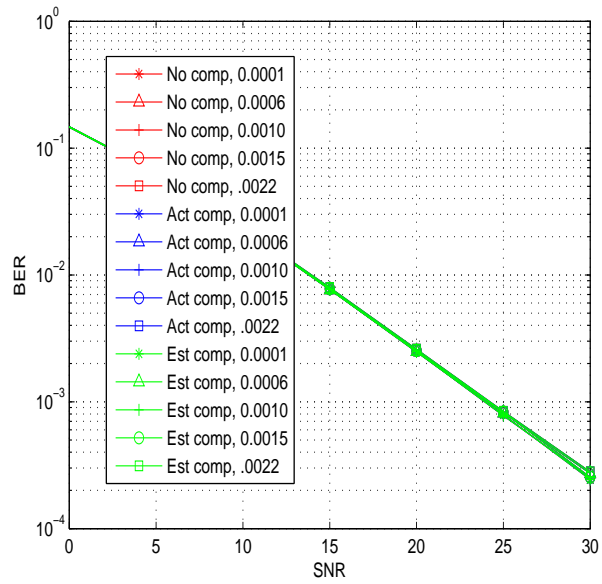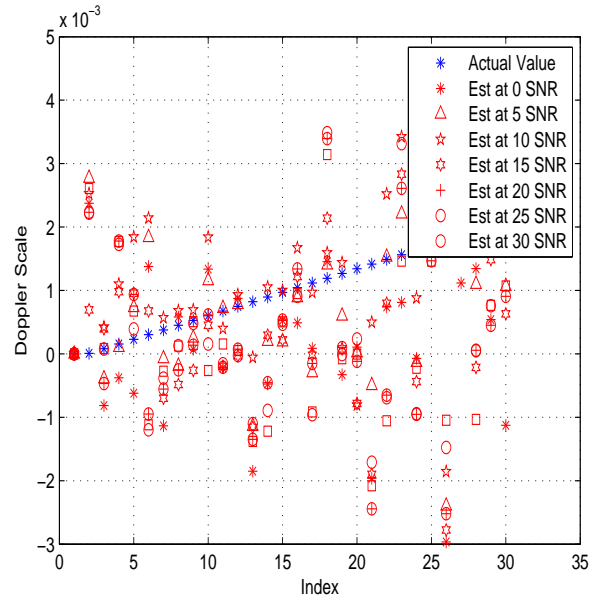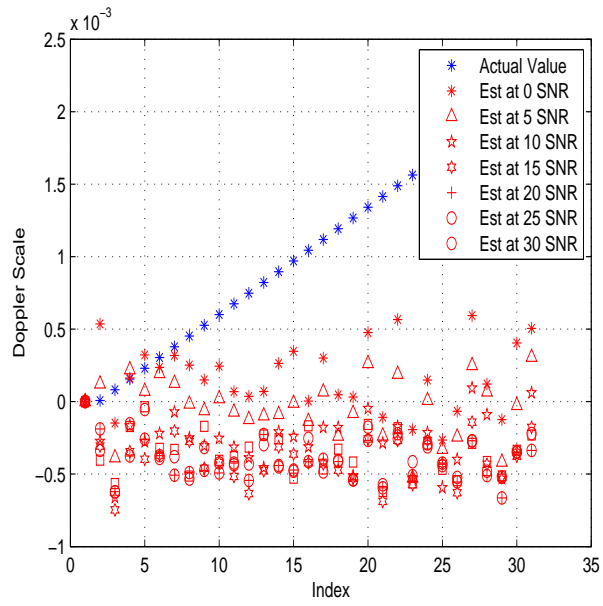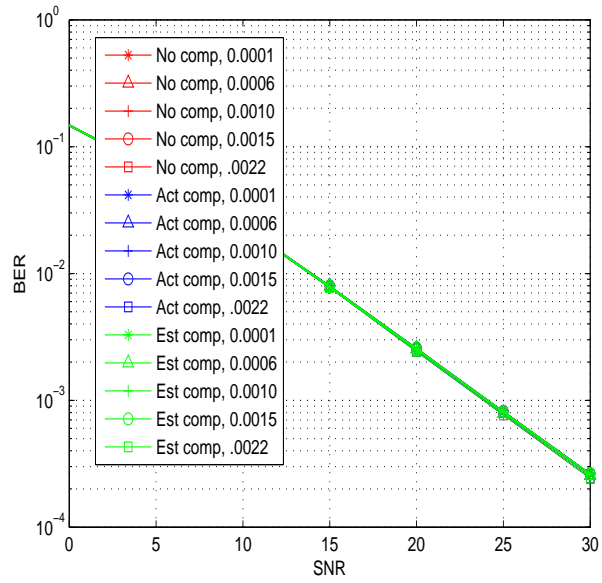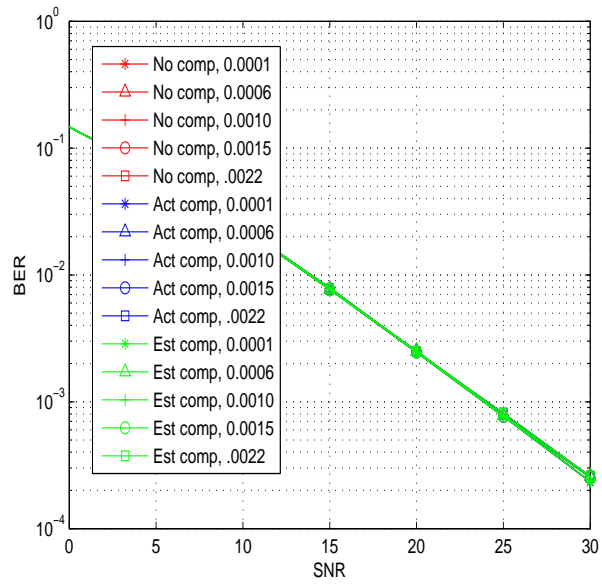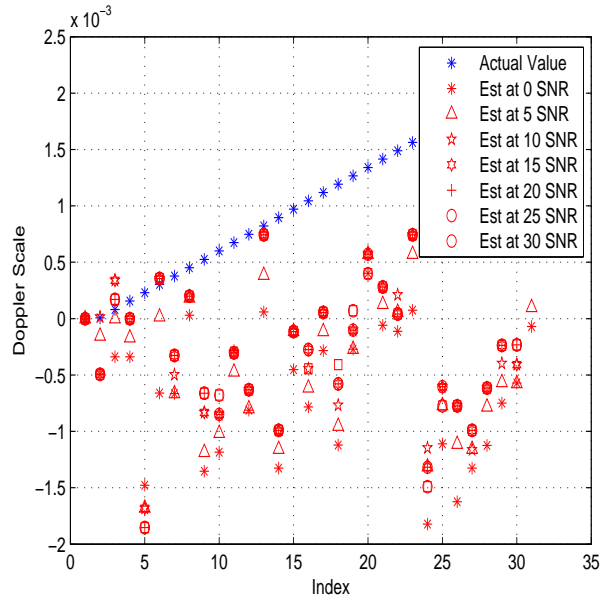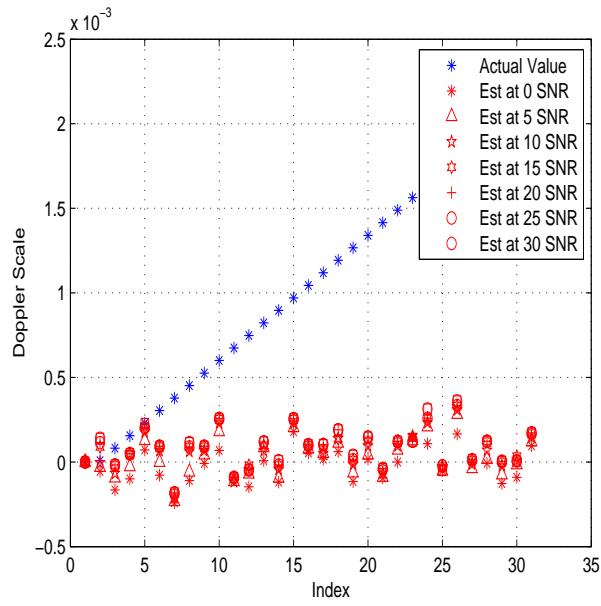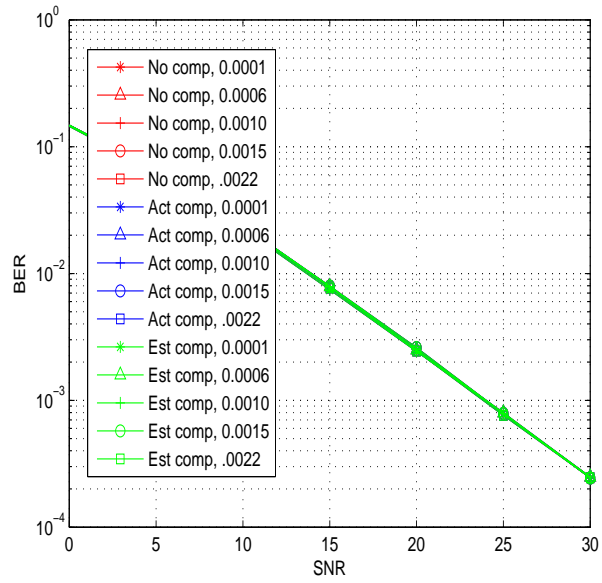Figure 3.10 Doppler Scale, First Estimation Method, Channel 100m, Taps 1, Rate 50

Figure 3.11 BER, First Estimation Method, Channel 100m, Taps 1, Rate 10

Figure 3.12 BER, First Estimation Method, Channel 100m, Taps 1, Rate 50

Figure 3.13 First Estimation Method, Channel 50m, Taps 3, Rate 10

Figure 3.14 First Estimation Method, Channel 50m, Taps 3, Rate 50

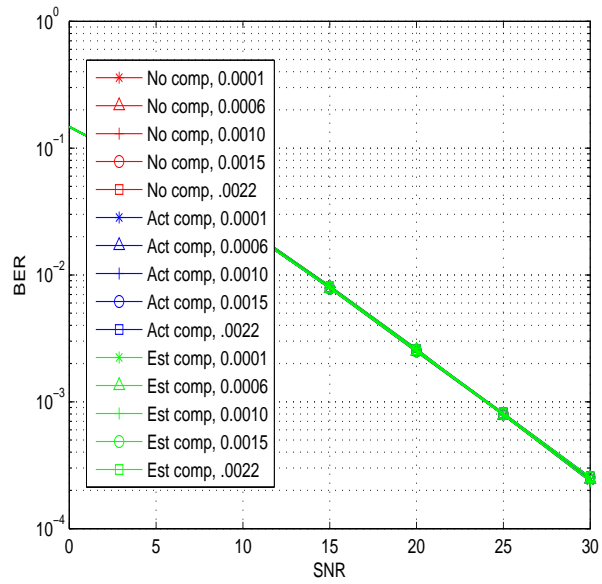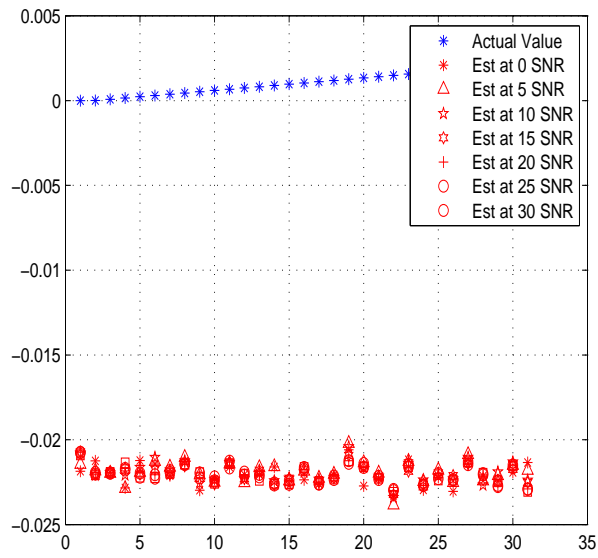Figure 3.15 BER, First Estimation Method, Channel 50m, Taps 3, Rate 10

Figure 3.16 BER, First Estimation Method, Channel 50m, Taps 3, Rate 50

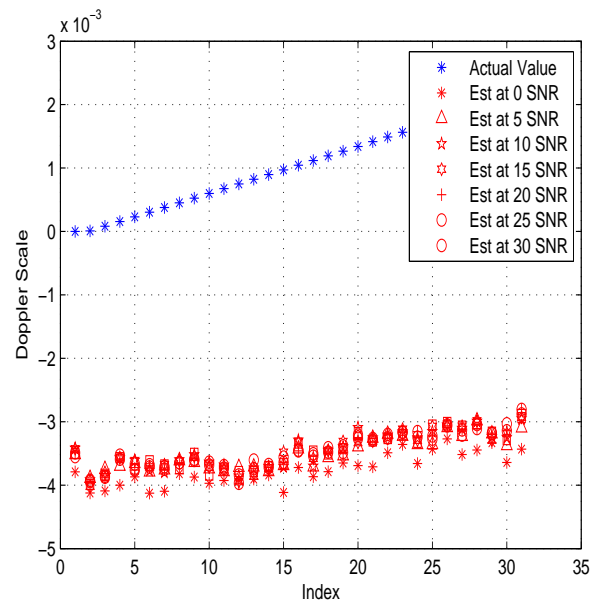Figure 3.17 First Estimation Method, Channel 50m, Taps 1, Rate 10

Figure 3.18 First Estimation Method, Channel 50m, Taps 1, Rate 50

Figure 3.19 BER, First Estimation Method, Channel 50m, Taps 1, Rate 10

Figure 3.20 BER, First Estimation Method, Channel 50m, Taps 1, Rate 50

Figure 3.21 Second Estimation Method, Channel 100m, Taps 3, Rate 10

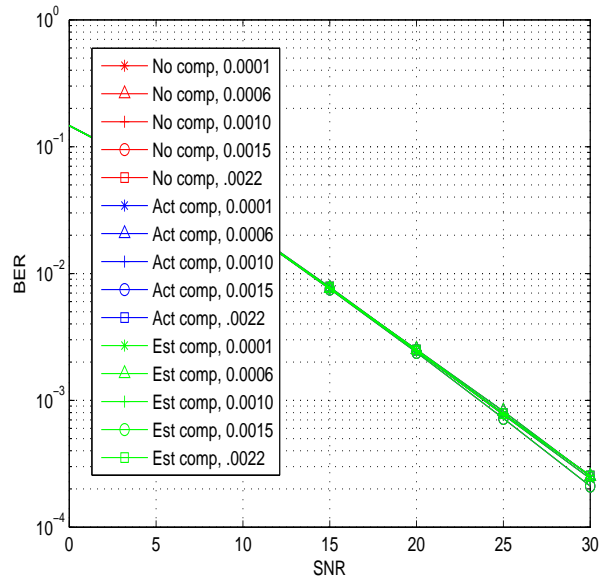Figure 3.22 Second Estimation Method, Channel 100m, Taps 3, Rate 50

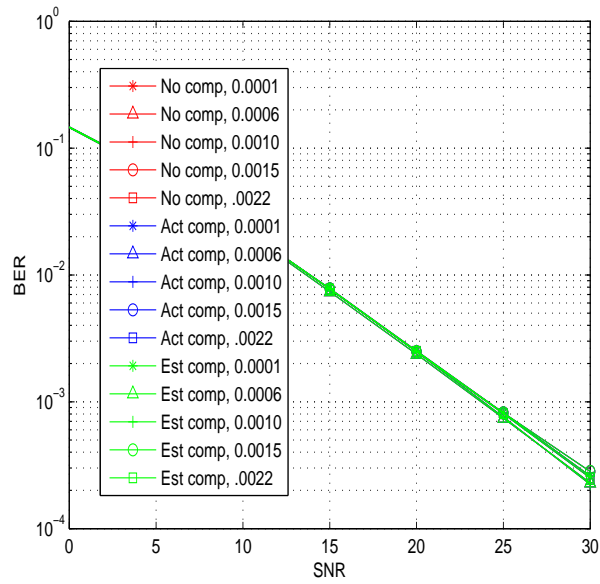Figure 3.23 BER, Second Estimation Method, Channel 100m, Taps 3, Rate 10

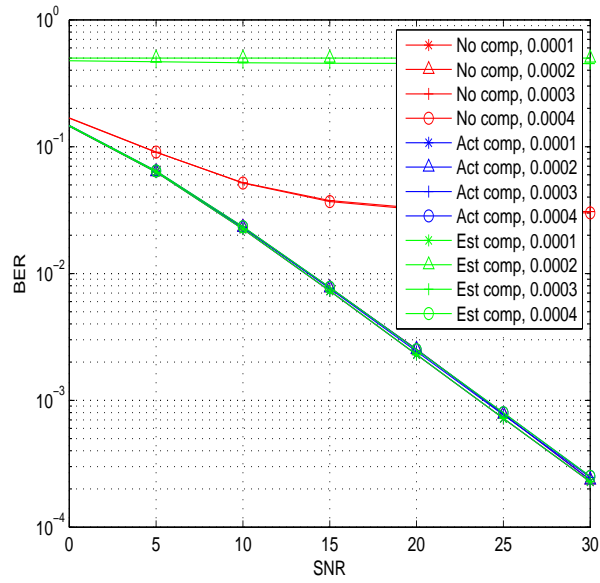Figure 3.24 BER, Second Estimation Method, Channel 100m, Taps 3, Rate 50

Figure 3.25 BER, First Method, Channel 100m, Taps 3, Est. Rate 10, BER Rate 1000, First 4
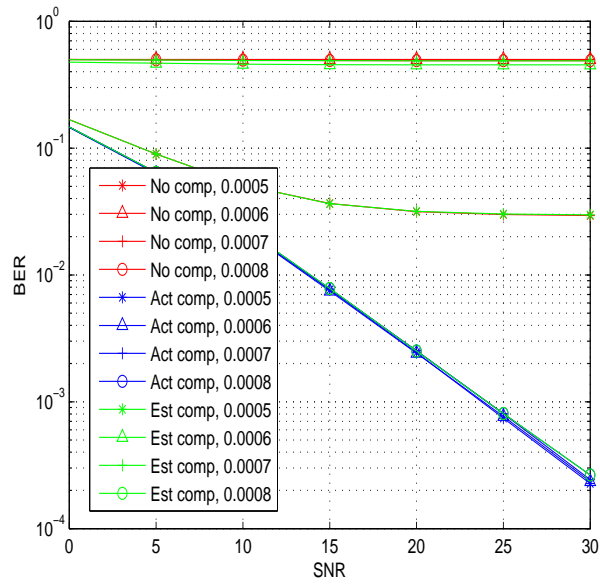

Figure 3.26 BER, First Method, Channel 100m, Taps 3, Est. Rate 10, BER Rate 1000, Last 4
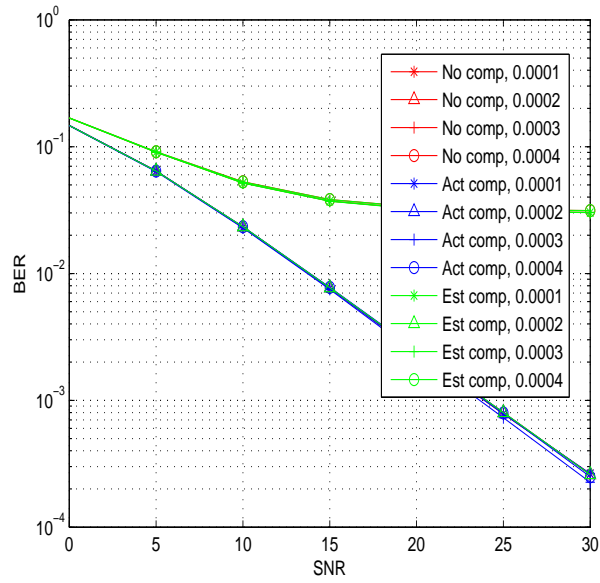
Figure 3.27 BER, First Method, Channel 100m, Taps 3, Est. Rate 50, BER Rate 1000, First 4
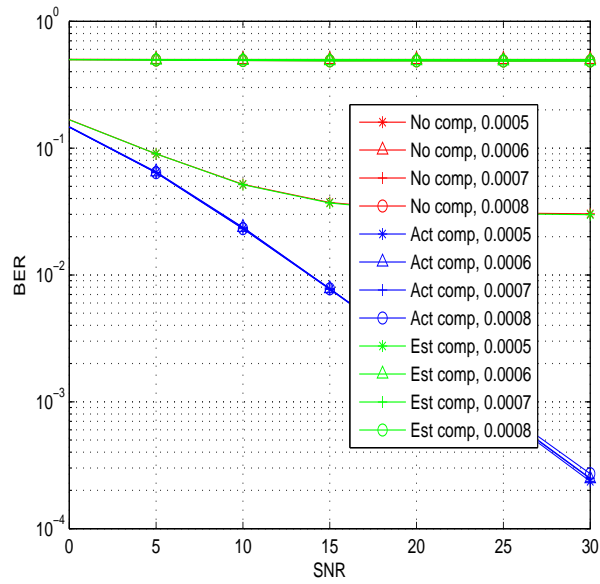

Figure 3.28 BER, First Method, Channel 100m, Taps 3, Est. Rate 50, BER Rate 1000, Last 4

Figure 3.29 BER, Second Method, Channel 100m, Taps 3, Est. Rate 10, BER Rate 1000, First 4

Figure 3.30 BER, Second Method, Channel 100m, Taps 3, Est. Rate 10, BER Rate 1000, Last 4
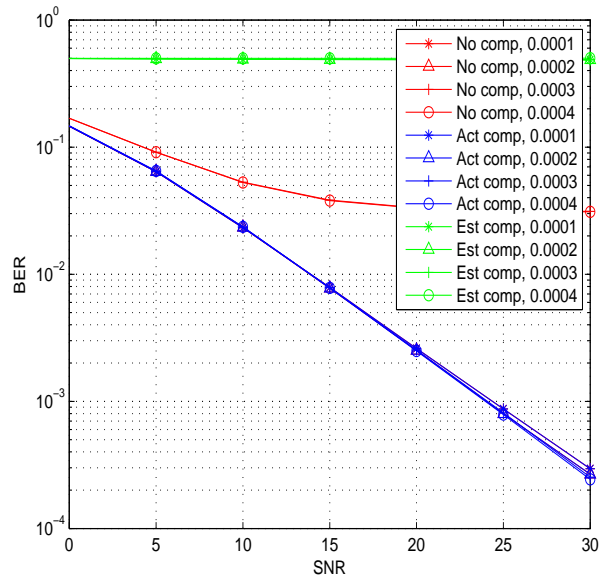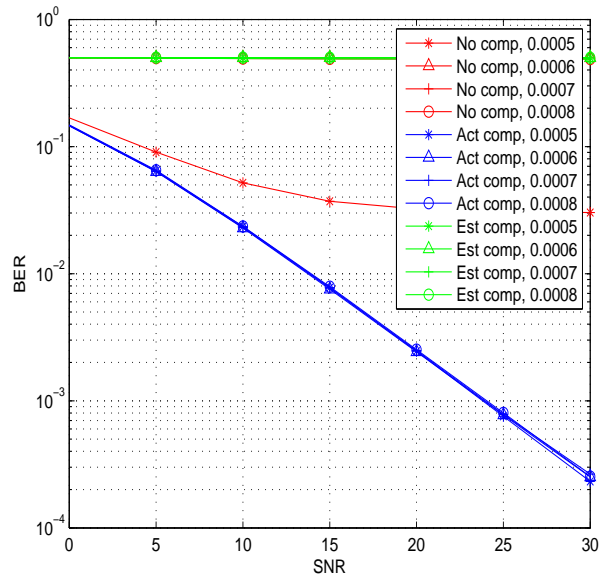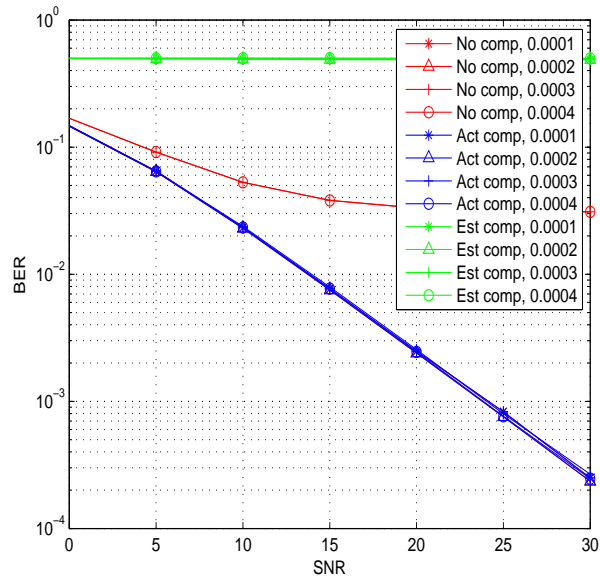
Figure 3.31 BER, Second Method, Channel 100m, Taps 3, Est. Rate 50, BER Rate 1000, First 4
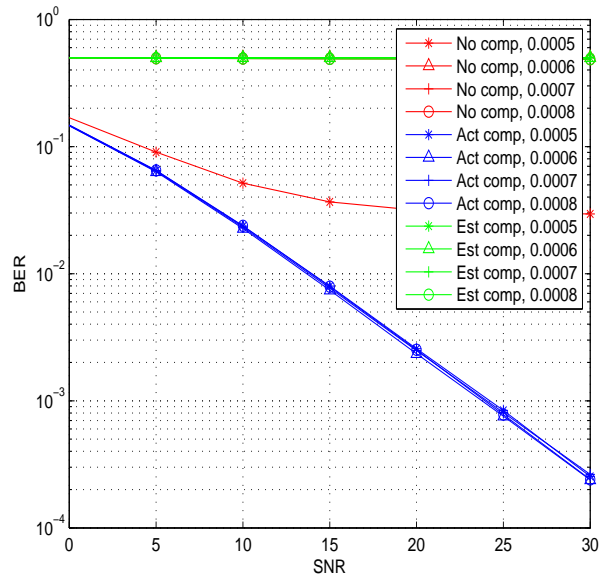

Figure 3.32 BER, Second Method, Channel 100m, Taps 3, Est. Rate 50, BER Rate 1000, Last 4

CHAPTER 4 :

**PERFORMANCE UNDER INTER-FRAME AND INTER-SYMBOL
INTERFERENCE IN ULTRA-WIDEBAND CHANNELS**

Ultra Wideband (UWB) Systems [1] take advantage of collecting energy from a large number of multipaths. In high data rate systems for TH UWB transmission, these large number of multipaths may leak into neighboring frames causing inter-frame interference (IFI). Most studies so far avoid this IFI by placing one or more constraints on chip length, frame length, minimum pulse to pulse duration, etc. In this first part of the chapter, IFI is investigated for BPSK and PPM modulations in coherent transceivers. It is shown that IFI effect is insignificant for these modulation options and transceiver architectures. Therefore, the constraints to avoid IFI can be removed for those systems.

4.1 Inter-frame Interference in Ultra-Wideband

Ultra-wideband systems require transmission of very short pulse (in the order of nano seconds) or pulse trains in extremely high bandwidth (greater or equal to 500 MHz) producing a large number of resolvable multipaths. Coherent receivers such as RAKE receivers can collect all the energy from these paths at the cost of estimating an impractically large number (in the order of hundreds) of finger locations and channel coefficients. Sub-optimal RAKE receivers such as partial RAKE or selective RAKE [41] reduce such estimation by collecting energy from the first few or from the strongest multipaths, respectively. In coherent UWB transceivers, transmitted information is typically replicated over multiple pulses over multiple frames using popular schemes such as time hopping (TH). In a TH environment, pulses are transmitted within chips per frame

---

[1]Parth of this chapter has been published in Proc. IEEE Vehicular Technology Society (VTC), Montreal, Canada, Sep 2006, in Proc. IEEE Radio and Wireless Symposium (RWS), Orlando, FL, Jan 2008 and in Geron Technology Journal, vol. 7, no. 1, pp. 4857, Jan 2008. Permission is included in Appendix C.

where the chip index determines the hopping sequence. If minimum pulse to pulse duration is not chosen carefully, multipaths within a symbol from one frame may leak into the next frame of the same symbol causing inter frame interference (IFI). Modulation options, multiple accessing schemes, type of transceiver used all influence IFI, its amount and its effect on the system. Depending on the leakage, IFI may or may not cause problem at the receiver. In most studies in the past, IFI had been avoided by employing restrictions on chip length, frame length, minimum pulse to pulse duration etc. [42]- [45]. In [46], IFI leading to (ISI) and inter block interference (IBI) have been considered and evaluated using digital single carrier and multicarrier spreading codes in RAKE type of receivers.

The main objective here is to carry out a comprehensive analysis and simulation of IFI in context of popular UWB modulation schemes and commonly used UWB coherent transceiver in TH environment. It is proved that IFI effect is negligible for high data rate systems and therefore, the assumptions to avoid IFI can be safely removed. In the next section TH-IR scheme is presented in terms of a generic system model.

4.2 Ultra-wideband Signal Structure

4.2.1 TH-IR Systems

Fig. 4.1 represents transmission of a single user in a generic TH multiple access environment. Information is transmitted in blocks or bursts where each block is an array of N symbols. Pulses of each user are hopped in time over multiple frames per symbol according to unique hopping code. The following notations are used for various system parameters. T_s denotes symbol period including guard interval between symbols, N_f denotes number of frames or pulse repetition per symbol, T_f represents frame duration, T_c is chip duration, N_c is number of chips per frame, T_p is pulse duration and T_g is maximum excess delay including pulse duration. Naturally, T_s may govern data rate ($R = 1/T_s$), N_f may govern processing gain and PN code limit. T_f, N_c and T_c may govern duty cycle and the multiple access capability (i.e. the number of users that a frame can support). The parameters are related by $T_s = N_f * T_f$ and $T_f = N_c * T_c$.
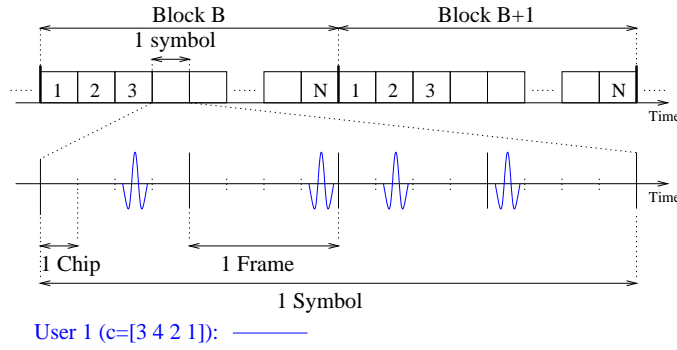
Figure 4.1 TH-UWB-IR Signaling Structure.

4.2.2   TH-IR System Model

The generic transmitted and received signal for user k in a multipath environment can be denoted as $s^k(t)$ and $r^k(t)$ respectively and is expressed as follows,

$$s^k(t) = \sum_j A\beta^k_{\lfloor j/N_f \rfloor}\omega(t - jT_f - c^k_j T_c - b^k_{\lfloor j/N_f \rfloor}\delta) \tag{4.1}$$

$$
\begin{aligned}
r^k(t) &= \sum_j \sum_{l=0}^{L-1} A\beta^k_{\lfloor j/N_f \rfloor}\gamma_l \\
&\quad \cdot\omega(t - jT_f - c^k_j T_c - b^k_{\lfloor j/N_f \rfloor}\delta - \tau_l) + n(t)
\end{aligned}
\tag{4.2}
$$

where j is the frame index, A represents amplitude of each pulse, $\beta^k_{\lfloor j/N_f \rfloor}$ is the change in amplitude according to pulse amplitude modulation (PAM) schemes and $\omega(t)$ represents the transmitted and received pulse. Decimal codes c^k_j are TH codes unique to user k. δ is the modulation index and $b^k_{\lfloor j/N_f \rfloor}$ represents bit value when Pulse Position Modulation (PPM) is used. γ_l represents path coefficient and τ_l represents path delay of the lth received path. $n(t)$ is the additive white Gaussian noise (AWGN) with double-sided spectrum of $N_o/2$. For simplicity TH scheme is considered in a single user environment in the following discussions and can be extended to any number of users. In the following section, parameters affecting IFI are discussed.
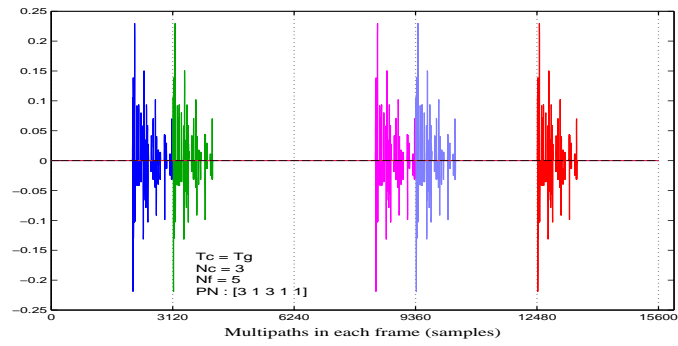
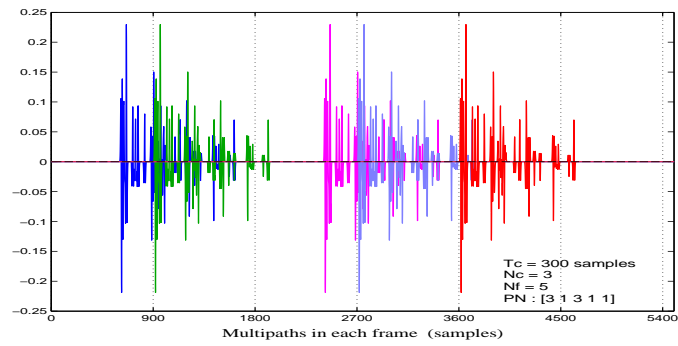Figure 4.2 Received Signal, PR_m Equals Maximum Excess Delay

Figure 4.3 Received Signal, PR_m is Less than Maximum Excess Delay
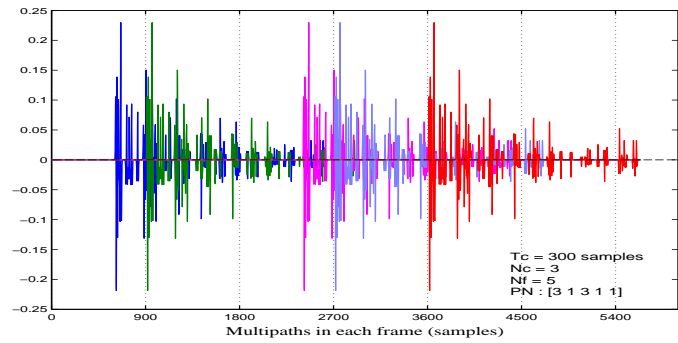

Figure 4.4 Received Signal when Maximum Excess Delay is Greater than Frame Length

4.3   Is Inter-frame Interference (IFI) a Problem

Minimum pulse to pulse duration is defined as the minimum distance in time between any two consecutive pulses of two frames within a symbol and can be denoted as PR_m. In most

studies so far, PR_m is considered to be greater or equal to T_g of the channel. This inherently avoids interference from multipaths between chips or pulses of any two frames within the same symbol. It can be easily understood that in the worst case scenario PR_m is one chip length. For the purpose of discussion in this section, transmission of one symbol over 5 frames and 3 chips per frame is considered. PN sequence is [3 1 3 1 1], which is one of the sequences generated randomly according to TH code generation formula in [47]. The channel model considered is CM1 [48] and the modulation is BPSK. According to the PN sequence, PR_m is equal to one chip length. Fig. 4.2 represents each received pulse and its multipaths when PR_m is equal to T_g [2]. If however, PR_m is smaller than T_g then multipaths from one or more neighboring frames can leak onto other frames. PN sequence may dictate the amount of leakage. This leakage is inter-frame interference (IFI) and is represented in Fig. 4.3. Because PN sequence is random, some frames may have more or less IFI, while others may not have any. T_g in Fig. 4.3, is greater than 3 chip lengths. Because of the considered PN sequence, this causes interference from frame 1 onto frame 2, frame 3 onto frame 4 and frame 4 onto frame 5. If interference from future frames is ignored at this point (for a causal system), frame 1 and 3 are interference free. When a pulse is transmitted in the largest chip index (pulse is at the border of a frame) even with small T_g, naturally multipaths leak from its frame to the next. This leakage may cross over to distant frame or frames if the frame length is less than T_g. This may cause IFI to neighboring as well as distant frames within a symbol and is shown in Fig. 4.4. IFI may also cause ISI by leakage between frames of different symbols in the absence of guard interval.

IFI is discussed in terms of various system parameters when constraint (PR_m greater or equal to T_g) against IFI in TH UWB systems is relaxed. In IEEE UWB channel models, in CM1, CM2, CM3 the mean excess delays are 5.05, 10.38, 14.18 nsec respectively [48]. Therefore, to avoid IFI, PR_m needs to be on average, at least equal to these values. This may result in a large T_c in a TH environment. In high data rate UWB systems, T_s is small. For a data rate of 100Mbps with transmitter and receiver distance of 10 m [49], $T_s = 10nsec$. It is clearly seen from these practical values that it may be impossible to avoid IFI in high data rate (data or symbol rate $R = 1/T_s$)

---

[2]Minimum pulse to pulse duration for this example is the distance between chip 3 of first frame and chip 1 of second frame

systems. In the worst case , to avoid IFI between adjacent frames, T_c needs to be at least equal to T_g. For a large T_c, if data rate is sacrificed i.e. T_s is large, N_f competes with N_c or number of users (for constant T_s). Large N_f provides a good processing gain and more flexible PN code limit. This may force smaller T_f and reduce N_c or users in the system. The above case leads to sacrificing data rate and user capacity to avoid IFI. For a constant T_s, T_f cannot be too small and therefore N_f cannot be too large leading to a limit on processing gain and PN code. In another case, data rate is still sacrificed to secure against IFI but T_f is allowed to increase for a constant T_s. Increase in T_f may increase user capacity but may compromise N_f leading to sacrificing processing gain and limit on PN code. The cases considered so far to avoid IFI may result in sacrificing one or more parameters such as data rate, user capacity, processing gain or possible number of different PN codes. For very high data rate systems, IFI is almost unavoidable. For low data rate systems, if IFI constraints is removed i.e. T_c is small, N_f may be increased, increasing processing gain and PN code limit. Also T_f may be large to provide higher user capacity. Therefore allowing IFI may increase data rate and may relax system parameter constraints. Note that guard interval between symbols to avoid ISI still effects data rate. In the next section, IFI in terms of popular modulation options and commonly used coherent transceiver is analyzed and evaluated.

4.4 Effects of IFI on Various Modulation Options and Coherent Transceiver Architecture

In this section, IFI is analyzed using equations and simulation for BPSK and PPM modulations in All-Rake [41] receivers. For simplicity, certain constraints are first applied and removed later on.

- ISI and MUI: Guard interval is present between symbols in order to avoid ISI. Single user transmission avoids multiple user interference (MUI).

- Channel: Each frame experiences same channel within a symbol. Channel is perfectly estimated at the receiver.
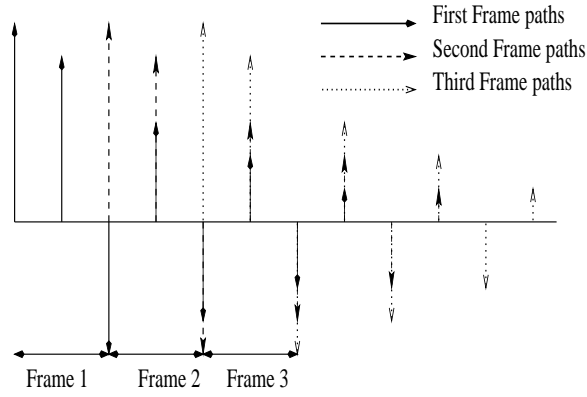
Figure 4.5 IFI with Equal Delay

- Multipath pulse: Interfering pulse from interfering path aligns perfectly with the interfered pulse. The pulse shape is same in every path.

- Delay: Arrived paths are at equal distance from each other. In reality path delays are random.

- Transmit/Receive pulse: Transmitted and received pulses are same. In reality they may be different.

Frame in question may receive both causal (previous frame) and non-causal (future frames) IFI. In reality, non-causal situation for prevail for very short chip lengths. In Fig. 4.4, frame 4 is affected by both causal and non-causal interference from frames 3 and 5 respectively.

4.4.1 Analysis of IFI

According to the assumptions discussed, if equation (4.2) is simplified for one user, single bit transmission, for unit pulse amplitude, and for BPSK, the received signal for each bit with no IFI can be expressed as,

$$r(t) = \sum_j \sum_{l=0}^{L-1} \gamma_l \beta_j \omega(t - jT_f - c_j T_c - \tau_l) + n(t) \tag{4.3}$$

Ideal All-Rake receivers, gather energy from all arrived multipaths [41]. To understand IFI, in the simplest form, 3 consecutive frames of received signal containing random delay multipaths can

100

be considered. If frame 2 is the frame of interest, then, some paths of frame 2 may or may not receive contribution from frame 1 as well as frame 3. Fig. 4.5 considers restricted delay case where the delay between any two consecutive arrived paths is assumed equal. In a more generic form, if frame in consideration is j and the interfering frames are denoted by i, then for jth frame, for each multipath, there may or may not be contribution from other multipaths from ith frame or frames. For each single path/tap l in jth frame, IFI contribution is the summation of all the contributions from mth paths from other i frames (previous and future for causal and non-causal respectively). Then for a single lth tap of frame j, for equal delay case, received signal is expressed as,

$$
\begin{aligned}
&\gamma_l \beta_j \omega(t - jT_f - c_j T_c - \tau_l) \\
&+ \sum_{m=0,i}^{m=L-1} \gamma_{mi} \beta_i \omega(t - iT_f - c_i T_c - \tau_{mi}) + n_l(t) \\
&m \text{ is not equal to } l
\end{aligned}
\tag{4.4}
$$

where β_j equals β_i (pulse polarity same within one bit). Combining equations (4.3) and (4.4), the received signal for a bit is,

$$
\begin{aligned}
r(t) \;=\; & \sum_j \sum_{l=0}^{L-1} \Big(\gamma_l \beta_j \omega(t - jT_f - c_j T_c - \tau_l) \\
& + \sum_{m=0,i}^{m=L-1} \gamma_{mi} \beta_i \omega(t - iT_f - c_i T_c - \tau_{mi}) + n_l(t) \Big) \\
& m \text{ is not equal to } l, \\
& m > l \text{ if } j > i \text{ (causal)}, \\
& m < l \text{ if } j < i \text{ (non causal)}
\end{aligned}
\tag{4.5}
$$

where $n_l(t)$ is the AWGN noise contribution on each tap of jth frame. The three conditions in (4.5) are denoted as C. At the receiver with perfect channel estimation, let template for a single

tap be $\gamma_q \omega(t - jT_f - c_jT_c - \tau_q)$, where taps are 0,1,2...q...L-1. Then local template

$$R(t)_{t=kT_s} = \sum_j \left(\Phi(t) \sum_{l=0}^{L-1} \left(\gamma_l \beta_j \omega(t - jT_f - c_jT_c - \tau_l) + \right.\right.$$
$$\left.\left. \sum_{m=0,i}^{m=L-1} \gamma_{mi}\beta_i \omega(t - iT_f - c_iT_c - \tau_{mi}) + n_l(t) \right) \right), \quad C$$

for All-Rake receiver can be expressed as $\Phi(t) = \sum_{q=0}^{L-1} \gamma_q \omega(t - jT_f - c_jT_c - \tau_q)$. Using equation (4.5) and the template, the decision variable at the output of correlators sampled at T_s can be expressed as equation for $R(t)$. It is clearly seen that the first part of $R(t)$ is the desired non IFI term and the third part is the AWGN noise contribution. It is the second term that is undesired due to IFI contribution. For BPSK modulation, error occurs when $R(t) > 0$ if negative pulse is transmitted or $R(t) < 0$ if positive pulse is transmitted. Similar to the derivation of BPSK, for binary PPM, equation of received signal for each bit, for one user, for single bit transmission and for unit pulse amplitude in non IFI case is derived and not shown due to space limitation. The pulses at two different positions for PPM are considered orthogonal i.e. δ is at least equal to T_p. Within one PPM bit, PPM pulse is situated on same side of nominal index in a chip for every frame.

$$R_1(t)_{t=kT_s} = \sum_j \left(\psi(t) \sum_{l=0}^{L-1} \left(\gamma_l \omega(t - jT_f - c_jT_c - b_j\delta - \tau_l) \right.\right.$$
$$+ \sum_{m=0,i}^{m=L-1} \gamma_{mi}\omega(t - iT_f - c_iT_c - b_j\delta - \tau_{mi})$$
$$\left.\left. + n_l'(t) \right) \right), \quad C$$

$$R_2(t)_{t=kT_s} = \sum_j \psi(t) \sum_{l=0}^{L-1} n_l''(t) \tag{4.6}$$

Therefore, PPM acts similar to BPSK under the assumptions of section 4.4. Interfering pulses (mth paths) fall on the same side of nominal as the interfered pulse (lth path). In equal delay case, similar to BPSK, equation for PPM received signal can be derived. Within the same bit, $b_{\lfloor j/N_f \rfloor}\delta$ is same in all frames and can be represented as $b_j\delta$. Let PPM template for All-Rake

be $\psi(t) = \sum_{q=0}^{L-1} \gamma_q \omega(t - jT_f - c_j T_c - b_j \delta - \tau_q)$. For binary PPM, PPM pulse may be on either side of nominal according to bit. Decision variables at the output of correlators, sampled at T_s, is given by equation (4.6) where n'_l is the AWGN noise on the transmitted pulse position and n''_l is the noise on non transmitted position. Using equation (4.6), $R_1(t)$ and $R_2(t)$ are compared and the bit decision is made.

4.4.2 Semi-analytical Simulation Results in IFI Systems

The semi-analytical simulation is carried out using the assumptions of section 4.4. Some of the assumptions are relaxed later and others may be removed in same way. For same pulse in each multipath, IFI part of $R(t)$ for BPSK may contain summation of same pulses as the pulse in the l th path but attenuated by a different path coefficient and may have originated from different frames, different chips and at different multiples of τ_l delay. In this context, IFI part of $R(t)$ may be simplified to depend on path coefficients or channel impulses alone. With further investigation of $R(t)$, it can be seen that IFI effect on each path is the cross correlation between desired path ($l = q$) with interfering paths (m). Same group of multipaths/channel impulses are received in each frame. Therefore, a closer observation of $R(t)$ shows that for each frame, the overall IFI effect from other frames is the autocorrelation of each frame at various lags. If N_f is very large i.e. $N_f = \infty$ and T_f is very small i.e. $T_f = 0$, then a frame can be considered to consist of a short impulse and the bit consists of many such very short duration impulses/frames. Therefore, the auto correlation of channel at various lags may be a measure of varying IFI effect on the bit due to varying IFI contribution from other frames/impulses. To keep close proximity to theoretical $N_f = \infty$, very large number of taps/impulses/frames for each channel model is considered in Table 4.1.

For understanding, first, autocorrelation is carried out for one realization over one actual channel and over one artificial channel (with arbitrary taps less than the number of taps for the actual channel but with same maximum excess delay as the actual channel) for CM1 through CM4 models in Fig. 4.6 and 4.7. In both figures, it is observed that for actual channel with large N_f, auto correlation value at smaller lags is negligible for all four models. This implies that at smaller lags IFI contribution may be large for large N_f and very small T_f but the overall/average IFI

effect of very large number of constructive/destructive interfering impulses may be negligible. For artificial channel with small N_f autocorrelation value at smaller lags is not completely negligible. It implies that at smaller lags, IFI contribution may be small for small N_f but the combined effect of those less number of constructive/destructive frames/impulses may not be entirely destructive. For the artificial channel, since number of taps is not large, depending on the density of taps, more or less interfering frames/impulses hit or not hit the desired frame/impulse and therefore IFI effect may be better or worse than average IFI (N_f very large) and can be denoted as instantaneous IFI. CIR (channel to IFI interference ratio in dB) for actual and artificial channels for CM1 model is simulated in Fig. 4.8. Noise in both cases is the IFI contribution and the signal is the normalized maximum autocorrelation value. For actual channel due to large N_f, at smaller lags, overall IFI effect is lower and so CIR is higher. For artificial channel due to smaller N_f, at smaller lags, overall IFI effect may be higher or lower than large N_f channel. For artificial channel, the variation in CIR curve which is more or less than actual channel at various smaller lags proves the above statement.

In practical situations, number of frames per bit is not ∞, T_f is not zero. Therefore, less contribution of IFI from less number of frames may not make overall IFI effect negligible. Also the random delay between paths make some frames to get more IFI than others. If the interfering paths/pulses don't exactly align with the interfered path/pulse, then there may be a time shift of the mth path pulse i.e. the pulse corresponding to the mth path of ith frame may be represented by $\omega(t - iT_f - c_iT_c - \tau_{mi} \pm \tau_{pp})$, where τ_{pp} is the time shift. This may introduce partial correlation between the lth path pulse and the interfering pulse of the m th path of the i th frame provided pulse shapes are same. If pulse shape varies from one path to another in the equation for $R(t)$, then $\omega(t - iT_f - c_iT_c - \tau_{mi})$ can be different from $\omega(t - jT_f - c_jT_c - \tau_l)$. This may contribute to the variation of IFI on each tap.

Fig. 4.9 take second order Gaussian pulses into account before autocorrelation of actual channels and plot variance of autocorrelation values at various lags for all 4 models. For any convolved channel models, for each realization, at lag 0, the impulses are on top of each other i.e. IFI contribution is maximum. But overall IFI effect is negligible. Therefore, autocorrelation values at lag 0 (the integration of squared energy over all channel impulses convolved with pulse)

Table 4.1 IFI Simulation System Parameters

channel model	CM1, CM2, CM3, CM4
Modulations	BPSK, PPM
N_c,N_f,PN code	3,5,[3 1 3 1 1]
T_c equals T_p (IFI case)	.41ns
T_c (non IFI)	All taps(All-Rake), T_g (PRake)
Sampling Frequency	100GHz
Maximum Excess Delays, T_g nsec,	10, 20, 40, 80
Taps for analysis (actual)	2000, 2000, 4000, 9000
Taps for analysis(artificial)	<2000,<2000,<4000,<9000
No. of realizations (analytical),(actual)	1e3,1e4

directly measures the total energy over all impulses in the entire realization. Variance of these autocorrelation values at 0 lag gives the variation of total energy from one realization to another. For smaller lags IFI contribution is still large and overall IFI effect is relatively small and so autocorrelation value of each realization is still a measure of energy over many channel impulses for that realization. Therefore, with small increase in lag, variance still gives a measure of energy from one realization to another.

For PPM modulation scheme, from equation (4.6), $R_1(t)$ contains three parts as in the case of BPSK and the second part is the IFI contribution. Analysis for BPSK is applicable to PPM as well and results are similar to BPSK.

4.4.3   RAKE Receiver

Local template generation in RAKE receiver implies estimation of γ_q and τ_q for every multipath q. When PR_m is less than T_g, for BPSK and PPM, multipaths leak to the next frame (or vice versa) and may affect the finger assignment strategy, finger amplitude, and phases depending on the location, amplitude and phase of interfering multipaths within the frame of interest. Therefore, template for new finger location or for modified amplitude and/or phase may need to be calculated for each frame. Depending on PN sequence, some frames in a bit have more IFI than others and so channel and finger location estimation may vary from frame to frame over the same symbol. In the next section simulation results of TH-IR UWB systems under IFI is presented.
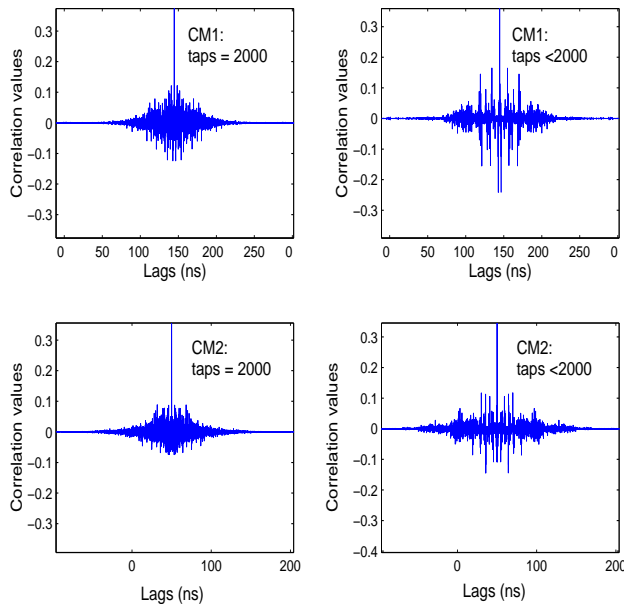
Figure 4.6 Average and Instantaneous IFI Effect: CM1 and CM2

4.5 Simulation Results of IFI in UWB Systems

Simulation is carried out for a single user and simultaneous single bit transmission for All-Rake (considering all taps) and for Partial RAKE (PRake) receivers with BPSK and PPM modulations using parameters in Table 4.1. For $T_p = .41ns$, T_s is 6.15 ns and .data rate is 163 Mbps. For shorter pulses, simulation can also be carried out for higher data rate such as 200Mbps as in WPAN or 802.153a. IFI performance closely coincides with non IFI for All-Rake with both BPSK and PPM modulation in Fig. 4.10 and for Partial RAKE, with both BPSK and PPM in Fig. 4.11. Due to the space limitation all channel models are not shown. Although for partial RAKE, number of taps is less than All-Rake, the constructive/destructive paths is sufficient to cancel each other in overall IFI effect over many symbols and IFI performance closely resembles non IFI case. In the following section possible future research direction is provided.

4.6 Conclusion and Future Research on IFI in UWB Systems

IFI is almost unavoidable for very high data rate UWB Impulse Radio systems. For single bit transmission, in RAKE receivers with BPSK and PPM modulations, it has been proved semi-
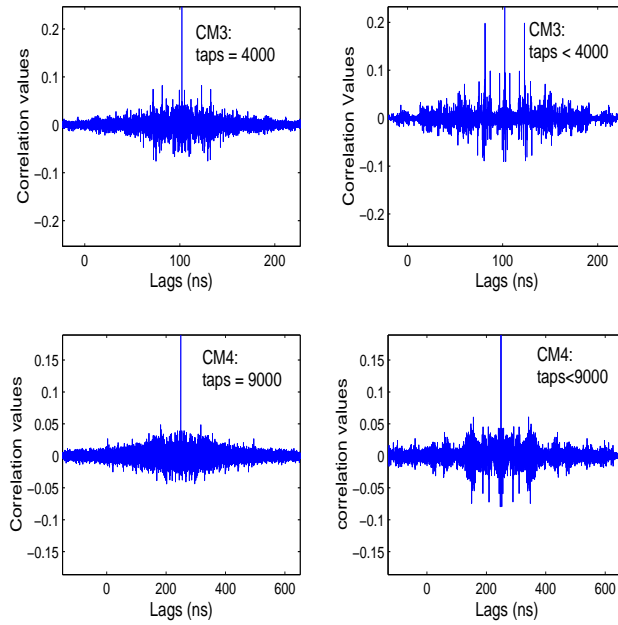
Figure 4.7 Average and Instantaneous IFI Effect: CM3 and CM4

analytically that overall IFI effect is negligible when N_f is very large and T_f is very small. With small N_f, overall IFI may be constructive or destructive. In the scenario, when IFI (small N_f per bit) effect over many bits is considered, combined IFI may be negligible. Actual simulation for All-Rake (large tap number, small N_f) and for Partial RAKE (small tap number, small N_f) over many bits produces IFI BER performance close to non IFI case and supports the analysis. Therefore, it can be safely concluded that IFI may not be a problem for RAKE receivers for BPSK and PPM modulation schemes and the restrictions on T_c, T_f, N_f to avoid IFI may be removed, which may allow higher data rate, relax PN code limit, increase processing gain, increase user capacity etc. As a future research IFI may be investigated for multiple user interference (MUI) and for ISI when the guard interval between symbols are lifted. In the next section performance of coherent receiver is investigated in the presence of both IFI and ISI in UWB systems.

4.7   IFI and ISI in UWB Systems

In high data rate systems, it may be impossible to prevent leakage of multipaths among symbols in both coherent and noncoherent UWB receivers. The resulting ISI is addressed in the
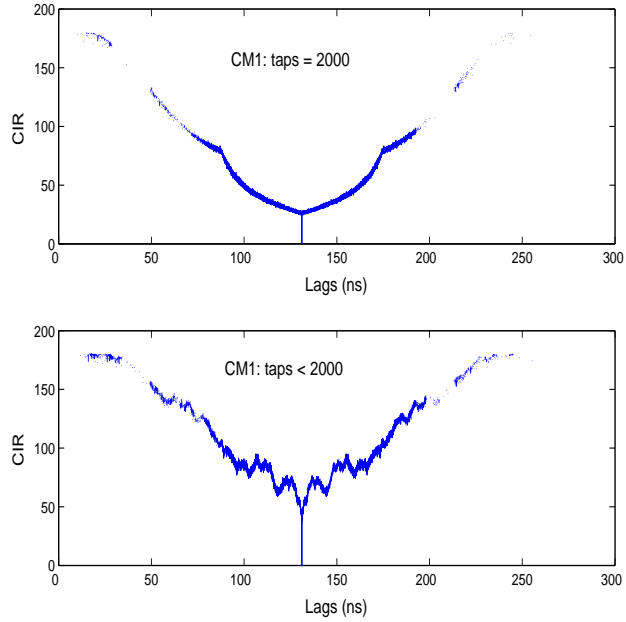
Figure 4.8 Average and Instantaneous CIR: CM1 (1000 Realizations)

past for coherent [50, 51] and non-coherent [52, 53] receivers to improve receiver performance under ISI. In this part of the chapter the ISI is evaluated in RAKE receivers using Pulse Amplitude Modulation (PAM) and Pulse Position Modulation (PPM) schemes. The primary contribution of this part is to show that for high data rate systems, ISI from a large number of symbols make the overall ISI effect negligible on RAKE receiver performance. An analysis and supporting simulation results prove such conclusions. The ISI is also investigated in the presence of IFI. In the following section, signal structure for the RAKE receiver is presented. The same notations used in the previous sections are used in the following sections as well.

4.8   Signal Structure in the Presence of Both IFI and ISI

In a generic TH UWB multiple access scheme, pulses of each user are replicated in time over N_f number of frames according to a unique TH code. Each transmission block can contain N successive symbols. The transmitted and received signals of the kth user in a multipath environment can be expressed as $s^k(t)$ and $r^k(t)$ according to equations (4.1) and (4.2) respectively. A single user case is considered in the following sections and hence the superscript k is omitted. The same
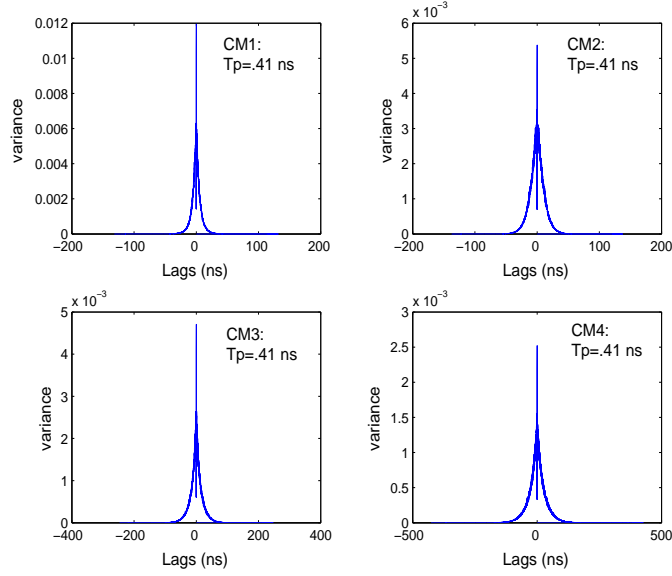
Figure 4.9 Variance with Lags, Channel Convolved with Pulse of 0.41ns

analysis and results can be extended to any number of users. Without loss of generality if $N_f = 1$ and $N_c = 1$ is considered, equations (4.1) and (4.2) can be simplified to exclude the subscripts and parameters for frame indices, chip indices and TH codes. The reduced equations are expressed as,

$s(t) = A\beta\omega(t - b\delta)$ and $r(t) = \sum_{l=0}^{L-1} A\beta\gamma_l\omega(t - b\delta - \tau_l) + z(t)$.

In the following sections, Binary Phase Shift Keying (BPSK) and binary PPM schemes are considered for modulation. The analysis can be extended to higher order modulation schemes as well. It is noted that orthogonal PPM is used in here, where the value of δ is chosen to be equal to T_p. In the presence of ISI, the received signal includes contributions from other $N-1$ symbols of the same user. In BPSK, symbols are transmitted T_p and in PPM, $2T_p$ width apart. For convenience of analysis, the channel is discretized to the timing resolution of either the receiver sampling rate or to the pulse bandwidth. It is assumed that $\tau_l = l\Delta$, where Δ is the chosen minimum timing resolution. Since consecutive symbols are transmitted T_p width apart and T_g is the path delay, the range of ISI contributing paths of the nth symbol can be written as $l = 1$ to $\frac{T_g - T_p(n-1)}{\Delta}$ (for PPM, T_p is replaced by $2T_p$). If $\frac{T_g - T_p(n-1)}{\Delta}$ is denoted by L_{ISIn}, the received signal can be expressed as eqn (4.7), where β_n represent the change in pulse amplitude and b_n represent the bit value of the

109
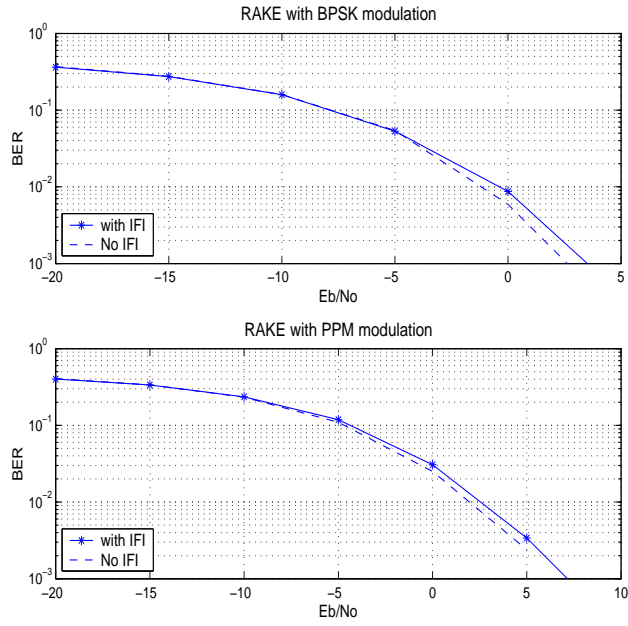
Figure 4.10 All-Rake BER Performance for CM1
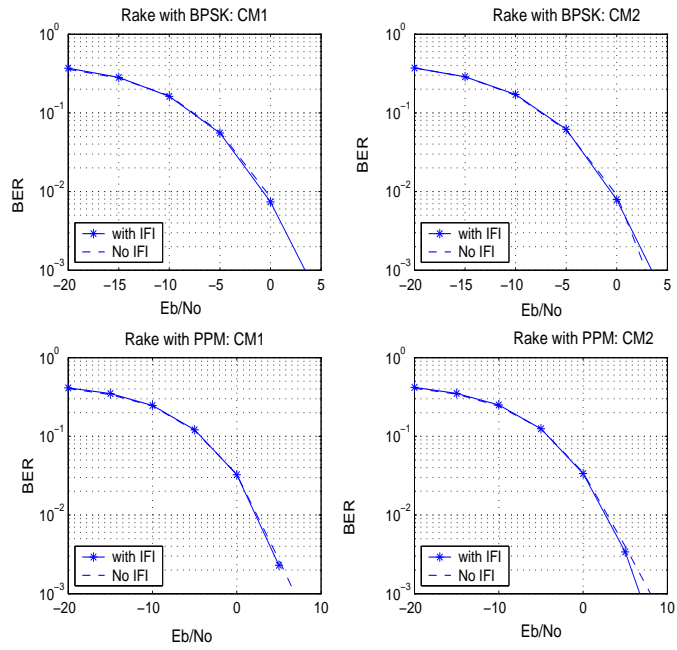
Figure 4.11 Partial RAKE BER Performance for CM1, CM2
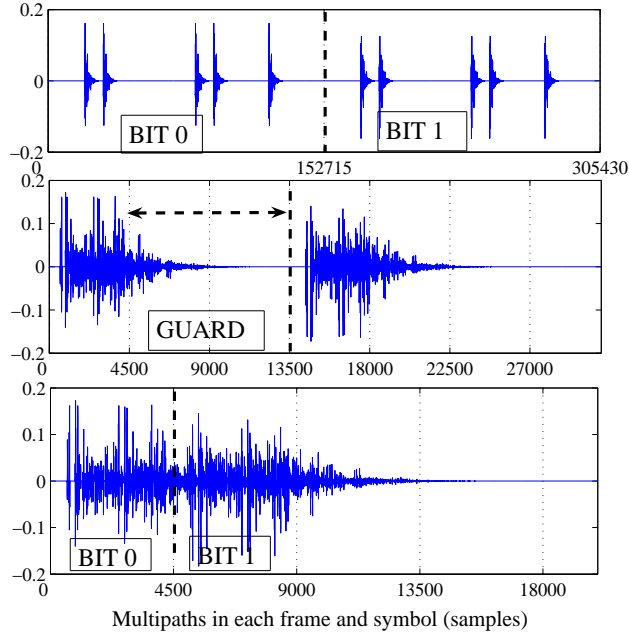
Figure 4.12 IFI and ISI: CM1, $N_c = 3$, $N_f = 5$, PN=[3 1 3 1 1]

nth symbol when PAM or PPM modulation scheme is considered respectively. The $r_{ISI}(t)$

$$r_{ISI}(t) = \sum_{l=0}^{L-1} A\beta\gamma_l\omega(t - b\delta - \tau_l),$$

$$+ \underbrace{\sum_{n=2}^{N} \sum_{l=0}^{L_{ISIn}-1} A\beta_n\gamma_l\omega(t - b_n\delta - \tau_l - T_p(n-1))}_{ISIterm} + z(t). \tag{4.7}$$

The of eqn. (4.7) excludes $b\delta$ and $b_n\delta$ parameters when PAM is used and excludes β and β_n parameters when PPM scheme is used. In the following section, the analysis of ISI in UWB is presented.

4.9 Analysis of ISI in UWB

For the analysis, it is assumed that the channel is constant over the ISI affected and its corresponding ISI contributing symbols and the transmitted and received pulses are identical. In an ideal All-Rake receiver, energy is gathered from all received multipaths by correlating the received signal

111
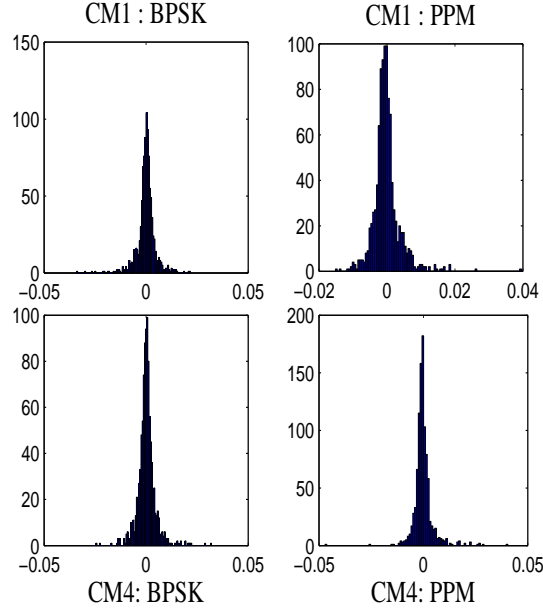
Figure 4.13 Histogram of Effective ISI for RAKE Receiver, Tp .41ns, ISIbits 99

with a local template and the correlator output is combined to form the decision statistics. Under the assumptions of a perfectly estimated channel and a perfect synchronization at the receiver, the correlator output of All-Rake receiver can be expressed as, $y_{rk}(t) = \int_0^{T_g} r_{ISI}(t)\phi(t)$, where $\phi(t)$ represents the local template at the receiver and, $\phi(t) = \psi(t)$ for BPSK and $\phi(t) = \psi(t) - \psi(t - \delta)$ for binary PPM. The value of $\psi(t)$ is represented as, $\psi(t) = \sum_{l=0}^{L-1} A\gamma_l \omega(t - \tau_l)$.

4.9.1   BPSK Modulation Scheme

After substituting (4.7) in $y_{rk}(t)$ and replacing $\phi(t)$ with $\psi(t)$ along with some mathematical computation (steps are omitted due to limited space) the decision variable for BPSK for bit 1, summed over one frame and conditioned on $\beta = 1$ can be expressed as,

$$
\begin{aligned}
y_{rkBPSK}(t) &= \int_0^{T_g} \Big(T(t)M(t) + T(t)N(t) + \underbrace{T(t)I(t)}_{ISI} \Big), \\
&= m_{BPSK} + N_{BPSK} + ISI_{BPSK},
\end{aligned}
\tag{4.8}
$$

where, $T(t) = \sum_{l=0}^{L-1} A\gamma_l \omega(t - \tau_l)$ represents the noise free local template for BPSK, $M(t) = \sum_{l=0}^{L-1} A\beta\gamma_l \omega(t - \tau_l)$ represents the desired BPSK modulated signal and $N(t) = z(t)$ represents the

AWGN noise. Variable $I(t) = \sum_{n=2}^{N} \sum_{l=0}^{L_{ISIn}-1} A\beta_n\gamma_l\omega(t - \tau_l - T_p(n - 1))$ represents the ISI from

other bits . The decision rule for BPSK is as follows: if $y_{rkBPSK}(t) > 0$, the transmitted bit is 1,

otherwise the bit is 0.

In order to derive the probability of error, each term of (4.8) can be evaluated similar to [50,

54]. In this chapter, $Ns = Nf = 1$ is considered. No pre-rake combining is applied. The N_{BPSK}

is uncorrelated and zero mean random variable since $N(t)$ is AWGN. Replacing the values for

$T(t)$, $M(t)$ and $I(t)$ in (4.8) and after some straightforward derivation, the components and their

variances of $y_{rkBPSK}(t)$ can be expressed as follows,

$$
\begin{aligned}
m_{BPSK} &= \sum_{l=0}^{L-1} A^2\gamma_l^2\omega^2(t - \tau_l), \\
VAR(N_{BPSK}) &= \frac{N_o}{2}E\Big(\sum_{l=0}^{L-1} A\gamma_l\omega(t - \tau_l)\Big)^2, and \\
VAR(ISI_{BPSK}) &= E\Big(\sum_{l=0}^{L-1} A\gamma_l\omega(t - \tau_l) \\
&\quad \cdot \sum_{l=0}^{L_{ISI2}-1} A\beta_2\gamma_l\omega(t - \tau_l - T_p(2 - 1)) + ... \\
&\quad + \sum_{l=0}^{L-1} A\gamma_l\omega(t - \tau_l) \cdot \sum_{l=0}^{L_{ISIn}-1} \\
&\quad A\beta_n\gamma_l\omega(t - \tau_l - T_p(n - 1)) + ... + \sum_{l=0}^{L-1} A\gamma_l\omega(t - \tau_l) \\
&\quad \cdot \sum_{l=0}^{L_{ISIN}-1} A\beta_N\gamma_l\omega(t - \tau_l - T_p(N - 1))\Big)^2,
\end{aligned}
$$

(4.9)

where, the E is the expectation or mean parameter. The variable, m_{BPSK} is the desired correlator

output and is equal to the mean of y_{rkBPSK}. It is assumed that ISI_{BPSK} is a zero mean random

variable. The histogram in Fig. 4.13 validates this assumption. It is noted that each term within the

square of $VAR(ISI_{BPSK})$ represents the correlation between ISI free template and ISI contributing

paths from each undesired bit. The detection SNR at the RAKE correlator output for BPSK can
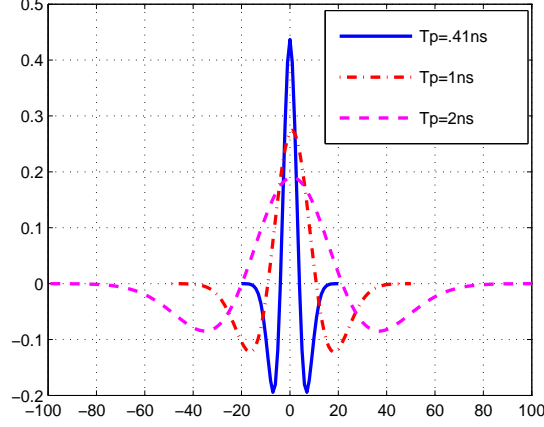
Figure 4.14 Various Pulse Widths

be expressed as,

$$SNR_{BPSK} = \frac{m_{BPSK}^2}{VAR(N_{BPSK}) + VAR(ISI_{BPSK})} \qquad (4.10)$$

The result in (4.10) is valid for both $\beta \in \{\pm 1\}$. When L and T_g are sufficiently large, central limit theorem can be used to approximate ISI_{BPSK} as Gaussian. Then the probability of bit error P_e can be given by, $P_e = Q(\sqrt{SNR_{BPSK}})$, where $Q(x) = \int_x^\infty \frac{1}{\sqrt{2\pi}} exp(\frac{-y^2}{2}) dy$.

4.9.2   PPM Modulation Scheme

After substituting (4.7) in $y_{rk}(t)$ and replacing $\phi(t)$ with $\psi(t) - \psi(t - \delta)$ along with some mathematical computation, the decision variable for PPM can be expressed as,

$y_{rkPPM}(t) = \int_0^{T_g} \Big(T_{PPM}(t) M_{PPM}(t)$

$+ T_{PPM}(t) N_{PPM}(t) + \underbrace{T_{PPM}(t) I_{PPM}(t)}_{ISI} \Big)$, where, $T_{PPM}(t) = \sum_{l=0}^{L-1} A\gamma_l \omega(t - \tau_l) - \sum_{l=0}^{L-1} A\gamma_l \omega(t -$

$\delta - \tau_l)$ represents the noise free local template for PPM, $M_{PPM}(t) = \sum_{l=0}^{L-1} A\gamma_l \omega(t - b\delta - \tau_l)$ represents the desired PPM modulated signal, $N_{PPM}(t)$ represents the AWGN noise. Variable $I_{PPM}(t) = \sum_{n=2}^{N} \sum_{l=0}^{L_{ISIn}-1} A\gamma_l \omega(t - b_n\delta - \tau_l - 2T_p(n-1))$ represents the ISI from other bits. The decision rule for PPM is as follows: if $y_{rkPPM}(t) > 0$, the transmitted bit value is 0 otherwise it is 1. (For bit '0' transmitted on the '0'th position). In Fig 4.12, two successive symbols of a single user is considered, where, $N_f = 5$, $N_c = 3$, the PN sequence is [3 1 3 1 1], and the minimum pulse

to pulse duration is equal to one chip length. In the top sub-figure, two bits are transmitted, where $T_c = T_g$, resulting in the absence of IFI or ISI. In the middle sub-figure, $T_c < T_g$ results in IFI, while a sufficient guard interval prevents ISI. In the bottom sub-figure, the guard is taken off allowing both IFI and ISI. From Fig. 4.12, it is clear that allowing IFI and ISI increase data rate. In [55], it is shown that IFI effect is negligible in All-Rake and Partial RAKE receiver performance. In the next section, simulation results are provided under the influence of both IFI and ISI.

4.10   Simulation Results under ISI

The BER is evaluated in simulation for All-Rake receiver using BPSK and PPM schemes. The CM1 and CM4 [48] channel models for indoor 802.15.3a standard are used. The total channel taps are 1000 in CM1 and 4000 in CM4. The received paths are combined using Maximal Ratio Combining (MRC). Three second order Gaussian pulses with $T_p = .41ns$, $T_p = 1ns$ and $T_p = 2ns$ are used in the simulation and are shown in Fig. 4.14. When $N_c = N_f = 1$ and $T_s = T_p$, the resulting data rates are 2.4, 1 and 0.5 Gbps. In a TH environment with $N_f > 1$, the same pulse widths result in lower data rates depending on the values of N_f, N_c and T_f for $T_c = T_p$.

ISI contributing bits vary from one realization to another. If the maximum T_g over all realizations is considered, it can be shown that for BPSK modulation schemes using $T_s = T_p = .41ns$ and $T_s = T_p = 1ns$, the ISI contributing bits exceed 100 in CM1. For $T_p = 2ns$, ISI bits is around 60. In CM4, T_g is larger and the the largest pulse width of $T_p = 2ns$ results in ISI contributing bits in excess of 100 and even more for shorter pulse widths. For PPM modulation, in CM1, $T_p = 2ns$ results in ISI bits less than 50 and in CM4, less than 100. In CM1, $T_p = 1ns$ results in bits less than 100. To include a high ISI contribution, the number of ISI contributing bits considered is 99, although for PPM less number of bits produce ISI. The value of N is 100 for each transmission block.

Fig. 4.15 and Fig. 4.16 illustrate the BER performance of All-Rake in the presence of ISI in CM1 channel, while Fig. 4.17 and Fig. 4.18 present the BER in CM4 channel. There is negligible performance difference between the presence and absence of ISI cases for both BPSK and PPM schemes in both channel models. The ISI free template in All-Rake generates ISI terms that contain
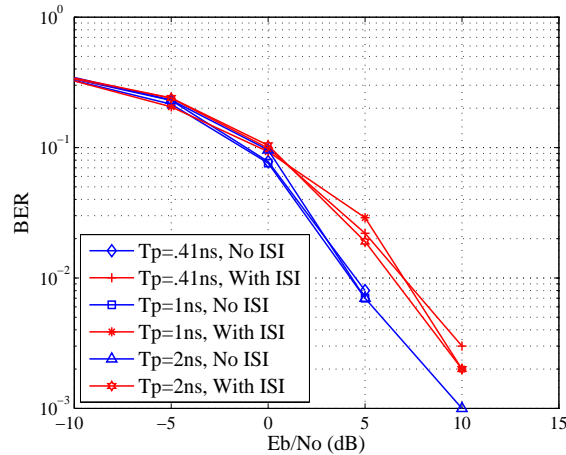
Figure 4.15 BER Performance in CM1 (BPSK)

no non-linear ISI [56]. This in turn prevents BER degradation due to non-linear ISI. According to
(4.8), the All-Rake decision variable consists of one ISI term and a noise term. Noise is pre-dominant
in the lower SNR values and the desired signal strength is weakened by noise in the absence of ISI.
As a result, ISI and ISI free performance coincide at low SNR. As the SNR increases, signal strength
increases in ISI free case and degrades in the presence of ISI due to dominating ISI term. As a
result, ISI performance is worse than ISI free performance at relatively higher SNR.

The PPM performance marginally supersedes that of BPSK in the ISI case. This can be
explained as follows. The PPM modulation allow the transmitted pulses to switch between two
positions. This makes some of the ISI contributing taps hit or miss the desired symbol taps.
Therefore, the overall effective ISI from all contributing bits may be reduced and performance is
improved. On the other hand, in BPSK, the undesired paths have more chance to hit the desired
paths.

It is seen that the ISI performance in CM4 is slightly better compared to the ones in
CM1 (Fig. 4.15 through 4.18) . This is due to the large number of paths present in CM4 that
result in a lower overall effective ISI compared to that of CM1. Fig. 4.13 illustrates the histogram
of effective ISI for BPSK and PPM schemes in CM1 and CM4 channel models. Data rate increases
significantly in the presence of ISI with negligible change in BER. In high data rate systems when
$N_f > 1$, IFI may also be present along with ISI. Fig. 4.19 presents the simulation results in the

116
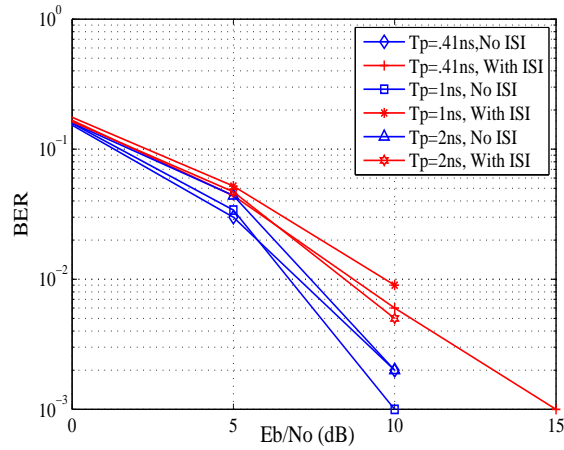
Figure 4.16 BER Performance in CM1 (PPM)
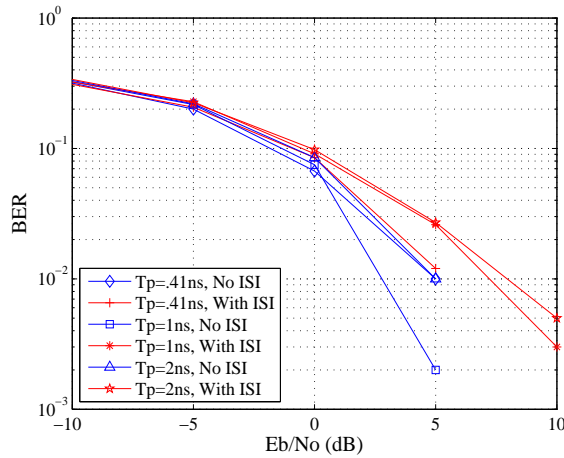
Figure 4.17 BER Performance in CM4 (BPSK)

presence of both IFI and ISI, the PN considered is [3 1 3 1 1]. It is seen that the overall effects of IFI and ISI on the BER is still negligible. In the next section, conclusion and discussion on future research are addressed.

4.11 Future Direction of IFI and ISI in RAKE UWB

In high data rate UWB systems, the presence of ISI may be unavoidable. Prior studies on ISI incorporated various techniques to improve coherent receiver performance under ISI. Here, ISI
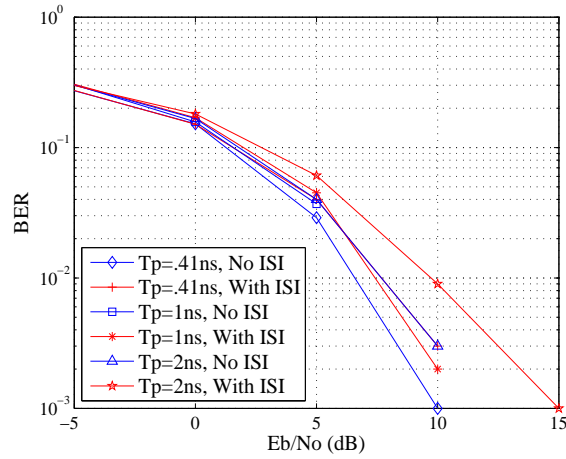
Figure 4.18 BER Performance in CM4 (PPM)
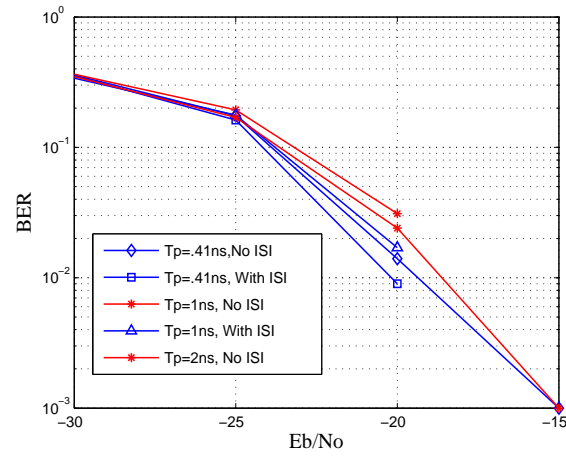
Figure 4.19 BER Performance in CM4 (BPSK) (with IFI and ISI)

is evaluated for RAKE receivers. It is shown that the ISI effect is negligible on RAKE receiver performance using BPSK and PPM modulation schemes. The ISI is also evaluated in the presence of IFI to show that the receiver performance is minimally effected due to both IFI and ISI. These results can be extended to incorporate multiple user interference (MUI) and synchronization error as part of future research. The next section addresses one of the key applications of ultra-wideband technology in locating the whereabouts, and thus determining the wandering behavior of Alzheimer's patients.

4.12 Ultra-wideband Application

Ultra wideband has numerous advantages over other technologies: First, UWB-RFID transmission can operate over unlicensed frequency ranges from 3.1GHz to 10.6GHz. The 7.5GHz bandwidth for UWB-RFID transmission comes with a severe restriction on power limit by the FCC. However, the restriction enables UWB-RFID to coexist with other technologies (for example 802.11a/g radio) that share narrow or smaller bands with the frequency range of UWB-RFID. UWB-RFID can therefore operate without creating interference for other users sharing the same frequency range. The UWB-RFID transmission power level is similar to background noise levels, i.e. a UWB-RFID signal may be deemed noise rather than an information signal by a non-UWB-RFID device. Different power limits for indoor and outdoor UWB-RFID transmission are set by the FCC; these limits also vary according to the transmitting UWB-RFID frequency. Since IR-UWB-RFID signal transmission does not require the encoding of an information signal on a high frequency carrier wave, the hardware and software necessary to process the signal is inherently reduced making UWB-RFID transmitters and receivers simple and inexpensive compared to other wireless communication technologies. The exceptionally large bandwidth available to UWB-RFID allows high rate data transmissions (on the order of 1Gbps) over very short ranges (less than 1m). UWB-RFID can tradeoff data rate against range allowing a variety of transmission modes according to the needs of the application and local conditions. UWB-RFID can penetrate a wide variety of materials including the human body, walls, and earth.

UWB's unique features make it an extraordinary candidate for applications requiring high data rate, low power, cost and complexity. A few of the current application areas include:

- Wireless Communication The high data rate and short range of UWB-RFID make it suitable for wireless home networking and peripherals (UWB-RFID wireless mouse, keyboard, wireless USB, high speed wireless personal area networking (WPAN), wireless body area network (WBAN) etc.)

- Imaging The high penetration capability of UWB-RFID gives it a great advantage in radar imaging systems, ground penetration radars, wall radar imaging, through-wall radar imaging,
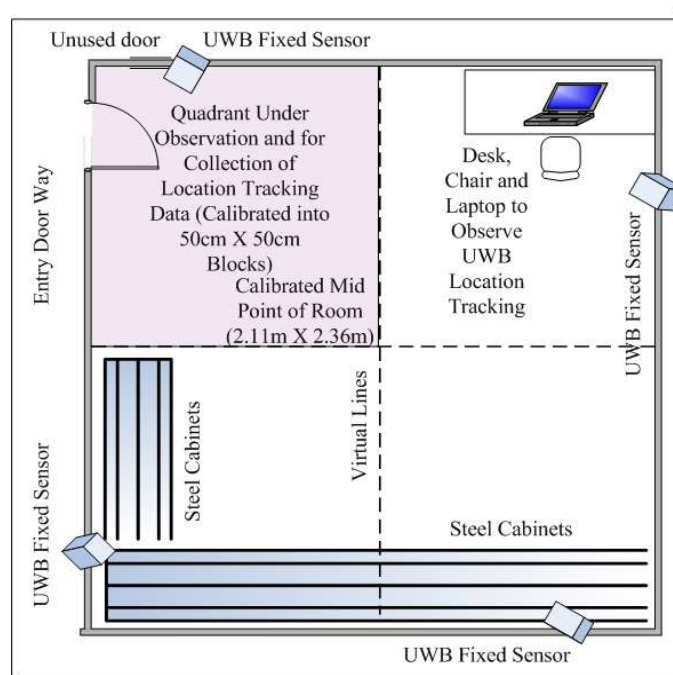
Figure 4.20 Floor Plan of Laboratory Testing Room

surveillance systems, medical imaging and imaging behind obstructions assisting firemen and public safety authorities.

• Location Tracking A unique feature of UWB-RFID is its ability to resolve or capture electromagnetic energy from numerous individual paths or rays that arrive at the receiving end with different time delays[12]. UWB-RFID can calculate the location of the transmitting point in real time and track the whereabouts of a moving transmitter. Some prominent applications of the location tracking capability of UWB-RFID are vehicular radar systems for avoiding collision, tracking targets in military applications, inventory tracking in warehouse environments and patient tracking in hospital environments.

UWB-RFID's strengths for determining location, patterns of movement and identity of multiple household residents are crucial to a fuller understanding of how wandering evolves in community settings for two reasons: 1.) diurnal rhythms in wandering behavior have been observed to occur suggesting that the risk of elopement (unattended departure through exit ways of a care setting)
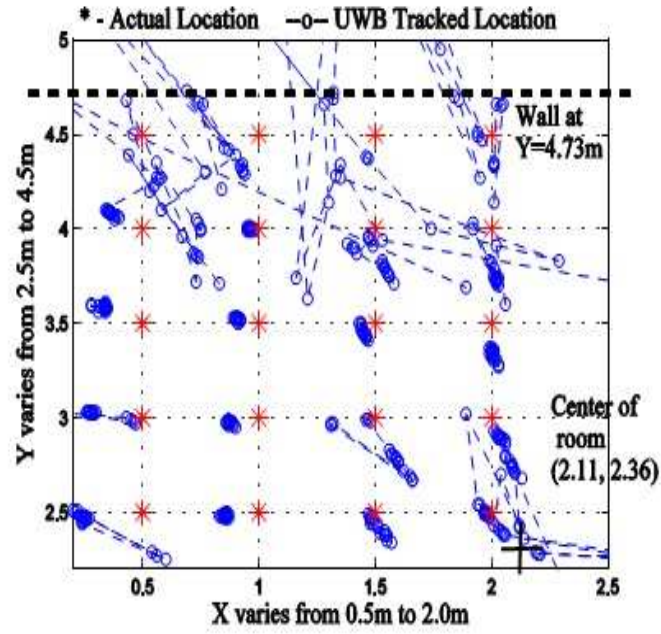
Figure 4.21 Plot of Location Data Collected from UWB-RFID Tag
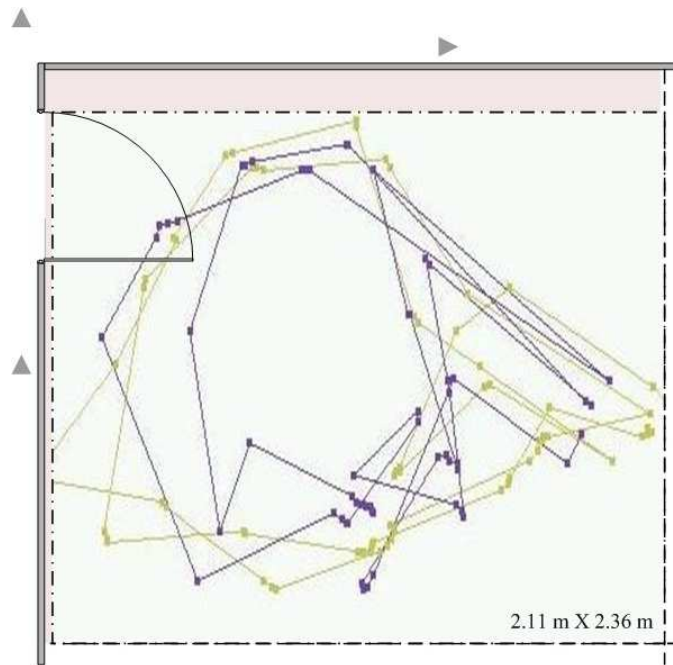
Figure 4.22 Shadowing Effect between Two Tags Carrying Human Subjects

121

increases at specific times of the day, and 2.) Persons who wander do so in social environments and may "shadow" or follow other persons out of doorways in response to behavioral or environmental cues.

Wandering within the home may not elevate risk, but wandering away from home definitely increases the risk of injury and death. Behaviors such as following another resident as they near an exit (shadowing) and remaining close to an exit door for extended periods (lingering) may therefore predict eventual elopement.

In order to study these two pre-elopement behaviors longitudinally using UWB-RFID technology, the following operational definitions are proposed: (a) Lingering, where a wanderer persistently remains near exitways and (b) Shadowing, where a wanderer closely follows or trails others seeking to exit. The relationship of lurking and shadowing behaviors to each other and their relationship to eventual elopement are unknown. Long term data collection will facilitate an understanding of the ontogeny of wandering and its evolving nature over the dementing process as it occurs in home environments. Systems that reveal the complex interplay of pre-elopement lurking and shadowing with behaviors of other household residents enhance our understanding of the phenomenon and will accelerate the creation of best practice guidelines for managing wandering.

A second but equally compelling reason for using longitudinal systems to measure wandering's precursor behaviors is to fairly evaluate existing technologies available to caregivers who must manage wandering in home settings. These technologies diverge in their theoretical assumptions and run the gamut from expensive and elaborate alarm systems to cheap cloth barriers placed over doorknobs and camouflage wallpapers, however their relative efficacies in home settings remain unknown. Best practices for which technologies work best for patients at varying levels of impairment must be informed by empirically sound methods which include longitudinal monitoring. A method that reveals the progression of wandering, elucidates the relationship of two of its key components (lurking and shadowing) to elopement; provides a relatively unbiased tool for assessing which technologies for managing wandering are best, and expands the knowledge base for the treatment of dementia is therefore highly desirable. An ideal tracking technology to gather the information needed to meet these objectives, should have the following characteristics.

122

- Unobtrusive Gathering longitudinal data in home settings, ideally, should not impact the normal behavior patterns of the residents. Additions to the home environment should be consistent with the architecture and dcor and not draw attention. If devices must be worn by the residents, they should be small, lightweight, waterproof, produce no social stigma, and be maintenance free. Data extraction should be possible without disruption of residents' routines.

- The range should be infinitely adjustable An ideal device must be able to detect a person wearing a transmitter at any distance within the home.

- Should be constantly online The device must be capable of gathering information continuously without interruption due to power line failure, and data storage must be permanent.

- Must differentiate a wanderer from another resident The device may not confuse a wanderer with another person. Movement by one resident cannot be misinterpreted as originating from another. The device's accuracy must not be affected by furniture or human bodies intervening between the recording device and the person(s) under study. It should never record the behavior of anyone or anything that is not the subject of study.

- Must detect shadowing when it occurs The device must be able to physically differentiate two individuals in close proximity and precisely track their arrival and departure times at a monitored area.

- Must detect lingering when it occurs The device must detect when an individual is in a monitored area and must precisely track their arrival and departure times from the areas with high precision.

- Must detect an elopement when it occurs The device must correctly determine when an individual passes over an exit threshold and successfully leaves the home. It must differentiate close contact with the interior surface of a door from movement across its threshold. It must record the time, date, and identity of the person crossing the threshold, and whether the person crossed the threshold alone or accompanied, and by whom.

123

Ultra wideband radio's powerful location tracking characteristics, fulfilling the device criteria mentioned above, make it a prominent candidate to track the Alzheimer's patients with a high precision accuracy. A laboratory study of UWB-RFID technology is conducted here and its data presented. Fig. 4.20 illustrates the laboratory testing floor plan, where the UWB fixed receivers are mounted on the four walls. The test subjects carrying the UWB wrist tags or UWB transmitters, walk around the room, while the tags transmit data to the UWB receivers. Fig. 4.21 shows the plot of collected/recorded location data using UWB transceiver system, and Fig. 4.22 shows the shadowing effect between two UWB tags, when the test subjects move around the room, one behind the other.

At the end of this laboratory testing, UWB systems are implemented in real homes of Alzheimer's patients, who are also veteran's, to track their wandering behavior. This project is funded by the Veterans Administration (VA) of USA.

CHAPTER 5 :

CONCLUSION

Wireless communication technology, in the terrestrial radio frequency domain, is advancing in lightning speed. The key reason being, the necessity and demand of consumers to have communication available, anywhere, anytime, and in anyway. The human habitats and livings on land, necessitate the development of communication technology in the terrestrial RF domain. However, future sustainability of human life on land depend on fully exploring and utilizing the vast water resources in the underwater domain. In order to achieve this, advanced technology needs to be researched and implemented to facilitate the exploration, understanding, and using the resources available in the underwater domain.

This dissertation addresses three of the key difficulties that are faced by manned and/or unmanned vehicles, during underwater acoustic communication with each other, while carrying out their task of underwater exploration and/or applications. The contributions of this research involve addressing these difficulties and provide feasible solutions to handle such difficulties.

5.1 Underwater Acoustic Communication Channel

The underwater acoustic communication (UAC) environment and consequently, the UAC channel, varies in the degree of severity compared to terrestrial radio frequency (RF) communication environment. In addition, the UAC presents challenges that may be absent in the RF communication domain.

5.1.1 Channel Representation

The UAC channels are highly variable in nature in time, frequency, and in spatial domains according to the channel environment. It is imperative to represent the channels according to

the environment parameters that define each channel. This dissertation provides a comprehensive classification and representation of the underwater acoustic communication channel based on the channel environments.

5.2 Doppler Shift Effect in UAC OFDM Systems

In a UAC environment, the transmission bandwidth is often comparable to the carrier frequency and the Doppler amount. This creates a varying Doppler shift effect over OFDM subcarriers in UAC OFDM systems, which in turn leads to loss of orthogonality of OFDM subcarriers. This dissertation proposes two Doppler scale estimation algorithms to estimate Doppler scale and use the estimated values to mitigate varying Doppler shift effect over OFDM subcarriers.

5.3 Inter-symbol Interference in Ultra-wideband

Very large delay spread, which is a function of the UWB channel environments, can cause severe ISI among the symbols in UWB systems. That in turn degrades receiver performance significantly. This dissertation provides a feasible solution to long delay spread causing ISI by allowing the symbols to overlap intentionally and presents the performance results under such ISI.

REFERENCES

[1] F. Schill, U. Zimmer, and J. Trumpf, "Visible Spectrum Optical Communication and Distance Sensing for Underwater Applications," *Proc. Australasian Conf. Robotics and Automation (Canberra, 2004)*.

[2] M. Stojanovic, "Recent advances in high-speed underwater acoustic communications," *Oceanic Engineering, IEEE Journal of*, vol. 21, no. 2, pp. 125–136, 1996.

[3] "The Development of a MEMS-based Integrated Wireless Remote Biosensors," 2005.

[4] S. Ahmed and H. Arslan, "Cognitive Intelligence in UAC Channel Parameter Identification, Measurement, Estimation, and Environment Mapping," in *Proc. MTS/IEEE OCEANS*, Bremen, Germany, May 2009.

[5] ——, "Cognitive Intelligence in the Mapping of Underwater Acoustic Communication Environments to Channel Models," in *Proc. MTS/IEEE OCEANS*, Biloxi, Mississippi, USA, Oct 2009.

[6] R. Galvin and R. Coats, "A Stochastic Underwater Acoustic Channel Model," in *proc. MTS/IEEE Oceans*, Fort Lauderdale, FL, Sep 1996.

[7] A. K. Morozov, "The Sequential Analysis Application in the Problem of Estimation of Stochastic Channel Impulse Response," in *proc. MTS/IEEE Oceans*, San Diego, CA, Oct 1995.

[8] S. Byun, S. Kim, Y. Lim, and W. Seong, "Time-varying Underwater Acoustic Channel Modeling for Moving Platform," in *proc. MTS/IEEE Oceans*, Vancouver, BC, Sep 2007.

[9] S. Appleby and J. Davies, "Time, Frequency and Angular Dispersion Modeling in the Underwater Communications Channel," in *proc. MTS/IEEE Oceans*, Nice, France, Sep 1998.

[10] X. Geng and A. Zielinski, "An eigenpath underwater acoustic communication channel model," *proc. MTS/IEEE OCEANS*, vol. 2, 1995.

[11] C. Bjerrum-Niese and R. Lutzen, "Stochastic Simulation of Acoustic Communication in Turbulent Shallow Water," *IEEE Journal of Oceanic Engineering*, vol. 25, no. 4, Oct 2000.

[12] P. Walree, T. Jenserud, and M. Smedsrud, "A Discrete-Time Channel Simulator Driven by Measured Scattering Functions," *IEEE Journal on Selected Areas in Communication*, vol. 26, no. 9, Dec 2008.

[13] F. Socheleau, C. Laot, and J. Passerieux, "Stochastic Replay of Non-WSSUS Underwater Acoustic Communication Channels Recorded at Sea," *IEEE Transactions on Signal Processing*, vol. 59, no. 10, Oct 2011.

[14] M. A. M. Gutierrez, P. L. P. Sanchez, and J. V. V. Neto, "An eigenpath underwater acoustic communication channel simulation," *Oceans, Proceedings of MTS/IEEE*, vol. 1, pp. 355–362, Sep 2005.

[15] X. Lurton, *An Introduction to Underwater Acoustics: principles and applications, Springer,Chichester , UK:.* Springer, 1996.

[16] M. B. Porter, "The bellhop manual and user's guide: Preliminary draft," *Heat, Light, and Sound Research, Inc.*, 2011, url=http://oalib.hlsresearch.com/Rays/HLS-2010-1.pdf.

[17] A. Maggi and A. Duncan, "Underwater acoustic propagation modeling software-actup v2.2l," *Center for Marine Science and Technology (CMST)*, 2005, url=http://cmst.curtin.edu.au/products/actoolbox.cfm.

[18] A. Bessios and F. Caimi, "Multipath compensation for underwater acoustic communication," in *proc. MTS/IEEE OCEANS*, vol. 1, 1994.

[19] A. Salberg and A. Swami, "Doppler and frequency-offset synchronization in wideband OFDM: Estimators and performance analysis," *Proc. Nordic Signal Processing (NORSIG)*.

[20] B. Li, S. Stojanovic, M. Freitag, and P. Willett, "Non-Uniform Doppler Compensation for Zero-Padded OFDM over Fast-Varying Underwater Acoustic Channels," *proc. MTS/IEEE OCEANS*, pp. 1–6, 2007.

[21] S. Mason, C. Berger, S. Zhou, and P. Willett, "Detection, synchronization, and Doppler scale estimation with multicarrier waveforms in underwater acoustic communication," *Selected Areas in Communications, IEEE Journal on*, vol. 26, no. 9, pp. 1638–1649, 2008.

[22] B. Li, S. Zhou, M. Stojanovic, L. Freitag, and P. Willett, "Multicarrier communication over underwater acoustic channels with nonuniform Doppler shifts," *Oceanic Engineering, IEEE Journal of*, vol. 33, no. 2, pp. 198–209, 2008.

[23] C. Berger, S. Zhou, J. Preisig, and P. Willett, "Sparse channel estimation for multicarrier underwater acoustic communication: From subspace methods to compressed sensing," *Signal Processing, IEEE Transactions on*, vol. 58, no. 3, pp. 1708–1721, 2010.

[24] Stojanovic, "Low Complexity OFDM Detector for Underwater Acoustic Channels," *Oceans*, pp. 1–6, Sep 2006.

[25] B. Kim and I. Lu, "Parameter study of OFDM underwater communications system," in *proc. MTS/IEEE OCEANS*, vol. 2, 2000.

[26] J. Huang, S. Zhou, J. Huang, R. C. Berger, and P. Willett, "Progressive inter-carrier interference equalization for ofdm transmission over time-varying underwater acoustic channels," *IEEE J. Selected Topics in Signal Processing*, vol. 5, no. 8, pp. 1524–1536, Dec. 2011.

[27] T. Kang and R. Iltis, "Iterative carrier frequency offset and channel estimation for underwater acoustic OFDM systems," *Selected Areas in Communications, IEEE Journal on*, vol. 26, no. 9, pp. 1650–1661, 2008.

[28] W. Lam, R. Ormondroyd, and J. Davies, "A frequency domain adaptive coded decision feedback equalizer for a broadband UWA COFDM system," in *OCEANS'98 Conference Proceedings*, vol. 2. IEEE, 2002, pp. 794–799.

[29] Z. Wang, S. Zhou, B. G. Giannakis, R. C. Berger, and J. Huang, "Frequency-domain oversampling for zero-padded ofdm in underwater acoustic communications," *IEEE J. Oceanic Engineering*, vol. 37, no. 1, pp. 14–24, Jan. 2012.

[30] K. Tu, D. Fertonani, M. T. Duman, M. Stojanovic, G. J. Proakis, and P. Hursky, "Mitigation of intercarrier interference for ofdm over time-varying underwater acoustic channels," *IEEE J. Oceanic Engineering*, vol. 36, no. 2, pp. 156–171, Apr. 2011.

[31] Z. Wang, S. Zhou, J. Catipovic, and J. Huang, "Factor-graph-based joint ibi/ici mitigation for ofdm in underwater acoustic channels with long-separated clusters," *IEEE J. Oceanic Engineering*, vol. 37, no. 4, pp. 680–694, Oct. 2012.

[32] P. Carrascosa and M. Stojanovic, "Adaptive MIMO detection of OFDM signals in an underwater acoustic channel," in *OCEANS 2008*. IEEE, 2009, pp. 1–7.

[33] G. Leus and P. van Walree, "Multiband OFDM for covert acoustic communications," *Selected Areas in Communications, IEEE Journal on*, vol. 26, no. 9, pp. 1662–1673, 2008.

[34] S. Yerramalli and U. Mitra, "Optimal resampling of ofdm signals for multiscale-multilag underwater acoustic channels," *IEEE J. Oceanic Engineering*, vol. 36, no. 1, pp. 126–138, Jan. 2011.

[35] S. Beygi and U. Mitra, "Optimal bayesian resampling for ofdm signaling over multi-scale multilag channels," *IEEE Signal Processing Letters*, vol. 20, no. 11, pp. 1118–1121, Nov. 2013.

[36] T. S. Rappaport, *Wireless Communications: principles and practice, Pearson Education, Delhi, India:*. Pearson, 2002, ch. Mobile Radio Propagation: Small-Scale Fading and Multipath, pp. **5**–182 – **5**–183.

[37] I. Capoglu, Y. Li, and A. Swami, "Effect of Doppler spread in OFDM-based UWB systems," *Wireless Communications, IEEE Transactions on*, pp. 2559–2567, Sep 2005.

[38] R. Y. Yen, H. Y. Liu, and W. Tsai, "QAM Symbol Error Rate in OFDM Systems Over Frequency-Selective Fast Ricean Fading Channels," *Vehicular Technology, IEEE Transactions on*.

[39] Y. Mostofi and D. Cox, "ICI Mitigation for Pilot-Aided OFDM Mobile Systems," *Wireless Communications, IEEE Transactions on*, vol. 4, no. 2, pp. 765–774, 2005.

[40] M. Chitre, J. Potter, and O. Heng, "Underwater acoustic channel characterisation for medium-range shallow water communications," *proc. MTS/IEEE OCEANS*, pp. 9–12, Nov 2004.

[41] D. Cassioli, M. Z. Win, F. Vatalaro, and A. F. Molisch, "Performance of low-complexity RAKE reception in a realistic UWB channel," in *Proc. IEEE Int. Conf. Commun. (ICC)*, vol. 2, New York, USA, Apr. 2002, pp. 763–767.

[42] M. H. Chung and R. A. Scholtz, "Comparison of transmitted- and stored-reference systems for Ultra-wideband communications," in *Proc. IEEE Military Commun. Conf. (MILCOM)*, vol. 1, Monterey, CA, Oct. 2004, pp. 521–527.

[43] J. D. Choi and W. E. Stark, "Performance of ultra-wideband communications with suboptimal receivers in multipath channels," *IEEE J. Select. Areas. Commun.*, vol. 20, no. 9, pp. 1754–1766, Dec. 2002.

[44] ——, "Performance analysis of rake receivers for ultra-wideband communications with ppm and ook in multipath channels," in *IEEE Int. Conf. on Commun. (ICC)*, vol. 3, April 2002, pp. 1969–1973.

[45] B. Mielczarek, M. Wessman, and A. Svensson, "Performance of coherent uwb rake receivers with channel estimators," in *Proc. IEEE Vehic. Technol. Conf. (VTC)*, vol. 3, Oct 2003, pp. 1880–1884.

[46] L. Yang and G. B. Giannakis, "Digital-carrier multi-band user codes for baseband uwb multiple access," *J. Commun. Networks (JCN)*, vol. 5, no. 4, pp. 374–385, Dec. 2003.

[47] M. G. D. Benedetto and G. Giancola, *Understanding Ultra Wide Band Radio Fundamentals*, 1st ed. New Jersey: Prentice Hall, 2004.

[48] J. Foerster, "IEEE P802.15 working group for wireless personal area networks (WPANs), channel modeling sub-committee report - final," Mar. 2003. [Online]. Available: http://www.ieee802.org/15/pub/2003/Mar03/

[49] D. Porcino and W. Hirt, "Ultra-wideband radio technology: Potential and challenges ahead," *IEEE Commun. Magazine*, vol. 41, no. 7, pp. 66–74, Jul. 2003.

[50] M. Jun and T. Oh, "Performance of pre-rake combining time hopping UWB system," *IEEE Trans. on Consumer Electronics*, vol. 50, no. 4, pp. 1033–1037, Nov 2004.

[51] Y. Zheng, J. Ng, and L. Yang, "A Low-Complexity Blind Rake Combining Equalizer for UWB Communication Systems," in *Proc. IEEE International Conference on Ultra-Wideband*, Waltham, MA, USA, Sep 2006, pp. 629–633.

[52] K. Witrisal, G. Leus, M. Pausini, and C. Krall, "Equivalent system model and equalization of differential impulse radio uwb systems," *IEEE Journal on Selected Areas in Commun.*, vol. 23, no. 9, pp. 1851–1862, Sep 2005.

[53] M. Pausini, G. Janssen, and K. Witrisal, "Performance enhancement of differential UWB autocorrelation receivers under ISI," *IEEE Journal on Selected Areas in Commun.*, vol. 24, no. 4, pp. 815–821, April 2006.

[54] M. H. Chung and R. A. Scholtz, "Comparison of transmitted- and stored-reference systems for Ultra-wideband communications," in *Proc. IEEE Military Commun. Conf. (MILCOM)*, vol. 1, Monterey, CA, Oct. 2004, pp. 521–527.

[55] S. Ahmed and H. Arslan, "Inter-frame interference in time hopping impulse radio based uwb systems for coherent receivers," in *Proc. IEEE Vehicular Technology Conference (VTC)*, Montreal, Canada, Sep 2006.

130

[56] J. Romme and K. Witrisal, "Impact of UWB Transmitted-Reference Modulation on Linear Eualization on-Linear ISI Channels," in *Proc. IEEE Vehicular Technology Conf. (VTC)*, vol. 3, 2006, pp. 1436–1439.

[57] S. Ahmed and H. Arslan, "Analysis of Underwater Acoustic Communication Channels," *The Marine Technology Society (MTS) Journal*, vol. 47, no. 3, pp. 99–117, May/Jun 2013.

[58] ——, "Evaluation of Frequency Offset and Doppler Effect in Terrestrial RF and Underwater Acoustic OFDM Systems," in *Proc. IEEE The Military Communicatins Conference,(MILCOM)*, San Diego, CA, USA, Nov 2008.

[59] ——, "Ifi and isi in high data rate uwb coherent transceivers," in *Proc. IEEE Radio and Wireless Symposium (RWS)*, Orlando, FL, Jan 2008.

[60] D. W. Kearns, D. Donna Algase, D. H. D. Helen Moore, and S. Ahmed, "Ultra wideband radio: A novel method for measuring wandering in persons with dementia," *Geron Technology Journal*, vol. 7, no. 1, pp. 48–57, Jan 2008.

APPENDICES

Appendix A : Acronyms

Acronym	Description
AWGN	additive white Gaussian noise
BER	bit error rate
BPSK	binary phase shift keying
CI	cognitive intelligence
CP	cyclic prefix
CR	cognitive radio
DFT	discrete Fourier transform
FFT	fast Fourier transform
ICI	inter-carrier interference
IDFT	inverse discrete Fourier transform
IEEE	Institute of Electrical and Electronics Engineers
IFFT	inverse fast Fourier transform
i.i.d.	independent and identically distributed
IFI	inter-frame interference
ISI	inter-symbol interference
LOS	line-of-sight
NASA	National Aeronautics and Space Administration
NLOS	non-line-of-sight
OFDM	orthogonal frequency division multiplexing
PDF	probability density function
PHY	physical layer
QPSK	quadrature phase shift keying
SPAWAR	Space and Naval Warfare Systems Command

Appendix A (Continued)

RF	radio frequency
SNR	signal-to-noise ratio
SIR	signal-to-interference ratio
SINR	signal-to-interference-plus-noise ratio
TPC	transmit power control
UAC	underwater acoustic communication
UWB	ultra-wideband
WCSP	Wireless Communications and Signal Processing
VA	Veterans Administration

Appendix B : Bibliographical Notes

This dissertation is based on research that I have performed between 2005 and 2012 with a number of outstanding colleagues in University of South Florida, Tampa Fl, in Veterans Administration (VA) of Tampa, FL, and with colleagues in a team project working with Space and Naval Warfare Systems Command (SPAWAR). Part of the material in Chapter 2, is published in [57], co-authored with Huseyin Arslan. Part of the work in Chapter 3, appears in [58], co-authored with Huseyin Arslan. Part of the work in Chapter 4, appears in separate papers, [55] and [59], co-authored with Huseyin Arslan. Part of this chapter also appears in [60] co-authored with William D. Kearns, Donna Algase RN and D. Helen Moore.

Appendix C : Permissions

Appendix C (Continued)

Informed consent and study design. Human subjects, including patients, have a right to privacy that should not be infringed without informed consent. Complete anonymity is often difficult to achieve. In relevant cases, informed consent should be obtained and indicated in the manuscript. In case a randomised controlled trial is reported, authors should refer to the CONSORT statement, available in six languages (www.consort-statement.org), and follow its recommendations.

Peer reviewing will be exercised on scientific contributions, such as review articles (2 peers), contributions on original research or design (at least 2 peers for full papers and 1 for shorter communications), and best practices (1 peer). Provide in your cover e-mail full contact information (e-mail and mailing addresses) of at least three potential peer-referees. The list should not name current or prior collaborators. You are also free to list persons whom you wish to be excluded from the review process. The editors will make the final choice of reviewing peers. Comments of peers will be communicated to the corresponding author of the manuscript. After peer review, the acting editor will inform the corresponding author as to the changes or corrections that are needed before publication can take place. The authors should submit the updated manuscript within 2 weeks when minor corrections are required, or 6 weeks after major changes. When the updated manuscript is not received after this time period, it is considered as new submission of a previously rejected manuscript.

Proofs showing the final layout of the paper will be sent in PDF format by e-mail to the corresponding author, for immediate handling. Proof corrections must be minimal. Thus it is essential that manuscripts are accurate when submitted.

Electronic publishing ahead of print is exercised after acceptance, typesetting and proof correction. The uploaded articles may be accessed through their digital object identifier (doi).

Copyright Protection. Authors submitting manuscripts do so upon the understanding that the work is unpublished, is not being considered for publication elsewhere, and has been checked and approved by all co-authors. The submission of the manuscript by the authors means that they automatically agree to assign exclusive copyright to the International Society for Gerontechnology (ISG), if and when the manuscript is accepted for publication. The work shall not be published elsewhere in any language without the written consent of ISG. The articles published in this journal are protected by copyright, which covers translation rights and the exclusive right to reproduce and distribute all of the articles printed in the journal. No material published in the journal may be stored on microfilm or videocassettes or in electronic databases and the like, or reproduced photographically, without the prior written permission of ISG. However, the ISG permits authors to reproduce their contributions on their own website for non-commercial purposes, provided a link is made to the content page of the issue in which the contribution appeared.

You are on a old section of the website of the Journal of the International Society for Gerontechnology. Please to go www.gerontechnology.info to go the the new website.

ABOUT THE AUTHOR

Sadia Ahmed received the B.Sc. degree in electrical and electronics engineering from Bangladesh University of Engineering and Technology (BUET), Dhaka, Bangladesh in 1993. She received her M.Sc. degree in computer science from University of Oklahoma, Norman, OK in 1999. From 1999 to 2004, and part of 2004, she worked as a programmer and as a senior programmer in Sanchez Computer Associates (currently part of Fidelity National), Philadelphia, PA, and in Quest Diagnostics, Philadelphia, PA respectively. In 2007, summer and fall, she worked as the research assistant in the SPAWAR naval underwater acoustic communication project (received SPAWAR Grant). From 2008 to 2010, she worked as part of a VA funded project (received VA Grant), where UWB-RFID was used to determine the wandering behavior of Alzheimer's VA patients in home setting. In 2011, she worked in Patel School of Global Sustainability, USF, as a graduate assistant. She also worked as the education co-ordinator in a local organic farm from 2009 to 2011, and as a part time teacher in the Hillsborough County School System, from 2012 to 2013.

She is currently working toward her Ph.D. degree with the Department of Electrical Engineering, University of South Florida, Tampa, FL. Her research interests include underwater acoustic communication channel modeling, Doppler and path loss mitigation, and underwater network. In the future, she would like to get involved in projects involving environment protection, by monitoring and collecting environmental data using underwater sensors.

She has been involved as a volunteer in the state parks, local radio stations, and local literacy programs, to help the Tampa community achieve better environment protection, better human health, and better education.